WELDABILITY OF POLYCRYSTALLINE ALUMINIDES

A. A. Fasching[*], G. R. Edwards[*], and S. A. David[#]

[*]Center for Welding and Joining Research
Department of Metallurgical and Materials Engineering
Colorado School of Mines
Golden, CO 80401

[#]Metals and Ceramic Division
Oak Ridge National Laboratory
Materials Joining Group
Oak Ridge, TN 37831

ABSTRACT

Water vapor present in the atmosphere during welding has been shown to cause fusion zone cold cracking in Fe_3Al alloys. Understanding the effect of water vapor concentration during welding is important to optimizing the welding parameters. Furthermore, the relationships between welding parameters, fusion zone microstructures, and cold cracking susceptibility must be understood if these advanced materials are to be effectively utilized. Preliminary studies have indicated that coarse-grained fusion zones for these alloys are the most susceptible to cold cracking. Because refined fusion zone microstructures are expected to exhibit superior properties, including resistance to cold cracking, a technique was developed to refine the fusion zone with magnetic arc oscillation during welding.

The GTA welding of iron-aluminide alloy FA-129 sheet was conducted using a 225-amp water-cooled torch enclosed in a controlled-atmosphere glove box. A two-pole magnetic arc oscillator deflected the arc during welding in a direction either longitudinal to or transverse to the welding direction. Transverse arc oscillations resulted in more significant fusion zone refinement.

Both arc oscillation amplitude and frequency were also found to affect grain refinement; low frequency (25 Hz) and small amplitudes (1.5mm) were found to be most effective in reducing the average fusion zone grain size. A series of experimental welds, fabricated with arc oscillation to produce a range of fusion zone grain sizes, and with shielding gas containing a range of water vapor concentrations, is in progress. The threshold water vapor concentration, sufficient to cause cold cracking in each fusion zone microstructure, will be quantified.

INTRODUCTION

Interest in developing polycrystalline, long-range ordered iron-aluminide alloys for high temperature applications is great because of unique properties, such as superior oxidation resistance. However, detrimental properties such as low room temperature ductility and poor weldability restrict their use in structural applications. Water vapor present in the atmosphere has been shown to severely embrittle Fe_3Al alloys during processing steps that include welding

(Ref. 1). A knowledge of the water vapor concentrations which can be tolerated during welding is important to optimizing the welding parameters. Furthermore, the relationships between welding parameters, fusion zone microstructures, and cold cracking susceptibility must be understood if these advanced materials are to be effectively utilized.

Control of the fusion zone grain size is important for increased toughness and decreased susceptibility to cold cracking. Refined fusion zone microstructures are expected to exhibit superior mechanical properties as compared to non-refined microstructures. Iron-aluminide alloys, including Fe_3Al, lack a sufficient number of independent slip systems for accommodating grain boundary incompatibilities resulting from plastic deformation. This results in inherently low tensile ductilities (Ref. 2). Numerous researchers (Ref. 3-6) have shown that the fracture stress of many structural materials, including other ordered alloys, is inversely proportional to the square root of the grain diameter. This observation has been explained on the basis that the stress required to nucleate microcracks, and thus initiate unstable crack propagation, depends upon dislocation pileup length, which is longer in coarse-grained material. Fusion zone microstructures of an Fe_3Al alloy, refined through arc oscillation, should manifest an increased fracture toughness, and, thus, an increased tolerance for water vapor in the atmospheres present during GTA welding.

DISCUSSION OF CURRENT ACTIVITIES

This study was conducted on a single Fe_3Al - type alloy, FA-129. The nominal composition of alloy FA-129 is 77.7 wt. pct. Fe, 15.9 wt. pct. Al, 5.45 wt. pct. Cr, 0.97 wt. pct. Nb, and 0.05 wt. pct. C. This composition lies within the DO_3 phase field; however, during cooling from the solidus temperature, the composition passes through the disordered BCC field, the two-phase BCC plus B2 field, the single B2 phase field, and finally, the two-phase B2 plus DO_3 phase field. Knowledge concerning the effect of order-disorder transformations on weldability is also a concern, and is addressed in another on-going study. For this research concerning fusion zone grain refinement, the welding of iron-aluminide alloy FA-129 was conducted using a 225-amp water-cooled GTA torch. A two-pole magnetic arc oscillator, commercially available from PowCon, was used to deflect the arc. The apparatus consisted of a water-cooled electromagnetic probe which mounted on the GTA torch, and a control unit, as illustrated in Figure 1. The control unit consisted of a low-frequency triangle-wave oscillator that generated the current signal relayed to the electromagnetic probe. Individual controls independently adjusted either the frequency or the amplitude of the wave. Other controls included an arc position control, which provided a means of offsetting the arc path relative to the center line of the torch, and a dwell control for adjusting the relative time that the arc spent on either side of the mean position. Both

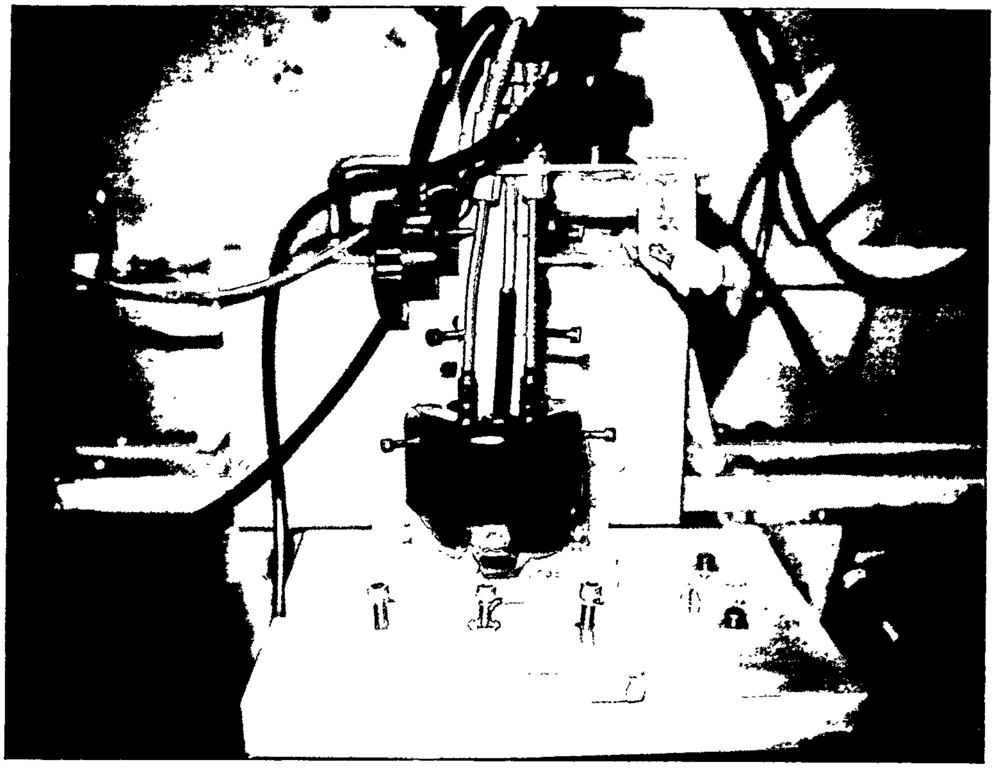

Figure 1. Photograph showing the magnetic arc oscillator. The stainless steel tips that extend down are the oscillation probes.

the arc position and dwell controls were set at neutral positions (along the centerline) for all of the welding experimentation. Thin sheet (0.75-mm-thick) specimens were used. Welding was conducted at a speed of 10 in./min. (4.23 mm/s) using 42 amps and 8 volts and an arc gap length of 0.04 in. (1.02mm). These parameters resulted in a heat input of 79.4 J/mm.

The welding arc was oscillated either parallel to or perpendicular to the welding direction. Arc oscillation creates refined solidification structures in the fusion zone that result from changes in the preferred growth direction, which are in turn caused by directional variations in the thermal gradient. Figure 2 shows a schematic diagram describing how the preferred growth direction changes with oscillation. For no oscillation, grains in the fusion zone grow epitaxially inward from the heat-affected zone along the steepest thermal gradient. Grains not oriented to grow in the direction of the thermal gradient will grow slower and be impinged by grains of preferred orientation. The isotherms follow the shape of the back of the weld pool, and the preferred growth direction at any point is perpendicular to the isotherm. In Figure 2a, the direction of preferred growth for a fixed point on the isotherm is indicated by an arrow. Successive arrows

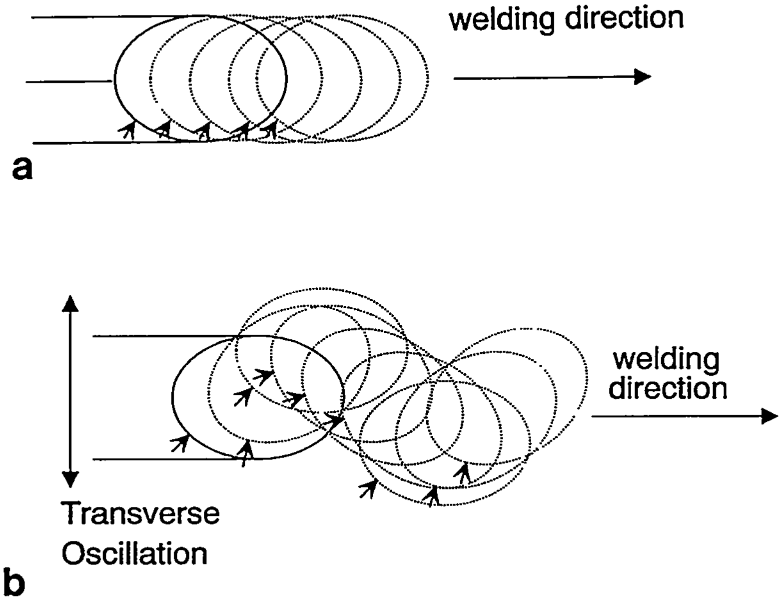

Figure 2. A schematic diagram showing the preferred growth direction, as indicated by the arrows, for: a) a non-oscillated weld pool, and b) a transversely oscillated weld pool.

follow the same point as the weld pool moves. When no arc oscillation is imposed, the resulting fusion zone has large, parallel, columnar grains. When the weld pool is oscillated longitudinal to the welding direction, the arc is simply moved back and forth. The oscillation effectively slows down the travel speed, resulting in a fusion zone similar to that found when the arc is not oscillated. During transverse oscillation, the maximum thermal gradient is constantly changing position, and consequently, the preferred growth direction continually changes. The arrows in Figure 2b once again locate the direction for preferred growth at a fixed point on the isotherm for a transversely oscillated weld pool. Depending upon the frequency and amplitude of oscillation, a grain favorably oriented for rapid growth parallel to the thermal gradient will grow for only a short time before the thermal gradient changes. At that point in time, that grain will be impinged by a faster growing grain, which in turn will grow only a short distance before it is impinged by another faster growing grain. The resulting fusion zone microstructure should contain many small grains. Experimentally, both transverse and longitudinal arc perturbation resulted in fusion zone microstructures similar to those predicted, as shown in Figures 3a and 3b.

Frequency and amplitude were varied systematically to determine optimal parameters for producing the most refined fusion zone structure. The frequency control allowed variations from 0.1 Hz to 100 Hz to be made. For this study, welding was conducted at 25, 50, and 75 Hz. A

Figure 3. The change in the fusion zone microstructure with changes in oscillation parameters is shown for: a) a longitudinal oscillation at a frequency=25 Hz and an amplitude=250/1000 (1.5 mm), b) a transverse oscillation at a frequency=25 Hz and an amplitude=250/1000 (1.5 mm), c) a transverse oscillation at a frequency=75 Hz and an amplitude=250/1000 (~1.5mm), and d) a transverse oscillation at a frequency=25 Hz and an amplitude=500/1000 (~1.9mm).

frequency of 25 Hz produced the finest structures overall, as shown in Figures 3b and 3c. Oscillations conducted at low amplitudes also proved more desirable, as indicated by comparing Figures 3b and 3d. All of these tests were conducted on the same heat of material (D5-3966-1), which was welded in the recrystallized condition.

Similar tests on a second heat of material (D5-3969-1) showed that refinement by arc oscillation was sensitive to compositional or microstructural variations, as well as to oscillator probe placement. The second heat of material was welded in the unrecrystallized condition, which produced less grain refinement in the fusion zone than that seen previously, as shown in Figure 4. The arc oscillation sensitivity to probe placement is illustrated in Figures 5a and 5b. Note the symmetry in the columnar grains on the right side of the fusion zone, which indicates that the probe on that side of the weld was not optimally oriented. More experimentation is needed to optimize the probe placement for maximum fusion zone grain refinement. Also, because slight variations in composition may contribute to differences in the solidification behavior, both heats of material are currently undergoing detailed chemical analysis.

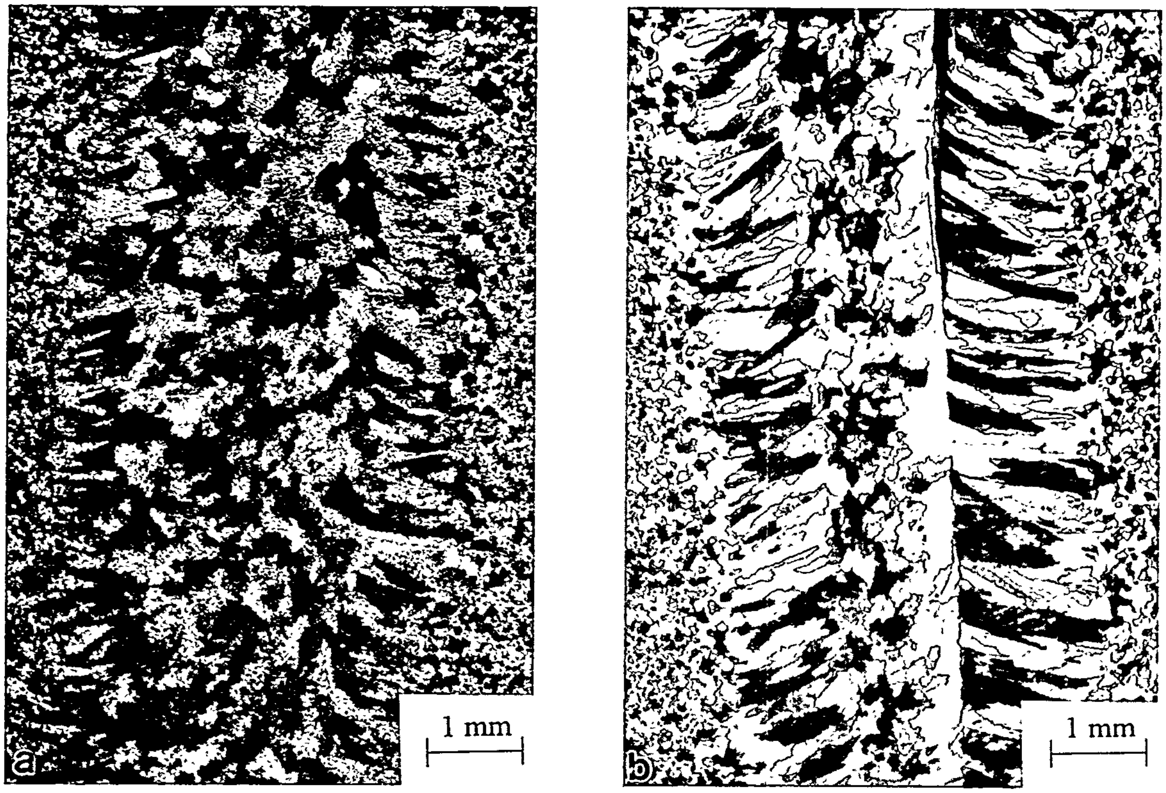

Figure 4. Sensitivity of base material condition on fusion zone grain refinement. a) heat #D5-3966-1, a recrystallized base material, and b) heat #D5-3969-1, an unrecrystallized base material.

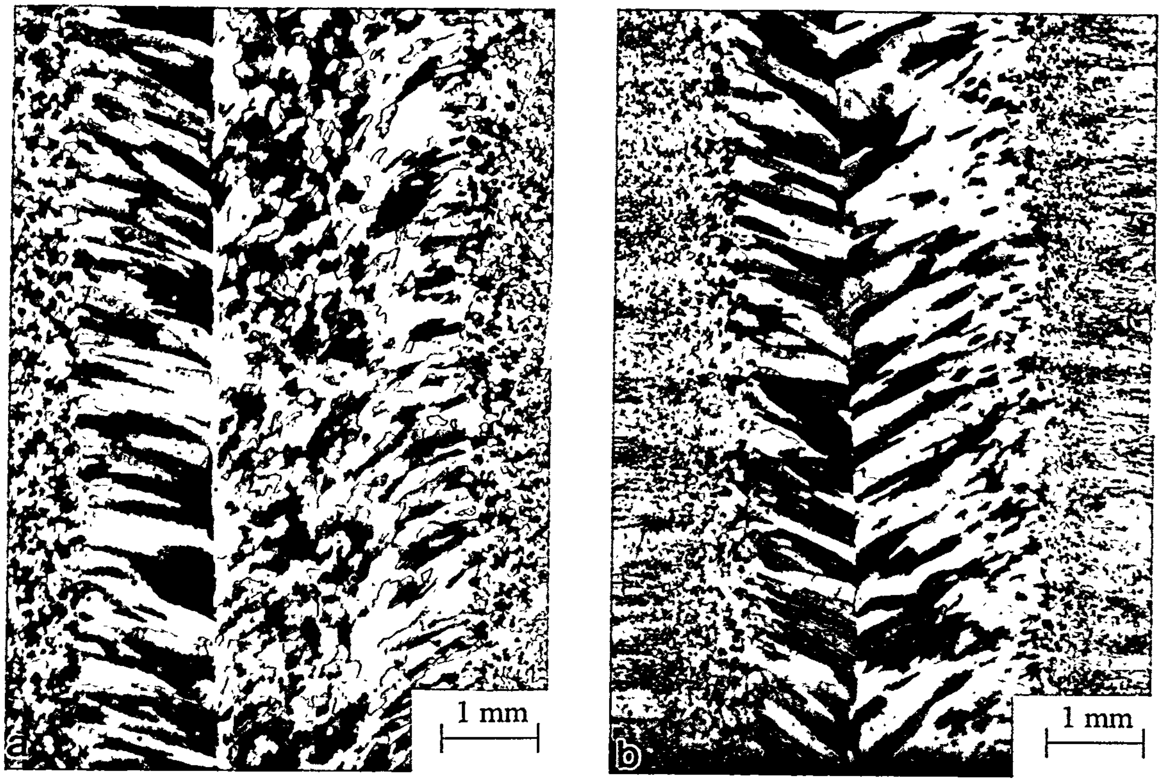

C

Figure 5. Sensitivity of oscillation probe position. a) heat #D5-3966-1, a recrystallized base material, and b) heat #D5-3969-1, an unrecrystallized base material.

After the oscillation process has been optimized, welds with nonrefined, partially refined and fully refined fusion zone microstructures will be produced in a range of water vapor atmospheres, and fusion zone fracture strength will be determined. From these data, the threshold water vapor concentration and the cold cracking susceptibility for each microstructure will be determined.

CONCLUSIONS

Magnetic arc oscillation has been shown to be an effective method for refining fusion zone microstructures in iron-aluminide alloy FA-129. The effectiveness of the fusion zone grain refinement due to arc oscillation is dependent upon the oscillation orientation and frequency, and the position of the oscillation probes. Effectiveness of oscillation may also be dependent upon the microstructural condition and the composition of the base material.

REFERENCES

1. David, S.A.; Zacharia, T.; Reed, R.W. 1990. Proceedings of Fourth Annual Conference on Fossil Fuel Materials ORNL/FMP-90/1: 207.

2. Chan, K.S. 1990. Theoretical analysis of grain size effects on tensile ductility. Scripta Metall. 24: 1725.

3. Schulson, E.M.; Barker, D.R. 1983. A brittle to ductile transition in NiAl of a critical grain size. Scripta Metall. 17: 519.

4. Cottrell, A.H. 1958. Theory of brittle fracture in steel and similar metals. Trans. AIME 121: 192.

5. Thompson, A.W.; Knott, J.F. 1993. Micromechanisms of brittle fracture. Met. Trans. A 24: 523.

6. Shiue, S. 1991. The effect of grain size on fracture: Dislocation-free zone in front of the finite crack tip. J. Appl. Phys. 70 (6): 2947.

ELECTRO-SPARK DEPOSITED COATINGS FOR FOSSIL ENERGY ENVIRONMENTS

R. N. Johnson

Westinghouse Hanford Company
P. O. Box 1970, L6-39
Richland, WA 99352

ABSTRACT

Electro-Spark Deposition (ESD) is a micro-welding process that uses short-duration, high-current electrical pulse to deposit or alloy an electrode material on a metallic substrate. The ESD process has been used to markedly improve the corrosion resistance and wear resistance of base metals by alloying appropriate materials into the surface. One of the most attractive developments has been the use of ESD to apply Fe_3Al- and FeAl-base materials to surfaces of iron alloys. The evolutionary developments of the aluminides as coatings include the further improvement in the sulfidation corrosion performance by the ESD addition of refractory metal diffusion barriers between the substrate metal and the aluminide coating and by ESD additions of modifying elements to an Fe_3Al or FeAl surface.

Developments are now in progress on titanium aluminide based coatings and on ORNL's new Cr-Nb intermetallic materials. The titanium aluminides are showing significant promise as a coating material. The Cr-Nb alloys are being evaluated not only as material for coatings but also for production of nanometer-sized particles using a modification of the ESD process.

Other advances include 1) the development of advanced robotics programs for automated ESD coating processes and 2) successful new applications being developed commercially through technology transfer activities.

INTRODUCTION

The objective of this program is to develop advanced materials coatings capable of operation in fossil energy environments beyond current materials limits, and to provide improvements in materials performance, durability and cost effectiveness for both new and existing power systems. Ultimately, new materials performance limits can enable new systems concepts.

A corollary objective is to further advance the Electro-Spark Deposition (ESD) technology and equipment, and to develop broad commercial applications through technology transfer activities.

The ESD process contributes a new dimension to materials for fossil energy applications by allowing the investigation of surface compositions that are difficult or impractical to achieve by other processes. A wide range of both stable and meta-stable surface alloys and structures can be produced by the ESD alloying and by the rapid solidification inherent in the process. Not only can the standard corrosion-resistant alloys be formed or deposited, for example, but it is also possible to apply refractory metal alloy diffusion barriers on the surface or between the substrate and primary corrosion protection coatings.

Coatings of current interest include single or multi-layer deposits of commercially available hardfacing alloys, as well as custom formulations of metal aluminides, chromium alloys, refractory metals, carbides, silicides, and borides. Materials to be protected include low alloy steels, Alloy 800, and various stainless steels, including the modified ("lean") stainless steels. Coatings will also be developed for use on the iron aluminides to further enhance their performance and to develop resistance to hydrogen embrittlement.

Background

Electro-spark deposition is a pulsed-arc micro-welding process that uses short-duration, high-current electrical pulses to weld a consumable electrode material to a metallic substrate. The short duration of the electrical pulse allows an extremely rapid solidification of the deposited material and results in an extremely fine-grained, homogeneous coating that may be amorphous for some materials. The microstructures produced by ESD can provide exceptional corrosion-resistance and wear-resistance for many materials.

The ESD process is one of the few methods available by which a fused, metallurgically-bonded coating can be applied with such a low total heat input that the bulk substrate material remains at or near ambient temperatures. This eliminates thermal distortions or changes in metallurgical structure of the substrate. Since the coating is metallurgically bonded, it is inherently more resistant to damage and spalling than the mechanically-bonded coatings produced by most other low-heat-input processes such as detonation gun, plasma spray, electro-chemical plating, etc. Nearly any electrically-conductive metal, alloy or cermet can be applied by ESD to metallic substrates.

Further background information on the ESD process is provided in Reference 1.

DISCUSSION OF PRIOR ACTIVITIES

Data collected so far indicate that ESD coatings tend to show lower corrosion rates in most environments than the same material would in either bulk form or as a coating applied by other processes. For example, ESD-applied coatings of chromium carbide-15% nickel exhibit significantly lower corrosion rates in aqueous and liquid metal environments than similar detonation-gun applied coatings.[2] The superior performance of the former is attributed to the extremely fine-grained, nearly amorphous structure inherent to the ESD coatings compared to the larger-grained, more heterogeneous detonation-gun coatings.

In tests at Argonne National Laboratory (ANL), this same ESD coating (chromium carbide-15% nickel) showed four times better sulfidation resistance than Type 310 stainless steel at 875°C.[3] Normally, this composition would not be expected to perform that well because of the strong susceptibility of a nickel matrix to sulfidation attack. Again, the fine grain structure is believed to be a major factor in the corrosion resistance. This observation is in agreement with other Fossil Energy Materials Program work that indicates one mechanism of improving lifetimes of protective oxide films and scales is to maintain as fine a grain structure as possible.[4] Further improvement in corrosion resistance of the chromium carbide coating was achieved by alloying aluminum into the surface by a further ESD treatment.[5]

One of the most significant advances in ESD coatings for use in sulfidation environments has been the successful development of Fe_3Al as a coating material. Oak Ridge National Laboratory (ORNL) has demonstrated the exceptional corrosion properties of Fe_3Al in bulk form, but alloying the Fe_3Al to achieve acceptable mechanical properties while maintaining optimum corrosion performance appears to be a challenge. As one alternative approach, ORNL supplied electrode materials to Westinghouse Hanford Company (WHC) for use in ESD coating development. (Using Fe_3Al as a coating material allows the selection of the substrate material for optimum mechanical properties and economy while retaining the corrosion resistance offered by the coating.) The coating results to date have been outstanding. The ESD parameters have been developed to the point that consistent, defect-free coatings over 100 μm thick can be applied relatively rapidly with good transfer efficiency. The Fe_3Al appears to produce some of the best coatings of all the materials evaluated for ESD application.

Further coating development is proving that the corrosion performance of the Fe_3Al coating can be significantly enhanced by the use of multi-layer ESD coating techniques. Sulfidation corrosion tests at ANL[5,6], for example, showed the beneficial effects of applying a Nb-1Zr diffusion barrier coating. The corrosion rate of an ESD coating of Fe_3Al was reduced by a factor of 2 in tests at 500°C when an intermediate ESD coating of Nb-1Zr was first applied to the steel, when compared to the same Fe_3Al coating applied directly to the steel.

Development efforts on further improvements in the Fe_3Al coatings have produced several new candidates which are now in corrosion evaluation at ANL. The new coatings represent various combinations of Fe_3Al with Nb or Mo diffusion barriers, and Pt or Pd surface treatments, all applied to Type 316 SS or Alloy 800 substrates. These and other coatings in development will be used to evaluate the relative effectiveness of the various refractory metals as diffusion barrier coatings for their contribution to the corrosion performance. The surface treatments with Pt and Pd are based on gas turbine coating experience demonstrating that light alloying additions of platinum to aluminide coatings increase the stability and life of protective oxide film formation. (In fact, the ESD process is being used commercially to economically apply Pt to gas turbine components.)

DISCUSSION OF CURRENT ACTIVITIES

Improved Iron Aluminide Coatings

Analyses of the Fe_3Al coatings with and without the Nb-1Zr diffusion barrier coating led to the conclusion that one of the principal reasons for the improved corrosion performance of the Fe_3Al coating over the Nb-1Zr layer was the higher aluminum content of the coating surface.[7] Scanning Electron Microprobe (SEM) analyses showed that the intermediate diffusion barrier reduced the dilution of substrate elements into the coating weld zone and resulted in about 50% more aluminum in the surface of the coating (15% vs 9.5%).

After attempting unsuccessfully to alloy aluminum into the Fe_3Al surface by ESD treatments without generating surface cracks[8], we obtained rods of FeAl from ORNL. This material proved to be nearly ideal for further increasing the aluminum content of the ESD coatings.

We have now produced Fe_3Al coatings as thick as 100 μm deposited on Type 316 stainless steel and on Alloy 800 with none of the cracking defects that were observed when aluminum electrodes were used.

Six new candidate metallurgical coatings were successfully developed for testing in fossil energy environments. The coatings consist of various combinations of Fe_3Al, FeAl, Nb, and Mo, applied to Type 316 stainless steel substrates. The Nb and Mo represent refractory metal diffusion barriers applied between the stainless steel substrate and the iron aluminide coating to inhibit the diffusion of nickel to the surface and the diffusion of sulfur or oxygen to the substrate, both of which are mechanisms of corrosion failure. The application of the diffusion barrier also reduces the weld dilution effects during the coating process and results in the surface composition of the coating more nearly approaching the composition of the electrodes used.

Test specimens of the advanced coatings were delivered to Argonne National Laboratory for corrosion testing in fossil energy environments.

The success of using FeAl as a coating material now opens the potential for further improving the performance of Fe_3Al alloys. The Fe_3Al alloys so far can provide better mechanical properties in structural applications than FeAl, while an FeAl coating could improve the corrosion performance in applications where the higher aluminum content is desirable. It is possible such treatments could also improve the resistance of Fe_3Al to hydrogen embrittlement (described by McKamey and Liu[9]). Plate or sheet substrates of Fe_3Al have been requested from ORNL for further exploration of these potential improvements.

New Intermetallic Materials

Experimental titanium aluminide alloys were obtained from Michigan Technology University for coating evaluations. The intermetallics consist of $Ti_{25}Al_{67}Cr_8$ and $Ti_{25}Al_{65}Cr_{10}$ and are showing promise as coating materials.

Specimens of a Cr-Nb intermetallic alloy developed by ORNL were also obtained and are being evaluated in coating experiments and in nano-particle production trials.

Nano-particle Production

Experiments were conducted to determine the feasibility of producing sub-micron or nano-meter size particles of metals using a modified ESD process. We had observed the production of extremely fine powders as a by-product of some coating conditions. In the initial feasibility tests, we used tungsten and iron aluminide to produce powders under several conditions. Analyses showed a significant distribution of particles in the 10 to 100 nm size range, indicating the process is a good candidate for further investigation and development.

The next experiments in nano-particle production will involve ORNL's chromium-niobium intermetallic alloys. The fabrication of acceptable components from this promising material may depend on the ability of the fabricators to achieve a very small grain size. Nanometer sized powders would be a desirable starting material for that development.

ESD Equipment Improvements

An advanced computer program for the automated control of the robotics used in the ESD coating process was developed. The next phase of development to expand control to other micro-welding process parameters is in progress.

Technology Transfer Activities

Technology transfer activities now include discussions in progress with a steam turbine manufacturer on the potential use of ESD coatings in a new power system being designed. Coatings resistant to corrosion, erosion, wear, and thermal cycling are required. Some of the ESD coatings developed to date in the Fossil Energy Materials Program are among the candidates for this application.

Other technology transfer activities included

1) Consultations with a major airline manufacturer on potential uses of ESD coatings to provide protection to titanium components on advanced aircraft,
2) Samples of corrosion and wear-resistant coatings to Bettis Atomic Power Laboratory for evaluations, and
3) Consultations on materials and coatings for use in protection of 2.25Cr-1Mo steel heat exchanger tubes in an 0.1 refinery catalyst bed.

REFERENCES

1. R. N. Johnson, "Principles and Applications of Electro-Spark Deposition," Surface Modification Technologies, T. S. Sudarshan and D. G. Bhat, eds., The Metallurgical Society, January 1988, pp. 189-213.

2. R. N. Johnson, "Coatings for Fast Breeder Reactors," in Metallurgical Coatings, Elsevier Sequoia, S. A., New York, 1984, pp. 31-47.

3. K. Natesan and R. N. Johnson, "Corrosion Resistance of Chromium Carbide Coatings in Oxygen-Sulfur Environments," Surface and Coatings Technology, Vol, 33, 1987, pp. 341-351.

4. I. G. Wright and J. A. Colwell, "A Review of the Effects of Micro-Alloying Constituents on the Formation and Breakdown of Protective Oxide Scales on High Temperature Alloys at Temperatures Below 700°C," ORNL/Sub/86-57444/01, September 1989.

5. K. Natesan and R. N. Johnson, "Development of Coatings with Improved Corrosion Resistance in Sulfur-Containing Environments," presented at the International Conference on Metallurgical Coatings, San Diego, April 1990, published in Surface and Coatings Technology, Vol. 3/44, 1990, pp. 821-835.

6. R. N. Johnson, "Electro-Spark Deposited Coatings for Protection of Materials in Sulfidizing Environments," Proceedings of the Fourth Annual Conference on Fossil Energy Materials, ORNL/FMP-90/1, August 1990, pp. 321-329.

7. R. N. Johnson, "Electro-Spark Deposited Coatings for Protection of Materials in Sulfidizing Atmospheres," Proceedings of the Fifth Annual Conference on Fossil Energy Materials, ORNL/FMP-91/1, September 1991, pp. 281-288.

8. R. N. Johnson, "Electro-Spark Deposited Coatings for Fossil Energy Environments," in Proceedings of the Seventh Annual Conference on Fossil Energy Materials, ORNL/FMP-93/1, July 1993, pp. 289-295.

9. C. G. McKamey and C. T. Liu, "Environmental Embrittlement of Iron Aluminides in Moisture-Containing Atmospheres", in Proceedings of the Environmental Effects on Advanced Materials, NACE Conference, June 1991.

HIGH TEMPERATURE CORROSION OF IRON ALUMINIDES*

K. Natesan and W. D. Cho
Energy Technology Division
Argonne National Laboratory
Argonne, IL 60439

ABSTRACT

Iron aluminides are being developed for use as structural materials and/or cladding alloys in fossil energy systems. Extensive development has been in progress on Fe_3Al-based alloys to improve their engineering ductility. This paper describes results from an ongoing program to evaluate the corrosion performance of these alloys. The experimental program at Argonne National Laboratory involves thermogravimetric analyses of alloys exposed to environments that simulate coal gasification and coal combustion. Corrosion experiments were conducted to determine the effect of gas flow rate and different levels of HCl at a gas temperature of 650°C on three heats of aluminide material, namely, FA 61, FA 129, and FAX. In addition, specimens of Type 316 stainless steel with an overlay alloying of iron aluminide were prepared by electrospark deposition and tested for their corrosion resistance. Detailed microstructural evaluations of tested specimens were performed. The results are used to assess the corrosion resistance of various iron aluminides for service in fossil energy systems that utilize coal as a feedstock.

INTRODUCTION

Iron aluminides are being developed as structural materials for application in fossil energy systems because of their relatively low cost, and their lower content of strategic elements and lower density than austenitic alloys. Several compositions of iron aluminides have been produced by Oak Ridge National Laboratory, with emphasis on improvements in mechanical properties, especially room-temperature ductility and high-temperature strength. Several possible applications for ductile iron aluminides were presented in a review paper by McKamey et al.[1] A valuable attribute of iron aluminides is their resistance to corrosion in a variety of complex environments that are prevalent in coal-fired energy systems.

The purpose of the present study is to examine the corrosion resistance of iron aluminides in simulated coal-gasification and -combustion environments of interest in development of fossil energy systems. In coal gasification, the environment is low in

---

*Work supported by the U.S. Department of Energy, Office of Fossil Energy, Advanced Research and Technology Development Materials Program, Work Breakdown Structure Element ANL-3, under Contract W-31-109-Eng-38.

oxygen partial pressure (pO_2) and moderate-to-high in sulfur partial pressure (pS_2), and the sulfur is present as H_2S. In the combustion environment, especially in fluidized-bed and pulverized-coal-fired systems, pO_2 is generally high and pS_2 is low, and the sulfur is present as SO_2. The implications of the gas chemistries on the corrosion of structural materials can be examined with a pO_2-pS_2 and pO_2-pCl_2 thermochemical diagram (shown in Fig. 1 for metal temperature of 650°C). In addition, the effect of chlorine-containing environments on the corrosion performance of iron aluminides is of interest as more and more higher-Cl coals are used as a feedstock. Earlier, corrosion resistance of three heats (FA 41, FA 61, and FA 81) of Fe aluminides was evaluated and corrosion performance was compared with the corrosion performance of Type 310 stainless steel and several alumina-forming structural/cladding alloys.[2,3] The test data obtained over a temperature range of 650-1000°C showed that the aluminides developed predominantly thin alumina scales and exhibited some propensity to spallation; however, the aluminides exhibited superior corrosion resistance in high-S atmospheres (typical of those produced by high-S coal feedstock) and O/S mixed-gas environments relative to the catastrophic corrosion of Type 310 stainless steel.

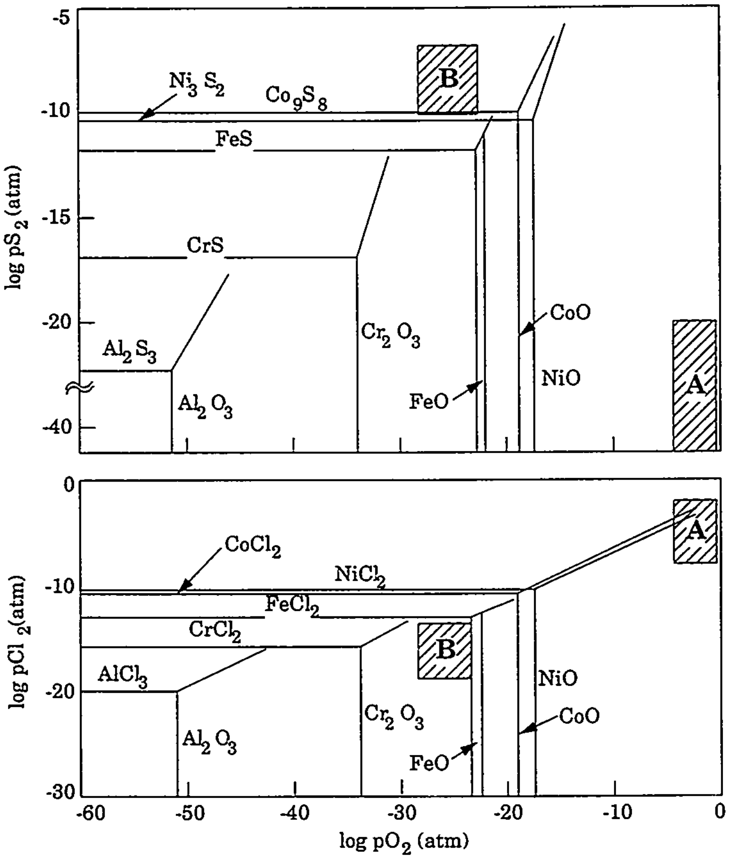

Figure 1.
Oxygen/sulfur and oxygen/chlorine thermochemical diagrams for several metals, calculated for temperature of 650°C. Also shown are regimes of (A) combustion and (B) gasification conditions.

The corrosion resistance of Fe aluminides, however, has not been studied in environments that contain O_2 and HCl, which is encountered in many metallurgical/chemical processes and in fossil energy systems. It is known[4] that halogen gases such as Cl_2 and HCl react with metals to form volatile metal halides and result in severe high-temperature corrosion. Hydrogen chloride-induced corrosion of materials is very complex because it often involves simultaneous diffusional growth and evaporation of corrosion products due to the high vapor pressure of metal chlorides. The phenomena of simultaneous formation and volatilization of the products is often expressed by a paralinear rate equation that was originally developed by Tedmon.[5] The rate equation for the change of scale thickness is

$$\frac{dx}{dt} = \frac{k_d}{x} - k_s \tag{1}$$

where x is the scale thickness, k_d is the parabolic rate constant that implies an increase in weight gain of a specimen, and k_s is a linear rate constant for a decrease in weight gain of a specimen due to volatilization. The integration of Eq. 1 with the boundary condition, $x = 0$ at $t = 0$, yields

$$t = \frac{k_d}{k_s^2}\left[-\frac{k_s}{k_d}x - \ln\left(1 - \frac{k_s}{k_d}x\right)\right]. \tag{2}$$

Mayer and Manolescue[6] and Miller[7] have reported that the corrosion rate of boiler steels in incinerators increases with increasing HCl concentration in the flue gas, which was associated with changes in scale morphology. The continuity of the stratified oxide scale is destroyed because of interaction with HCl and formation of volatile compounds. The purpose of this study is to evaluate the corrosion performance of Fe aluminide materials in S- and Cl-containing environments. Results from the continued study are discussed in this paper.

EXPERIMENTAL PROCEDURE

Sheets of Fe_3Al and Fe_3Al-based materials were procured from Oak Ridge National Laboratory. The sheet materials were annealed at 750°C for 1 h followed, by oil quenching. Coupon specimens were cut from the sheet material for thermogravimetric experiments. The compositions of the investigated alloys are given in Table 1.

The thermogravimetric experiments were performed with an electrobalance with a sensitivity of 0.1 μg. The specimens were suspended from the balance in a vertical furnace and held for a desired exposure period. An appropriate reacting gas, HCl/N_2, was introduced into the reaction tube at several predetermined flow rates, which were

Table 1. Nominal chemical composition (wt.%) of alloys used in corrosion tests

Material	Cr	Al	Fe[a]	Other
FA 61	-	13.9	Bal.	-
FA 71	5.5	15.9	Bal.	-
FA 81	2.2	15.9	Bal.	B 0.01
FA 129	5.5	15.9	Bal	Nb 1.0, C 0.05
FAX	5.5	15.9	Bal.	Nb 1.0, Mo 1.0, Zr 0.15, B 0.04
Fe_3Al	Overlay coating on Type 316 SS with Fe_3Al weld rod			
Fe-Al	Overlay coating on Type 316 SS with FeAl weld rod			

[a] Bal. = balance.

controlled by flow meters calibrated by the standard soap bubble method. Oxygen was an impurity in the gas mixture and was maintained at a ppm level. Upon completion of the corrosion test, the furnace was opened and the specimen was rapidly cooled in the reaction gas mixture. Most of the specimens were subjected to corrosion for 48 h at 650°C.

Following thermogravimetric measurement of corrosion, the scales of corrosion product and cross sections of specimens were examined with a scanning electron microscope equipped with an energy-dispersive X-ray (EDX) analyzer.

RESULTS AND DISCUSSION

Fe_3Al System

Corrosion tests on Fe_3Al were conducted under different experimental conditions, which included variations in partial pressure of HCl and gas flow rate. The effect of gas flow rate, namely 20, 60, 110, and 250 mL/min, on the kinetics of corrosion of Fe_3Al is presented in Fig. 2 in plots of weight change/unit area versus time. The temperature of the specimens was maintained constant at 650°C.

As shown in Fig. 2, three distinct patterns of weight change during corrosion were observed, depending on the gas flow rate. At a gas flow rate of 20 mL/min, a continuous weight gain was observed, whereas at a gas with a flowrate of 250 mL/min, the weight of the specimen decreased. At intermediate gas flow rates, there was an initial weight gain followed by a linear loss in weight. After a certain period of time, for instance ≈8 h at a flow rate of 250 mL/min, specimens from all of the tests (except that exposed to a 20 mL/min flow rate) showed negligible weight change. The steady-state condition of negligible weight change was reached more quickly at higher gas flow rates.

Figure 3 is a parabolic plot of the square of weight change/unit area versus time for a specimen exposed to a gas flow rate of 20 mL/min: the plot follows parabolic growth kinetics. The measured parabolic rate constant k_p from the equation,

$$\frac{(\Delta W)^2}{A} = k_p t \, , \qquad (3)$$

is 3.3×10^{-5} mg^2 cm^{-4} s^{-1}.

Scanning electron microscopy (SEM) and EDX analysis of the surface and cross section of the corroded specimen exposed to the 20 mL/min flow rate showed that the exterior Fe_2O_3 layer had cracked and spalled while the interior appeared to be $FeAl_2O_4$. With the gas flow rate of 20 mL/min, no metal chloride was detected in the scale, a circumstance that suggests that HCl may not have any effect on the corrosion of Fe_3Al under the low flow rate conditions of the experiment. At intermediate gas flow rates, the corrosion behavior of Fe_3Al was different from that at low flow rates. The specimen initially gained weight but after a short time, linear loss of weight was observed. The initial weight increase may stem from the formation of $FeCl_2$(s) on the surface of the Fe_3Al by the following reaction:

$$Fe\,(s) + 2\,HCl = FeCl_2(s) + H_2(g).$$

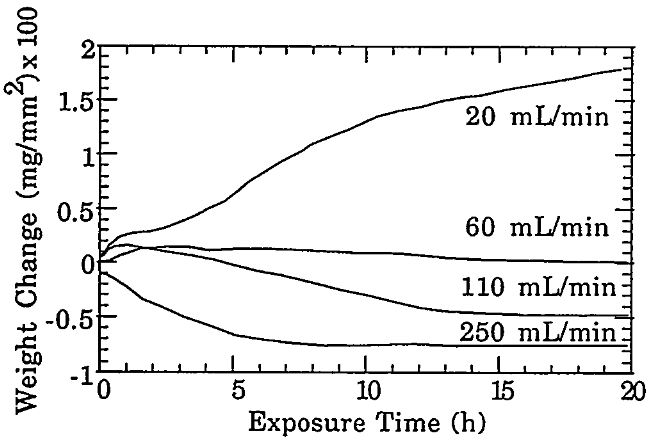

Figure 2.
Effect of gas flow rate on the corrosion of Fe_3Al exposed to 1 vol.% HCl-N_2 gas mixture at 650°C.

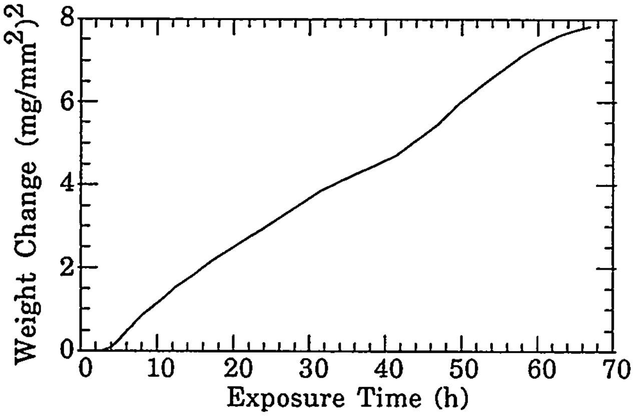

Figure 3.
Parabolic plot of square of weight change per unit area versus time for Fe_3Al exposed at 650°C to 1 vol.% HCl-N_2 gas mixture at a flow rate of 20 mL/min.

The subsequent weight loss may indicate vaporization of $FeCl_2$. This observation is similar to that found by Fruehan et al.[8] in the study of the reaction of iron with Ar-HCl mixtures at 540-900°C. Under their experimental conditions, equilibrium vapor pressure of $FeCl_2$ was much higher than that of $FeCl_3$. They found that, at lower temperatures and higher HCl pressures, the condensed-phase $FeCl_2(s)$ formed and the rate of steady-state weight loss was controlled by diffusion of $FeCl_2(g)$ through the gas film boundary layer.

At a gas flow rate of 250 mL/min, there was no increase in weight during the initial stage of corrosion, indicating absence of an $FeCl_2$ layer. After a certain amount of weight loss, the specimens exhibited a plateau in weight change for longer times because of the formation of a protective alumina scale. EDX data for the cross sections of the three specimens at higher flow rates showed Al_2O_3 scale on the surface of the Fe_3Al and depletion of Fe in the substrate near the alumina/substrate interface. Also, the rate of weight loss decreased with time, which implies gradual coverage with Al_2O_3 scale. Therefore, it can be concluded that as vaporization of Fe chloride proceeds, the surface of the specimen develops an aluminum-rich, protective alumina scale.

Data from corrosion tests conducted at three different HCl concentrations in the gas phase, 0.1, 1.0, and 10 vol.% $HCl-N_2$ gas mixtures at a flow rate of 110 mL/min are presented in Fig. 4. In the gas mixtures that contained 1 and 10% HCl, the specimens initially gained weight, presumably due to formation of an $FeCl_2$ layer on the surface of the Fe aluminide. The extent of initial weight increase is dependent on the partial pressure of HCl. Also, after a certain amount of weight gain, both specimens exhibited linear weight loss. This weight loss is much more evident for the specimen tested in 10 vol.% HCl in the gas mixture. The specimen exposed to 0.1 vol.% $HCl-N_2$ gas mixture showed negligible initial weight gain, indicating that the rate of evaporation of $FeCl_2$ may have been faster than the rate of growth of the $FeCl_2$ layer. After an initial weight gain period for specimens exposed to 1 and 10 vol.% HCl, the rate of weight loss follows a linear rate law,

$$-\frac{\Delta W}{A} = k_v t, \tag{4}$$

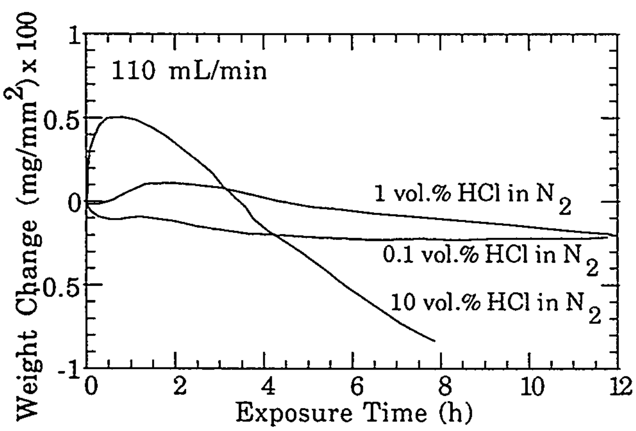

Figure 4.
Effect of partial pressure of HCl on corrosion behavior of Fe_3Al at 650°C.

where k_v is a linear rate constant. The rate of decrease in weight is higher for specimens tested in a gas mixture with higher HCl concentration. Therefore, it appears that at higher HCl concentrations the rate is controlled by surface chemical reactions. The linear rate constant for specimens tested in 10 vol.% HCl was 6.1×10^{-6} mg cm^{-2} s^{-1}. The corrosion of Fe_3Al in a gas mixture containing 1 vol.% HCl during the first few hours of exposure showed paralinear kinetics, which are the result of simultaneous presence of parabolic scale growth and linear evaporation of $FeCl_2$. The paralinear kinetic behavior has been observed for other simultaneous oxidation-volatilization processes.[5,9] After a sufficiently long corrosion time, the rate of linear weight loss decreased and eventually almost no weight change was observed. EDX analysis showed the surface layer to be alumina. Therefore, the decrease in linear rate can be characterized by simultaneous formation of alumina and evaporation of $FeCl_2$.

Fe_3Al-based Alloys

The Fe_3Al-based alloys containing alloying elements such as Cr, B, Nb, C, Mo, and Zr, were tested for ≈48 h at a flow rate of 110 mL/min in 1 vol.% HCl-N_2 gas mixture at 650°C. The compositions of the tested alloys are given in Table 1. Figure 5 represents weight change of the alloy specimens during the corrosion tests. The figure clearly shows that, depending on their Cr content, the alloys either lose or gain weight under the same experimental conditions. A comparison of the weight changes of the binary alloy FA 61 and the C- containing alloy FA 81 shows that FA 81 loses less weight during the period of exposure used in the present study. Furthermore, alloys containing 5.5 wt.% Cr show positive weight change during the tests. Therefore, it can be concluded that there a critical concentration of Cr may control the general corrosion behavior of Fe_3Al-based alloys in HCl-containing environments. For application in coal-gasification and -combustion environments, corrosion performance of these multicomponent alloys must be evaluated in environments that contain both sulfur and chlorine.

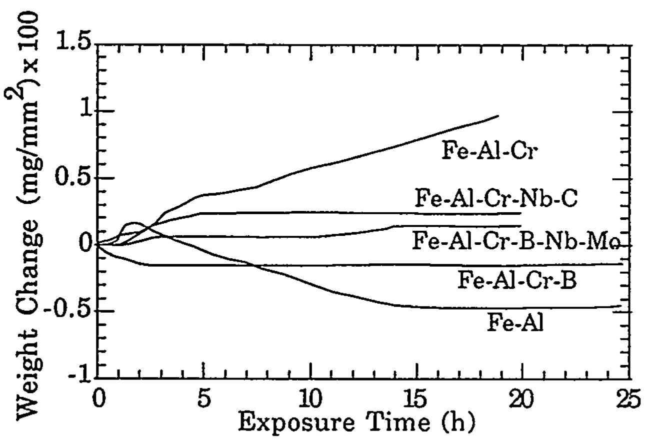

Figure 5.
Thermogravimetric test data for Fe_3Al-based alloys tested in 1 vol.% HCl-N_2 gas mixture at 650°C.

Deposition of Iron Aluminides

From the corrosion standpoint, it is desirable to apply a layer of Fe aluminide that possesses adequate corrosion resistance to enhance the service life of structural components. For this purpose, the electrospark deposition (ESD) process was used to apply layers of Fe_3Al and FeAl-type compositions onto a substrate of Type 316 stainless steel. The ESD process is a microwelding technique that uses short-duration, high-current electrical pulses to deposit an electrode material on a metallic substrate. A principal advantage of ESD is that the coatings are fused to a metal surface with low heat input while the bulk substrate material remains at ambient temperature. This eliminates thermal distortions or changes in the metallurgical structure of the substrate. Because the coating is alloyed with the surface, i.e., metallurgically bonded, it is inherently more resistant to damage and spalling than the mechanically bonded coatings produced by most other low-heat-input processes (such as detonation-gun, plasma-spray, and electrochemical plating).

Several coatings were applied on Type 316 stainless steel and Alloy 800 substrate alloys by the ESD technique and tested in simulated gasification or combustion environments that contained H_2S/SO_2 with or without HCl. The coatings on Type 316 stainless steel were prepared from either an Fe_3Al or an FeAl weld rod. Coatings made with FeAl weld rod were much higher in Al content than those made with Fe_3Al weld rod. The calculated chemistries of gas mixtures used in gasification and combustion simulation experiments are listed in Table 2. The coated and uncoated specimens were exposed to these environments for time periods up to 1000 h and were periodically retrieved to measure weight changes at intermediate exposure times. Figures 6A and B show the weight change data for Type 304 and 316 stainless steel and for Fe_3Al- or FaAl-coated Type 316 stainless steel after exposure at 650°C to simulated gasification environments with or without HCl. The uncoated alloys exhibited some general corrosion but significant sulfidation and localized pitting corrosion. The aluminide-coated specimens showed weight gains and the scaling rate was much lower than that for uncoated alloys. The figure shows two curves for Fe_3Al coated specimens that were fabricated at different times and tested in the same environments but at different times. The weight-change data for the two specimens are similar which indicates that the corrosion performance of these coated alloys is reproducible and that substantial improvement in corrosion resistance can be achieved by surface coating of structural alloys.

Table 2. Calculated chemistries of gas mixtures used in experiments at 650°C

Test condition	pO_2 (atm)	pS_2 (atm)	pCl_2 (atm)	pSO_2 (atm)	pHCl (atm)
Gasification (G)	1.5×10^{-23}	5.6×10^{-10}	-	1.3×10^{-11}	-
Combustion (C)	6.7×10^{-3}	1.4×10^{-35}	-	1.2×10^{-3}	-
(G) with HCl	1.2×10^{-23}	5.2×10^{-10}	1.5×10^{-23}	9.1×10^{-12}	2.1×10^{-3}
(C) with HCl	4.9×10^{-3}	1.6×10^{-35}	1.5×10^{-23}	9.1×10^{-4}	1.7×10^{-3}

Figures 7A and B show the weight change data for Type 304 and 316 stainless steel and for Fe$_3$Al- or FaAl-coated Type 316 stainless steel after exposure at 650°C to simulated combustion environments with or without HCl. In the absence of HCl, the uncoated alloys developed scales of (Fe, Cr) oxide or Fe oxide and they tended to crack and spall as evidenced by weight loss in Fig. 7. However, the absolute values for weight change after 900 h of exposure is small, i.e., in the range of 0.01-0.016 mg/mm^2. The aluminide-coated alloys showed a small weight gain due to the development of a thin, adherent alumina scale. In the presence of HCl, both the uncoated and coated alloys showed substantial weight loss at 650°C. The attack was most notable in Fe$_3$Al-coated alloy, less notable in the uncoated alloys, and least notable in FeAl-coated alloy. The primary cause for the increased corrosion of Fe$_3$Al-coated alloys seems to be due to a low concentration of Al in the coating that resulted from dilution of the deposit layer with substrate constituents. Even though

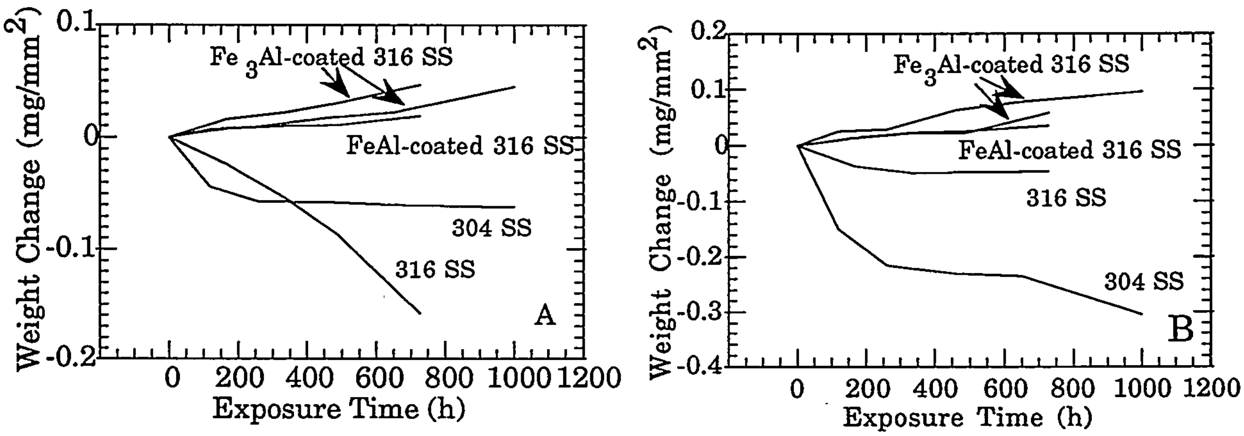

Figure 6. Weight change data for base and aluminide coated alloys tested at 650°C in simulated gasification atmospheres (A) without and (B) with HCl.

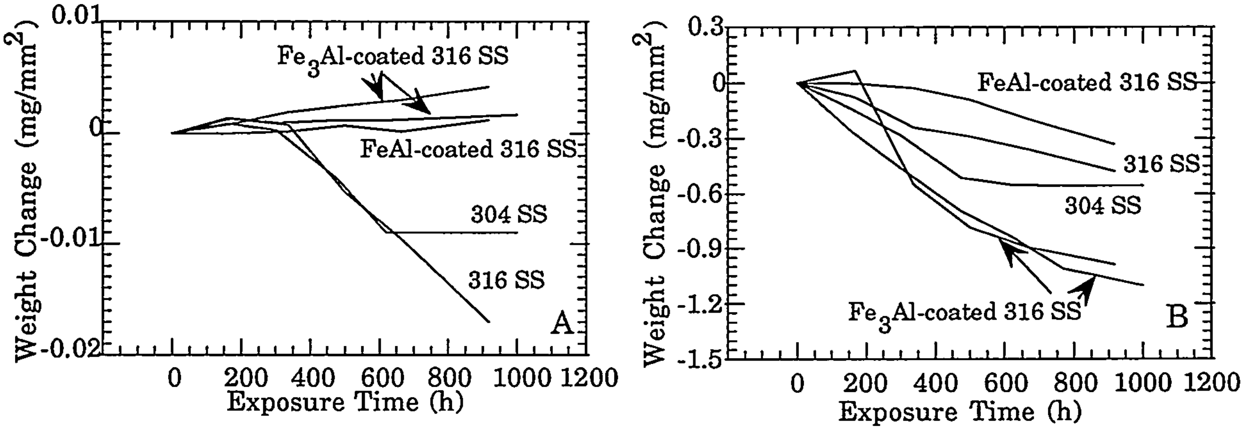

Figure 7. Weight change data for base and aluminide coated alloys tested at 650°C in simulated combustion atmospheres (A) without and (B) with HCl.

Fe_3Al contains ≈15 wt.% Al, the coated alloy contained <8 wt.% Al after fabrication. The results also indicate that a threshold Al concentration may be present for obtaining improvements in corrosion resistance of the structural alloys.

The performance of the ESD coatings (which included Fe_3Al with different bond coats of refractory metals and/or overlay coatings of noble metals) on Type 316 stainless steel and Alloy 800 was compared with that of uncoated austenitic alloys.[10] Figure 8 shows corrosion loss data obtained for specimens tested for 1000 h at 650°C in gasification environment with and without HCl. The weight change data and extensive microscopic analyses of tested specimens showed that the bond coats themselves do not significantly influence the corrosion process. All of the tested Fe aluminide coatings were resistant to sulfidation and chloride attack, whereas the base alloys were susceptible to general corrosion and pitting attack, especially in the HCl-containing environment.

SUMMARY

The corrosion performance of Fe_3Al, FeAl, and Fe_3Al-based alloys was evaluated for application in coal gasification and combustion environments. Experiments conducted at 650°C showed that the gas flow rate significantly affects the corrosion product morphology, especially when the gas contains HCl. Several different types of kinetic behavior were observed, including parabolic, paralinear, and simple vaporization. Hence, three modes of weight change were observed: continuous weight gain, initial weight increase followed by weight loss, and continuous weight loss, depending on the gas flow rate. Except for the specimen exposed to alow gas flow rate, the product scale was found to be protective alumina. Similar kinetic patterns were obtained with different HCl partial pressures, indicating that the corrosion process was controlled by surface chemical reactions. Alloys such as FAX and FA 129 exhibited better corrosion resistance in HCl-containing environments in the absence of S than in its presence. The Cr content of the alloy played a

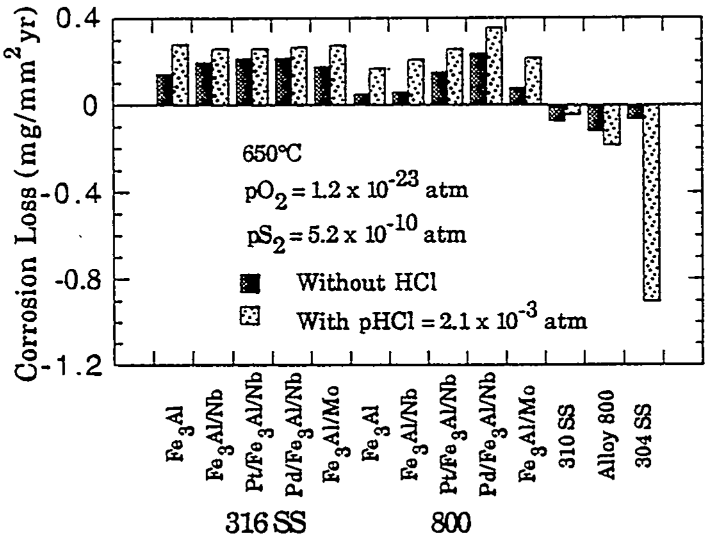

Figure 8.
Corrosion loss data for several iron aluminide coatings and uncoated austenitic alloys after exposure in gas mixtures containing H_2S with and without HCl.

critical role in its corrosion behavior. At 650°C, aluminides exhibited negligible corrosion in both gasification and combustion gas environments in the absence of HCl. Both Fe_3Al and FeAl layers on Type 316 stainless steel improved corrosion resistance of the alloy in a gasification environment with a nominal HCl concentration. In the HCl-containing combustion environment, the Fe_3Al layer exhibited severe corrosion but FeAl reduced corrosion. The effect of bond coat composition on the corrosion process was negligible when Fe_3Al coatings with several bond layers were tested in gasification environments.

REFERENCES

1. C. G. McKamey, J. H. DeVan, P. F. Tortorelli, and V. K. Sikka, A Review of Recent Developments in Fe_3Al–based Alloys, J. Mater. Res. 6, 1779, 1991.

2. K. Natesan, Corrosion Resistance of Iron Aluminides, Proc. 6th Annual Conf. on Fossil Energy Materials, ORNL/FMP–92/1, p. 271, 1992.

3. K. Natesan, Corrosion Performance of Iron Aluminides, Proc. 7th Annual Conf. on Fossil Energy Materials, ORNL/FMP–93/1, p. 249, 1993.

4. M. G. Fontana and R. W. Staehle, eds., Advances in Corrosion Science and Technology, Vol. 5, Plenum Press, New York, 55, 1976.

5. C. S. Tedmon, Jr., The Effect of Oxide Volatilization on the Oxidation Kinetics of Cr and Fe-Cr Alloys, J. Electrochem. Soc. 113, 766, 1966.

6. P. Mayer and A. V. Manolescu, Influence of Hydrogen Chloride on Corrosion of Boiler Steels in Synthetic Fuel Gas, Corrosion, 36, 369, 1980.

7. P. D. Miller, The Mechanism in High-Temperature Corrosion in Municipal Incinerators, Corrosion 28, 274, 1972.

8. R. J. Fruehan and L. J. Martonik, The Rate of Chlorination of Metals and Oxides: Part II, Iron and Nickel in HCl(g), Metall. Trans. 4, 2789, 1973.

9. N. J. Jacobson, M. J. McNallan, and Y. Y. Lee, The Formation of Volatile Corrosion Products During the Mixed Oxidation-Chlorination of Cobalt at 650°C, Metall. Trans. 17A, 1223, 1986.

10. K. Natesan, Surface Modification for Corrosion Resistance, Mater. High Temp. 11, 36, 1993.

ELASTIC BEHAVIOR OF NICKEL ALUMINIDE AND IRON ALUMINIDE-BASED INTERMETALLICS

M.N. Srinivasan*, S. Manjigani*, A. Wolfenden*
and V.K. Sikka**

***Department of Mechanical Engineering**
Texas A&M University
College Station, TX 77843-3123

****Metals and Ceramics Division**
Oak Ridge National Laboratory
Oak Ridge, TN 37831

ABSTRACT

The elastic and torsion modulus of five different grades of nickel aluminide and four different grades of iron aluminide at different temperatures are reported in this paper. The instrument used for this purpose is the Piezoelectric Ultrasonic Composite Oscillator Technique (PUCOT).

INTRODUCTION

Both nickel and iron aluminides are intermetallic compounds, which are candidate materials for high temperature applications. The compositions of these aluminides have been modified to serve different purposes, at Oak Ridge National Laboratory, so that different grades of these aluminides are now available. Since these are structural materials, knowledge of the elastic properties of these materials at different temperatures is essential. Prior to this study, there was no information available on the elastic behavior of the aluminides developed at Oak Ridge National Laboratory. The information presented in this paper, therefore, bridges an important gap in knowledge.

The technique used for the determination of the Young's modulus and the torsion modulus has been described earlier [1]. The experimental set up consists of piezoelectric quartz gage and drive crystals. In this work the frequency used was 100 kHZ for the determination of the Young's modulus and 80 kHz for the determination of the torsion modulus. For temperatures above ambient, a fused quartz crystal tuned to the appropriate frequency was interposed between the specimen and the gage crystals, so as to protect the gage crystal from the heating furnace.

EXPERIMENTAL

The compositions of the nickel and iron aluminides whose elastic moduli were determined are shown in Table 1 and Table 2 respectively.

Table 1 - Composition of Nickel Aluminides[2]

NiAl-82	5794	49.5	-	-	0.4	0.7	Bal
NiAl (P/M)	5903	31.5	-	-	-	-	Bal
IC-218 LZr	7731	8.69	8.08	0.02	0.2	-	Bal
IC-221 M	7805	7.98	7.74	0.008	1.70	1.43	Bal
IC-50	7626	11.3	-	0.02	0.60	-	Bal

Table 2 - Composition of Iron Aluminides[3]

Alloy	Den kg/m^3	Al,%	Cr,%	B,%	Zr,%	Mo,%	C,%	OE,%
FAPY	7024	8.5	5.5	-	0.2	2.0	0.03	0.1Y
FAS	6556	15.9	2.2	0.01	-	-	-	-
FAL	6560	15.9	5.5	0.01	0.15	-	-	-
FA-129	6536	15.9	5.5	-	-	-	0.05	1.0Nb

Note: The balance is Iron. OE: Other elements. All are in wt.%

The initial length of the specimen is calculated using the formula:

$$l = (\tau/2)(E/\rho)^{1/2} \qquad (1)$$

Where, l is the length
τ is the frequency
E is the estimated Young's modulus
ρ is the density

The subsequent procedures are shown in the flow chart (Fig. 1).

The same principles are used for the torsional modulus calculation, except that torsional waves are used instead of longitudinal waves.

RESULTS AND DISCUSSION

In Fig. 2 and Fig. 3 are shown the variation of Young's and torsion modulus with temperature for nickel aluminides, while in Fig. 4 and Fig. 5 are shown the corresponding figures for iron aluminides.

It is seen from Fig. 2 and Fig. 4 that the Young's modulus decreases with temperature for both nickel and iron aluminides, but in general, the drop in the case of nickel aluminides is smaller for a given range of temperature. In particular, IC-218 LZr, NiAL (P/M) and NiAl-82 show relatively high Young's modulus values at high temperatures.

It is seen from Fig. 3 and Fig. 5 that the torsion modulus of both nickel and iron aluminides also decrease with increase in temperature, but the absolute drop is much less than for Young's modulus for a given range of temperature. In particular, IC-50 and IC-218 LZr show very high values of torsion modulus at high temperatures.

It may also be stated that the high temperature rigidity of both nickel and iron aluminides is far superior to that of common structural alloys like mild steel.

The Poisson's ratio of a material, being defined as the ratio of the lateral strain to the longitudinal strain in a tensile test, is a measure of the anisotropy of the material.

For a given applied stress, a high value of the elastic modulus induces a small amount of strain. In all the nickel and iron aluminides examined, the general observation is that the torsion modulus is relatively high, indicating the lateral strain is small. The Young's modulus, on the other hand, does not show abnormal trend, though the absolute values are better compared to ordinary structural materials. It may thus be surmised that the ratio of the lateral strain to the longitudinal strain (or the ratio of the longitudinal modulus to the lateral modulus) is high in all these aluminides compared to a material like mild steel, which has value of about 0.3. In the present work, the lateral modulus measured was torsion modulus, whereas for Poisson's ratio the value of shear modulus is required. Nevertheless, to understand how anisotropy is affected by temperature, plots of {(E/2G)-1} versus temperature were made, as shown in Fig. 6 and Fig. 7 for nickel aluminides and iron aluminides, respectively. In the ordinate, E is the Young's modulus and G is the torsion modulus. It is seen that in many cases the ordinate values are abnormally high, particularly at higher temperatures. Since $\epsilon_l+\epsilon_w+\epsilon_t = 0$, it follows that when $\epsilon_l=\epsilon_w=\epsilon_t$, the value of Poisson's ratio is 0.5. Thus the maximum value of the Poisson's ratio possible in a material is 0.5. The anomalous results seen in Fig. 6 and Fig. 7 indicate that the macroscopically measured Young's modulus and torsion modulus are not related to each other as in common engineering material. Furthermore, despite vast differences in the processing methods, resulting in obvious grain size variations, the trends in the ordinate values are generally similar. Schwarz has pointed out that there is significant lattice anisotropy in other intermetallics[4] and it seems to be very much necessary to investigate how this factor affects the response to stress. It is quite possible that the shear modulus is adequately low in these materials, contributing to reduction in the true lateral strain.

CONCLUSIONS

1. The Young's modulus decreases with temperature in both nickel and iron aluminides, but the extent of decrease for a given range of temperature is much less than in traditional structural materials like mild steel. Thus these materials have superior high temperature rigidity in the direction of applied stress.

2. The torsion modulus of many of these aluminides is abnormally low in relation to the Young's modulus, resulting in anomalous values of lateral strain. It is likely that submicroscopic evaluation of lateral strains will resolve this anomaly.

3. In general, nickel aluminides show superior high temperature rigidity compared to iron aluminides. All the same, the high temperature rigidity of iron aluminides is adequately high to be considered for use as inexpensive high temperature structural materials instead of the more expensive stainless steels. By the same token, nickel aluminides show promise for replacing superalloys. However, it is necessary to resolve the lateral strain anomaly in both nickel and iron aluminides before designs can be made using them.

REFERENCES

1. M.N. Srinivasan, A. Wolfenden, V.K. Sikka and S. Manjigani, "Elastic Behavior of Iron and Nickel Aluminides", Proceedings of the Seventh Annual Conference on Fossil Energy Materials", May 11-13, 1993, Oak Ridge, Tennessee, 269-275

2. C.T. Liu, P.J. Maziasz and G.M. Goodwin, "Intermetallics Down the Road", Presented at the Technology Transfer Conference on Nickel and Iron Aluminides, Oak Ridge, August 4-5, 1992.

3. V.K. Sikka, "Data Package on Fe_3Al and FEAl-based Alloys developed at ORNL", Oak Ridge National Laboratory, Oak Ridge, Tennessee, Jan.1993.

4. S.R. Srinivasan and R.B. Schwarz, "Elastic Moduli of Mo-Si_2- based Materials", <u>J. Mat. Res</u>, 7, 1992, 1611-1613.

ACKNOWLEDGEMENT

This research was sponsored by the U.S. Department of Energy, Fossil Energy AR&TD Program under Subcontract No. 19X-SM432V.

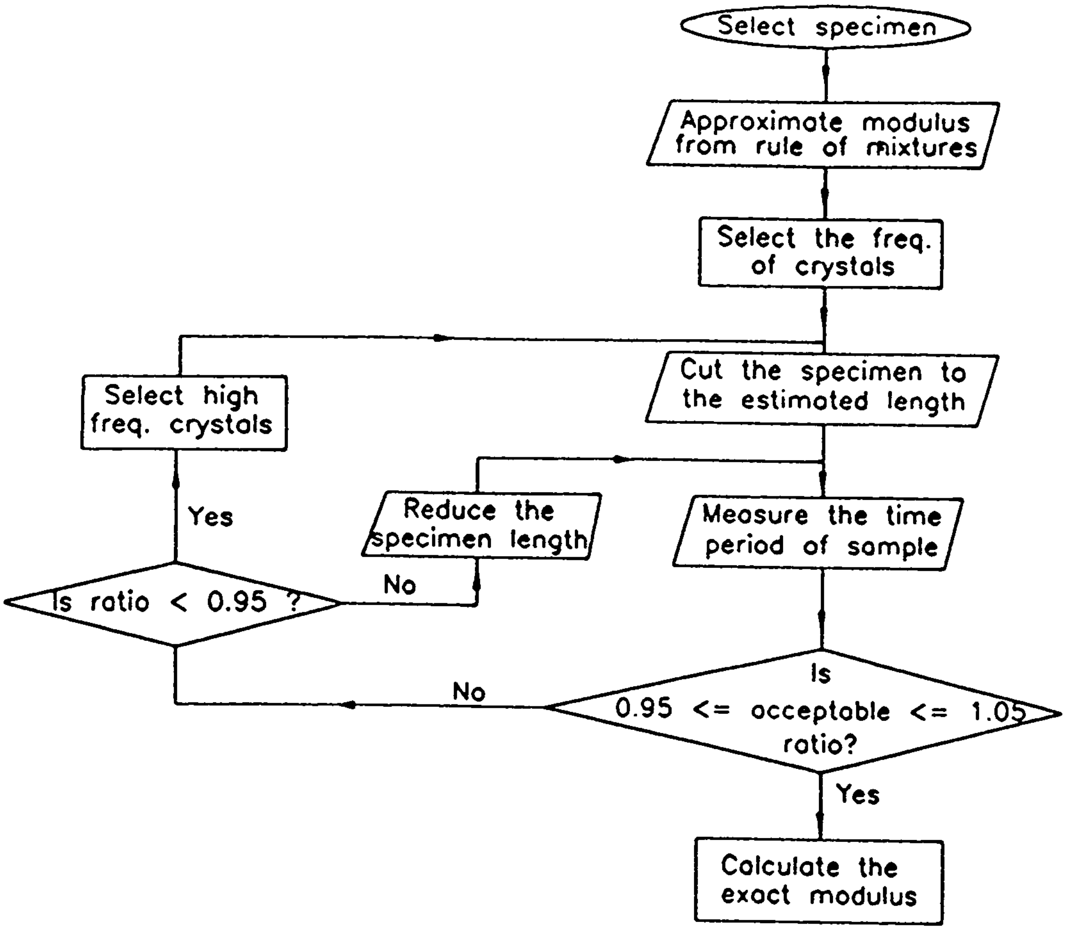

Fig. 1 Block diagram for the measurement of modulus with the PUCOT.

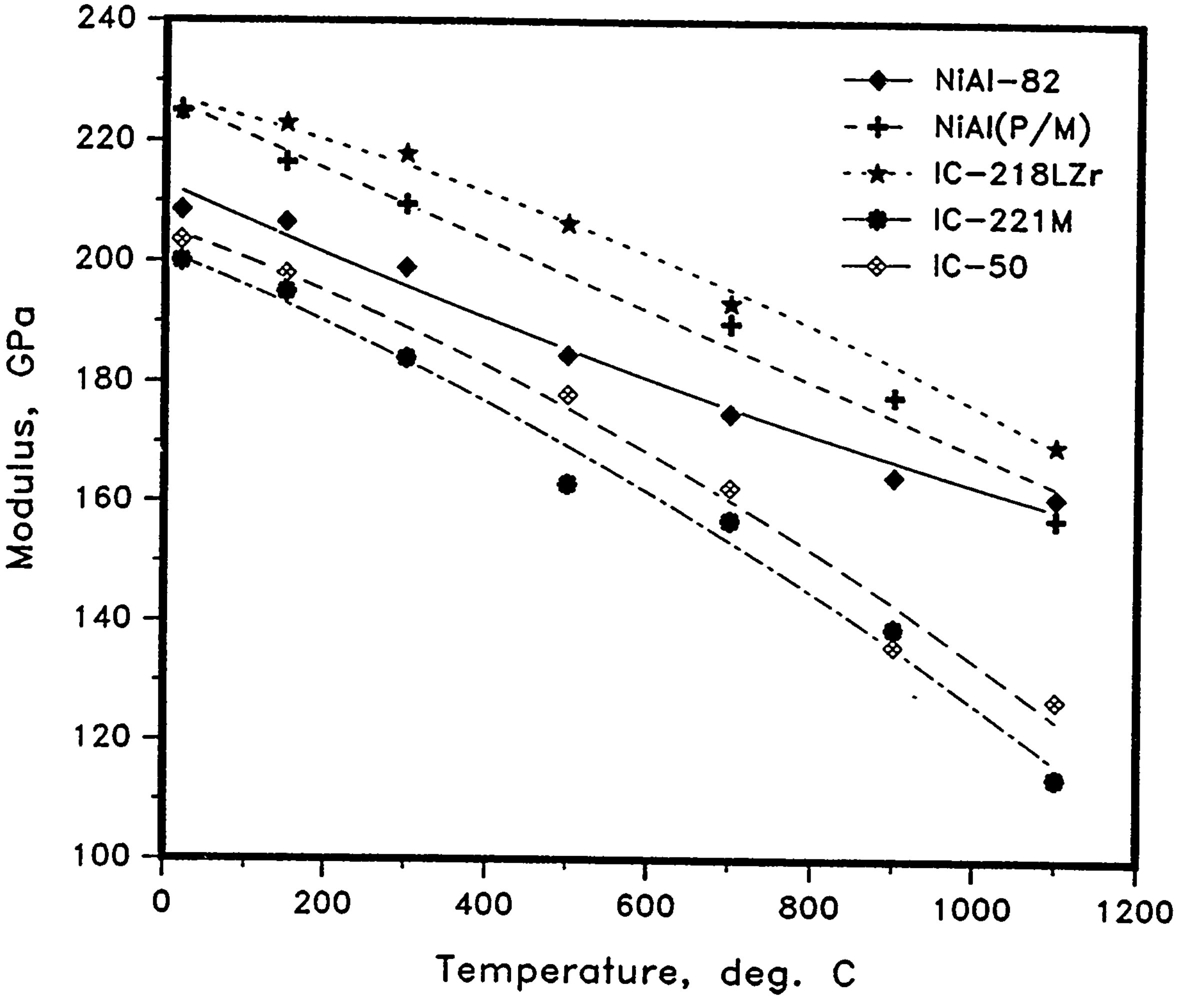

Fig. 2. Young's modulus of nickel aluminides as a function of temperature.

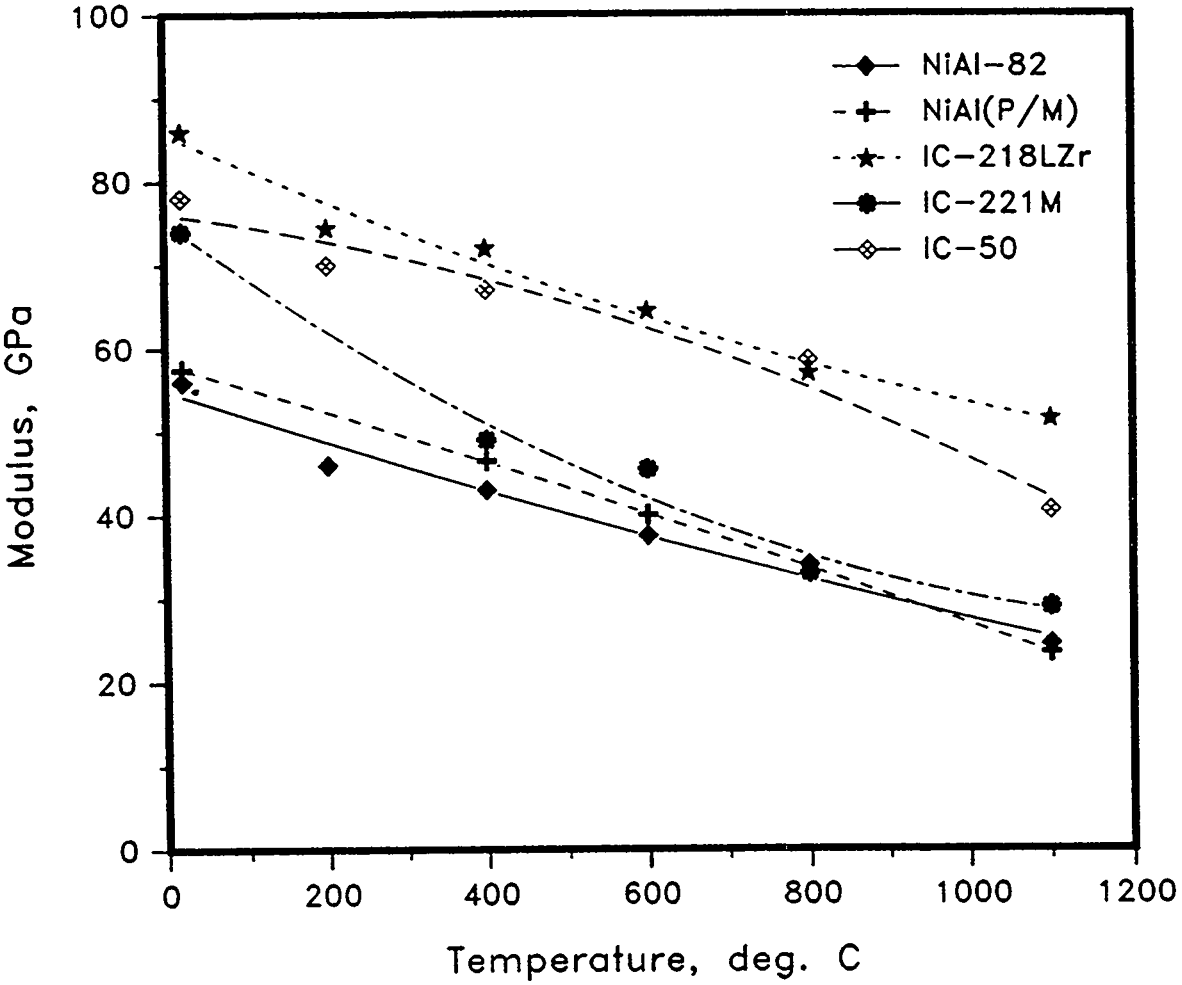

Fig. 3. Torsional modulus of nickel aluminides as a function temperature.

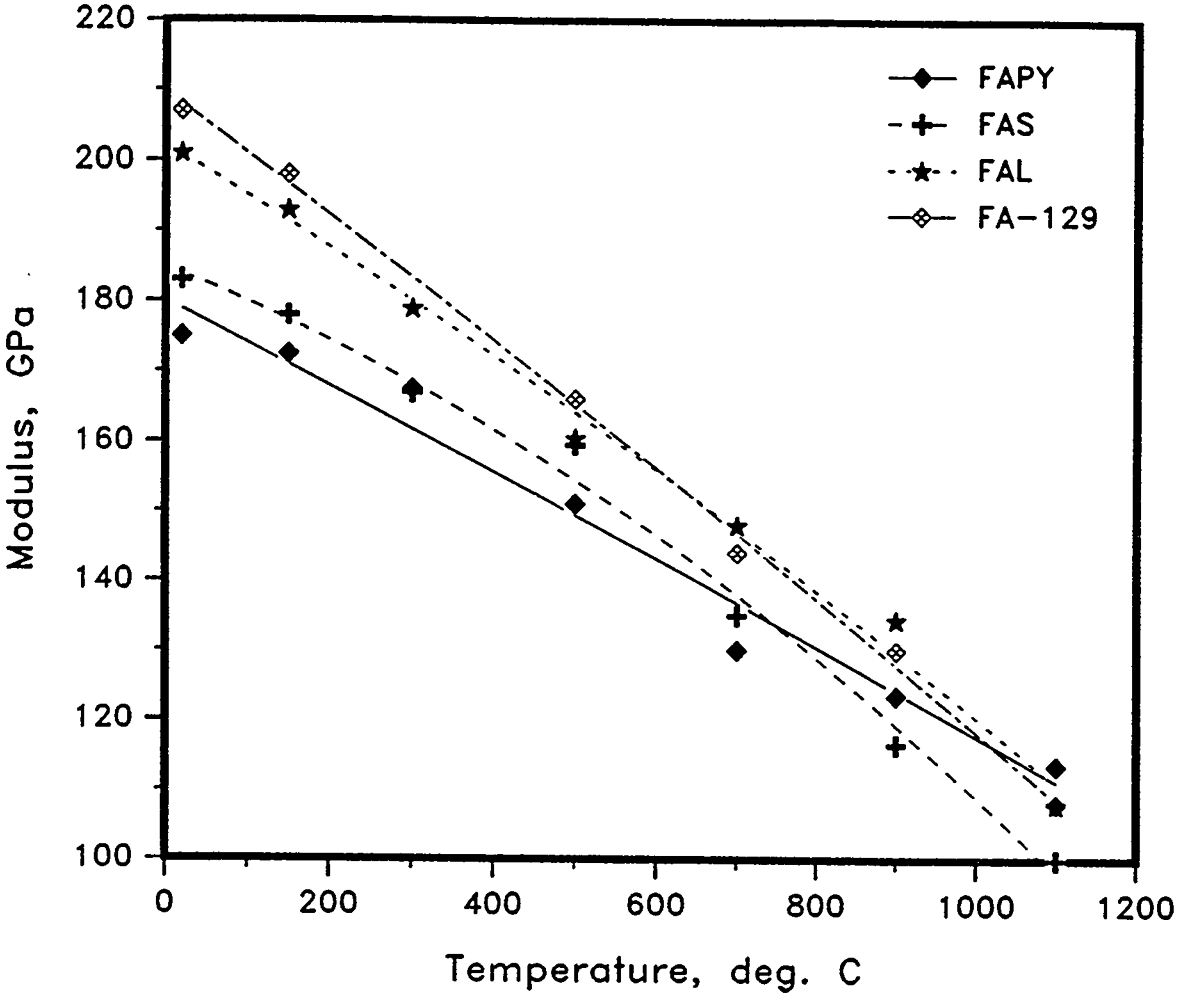

Fig. 4. Young's modulus of iron aluminides as a function temperature.

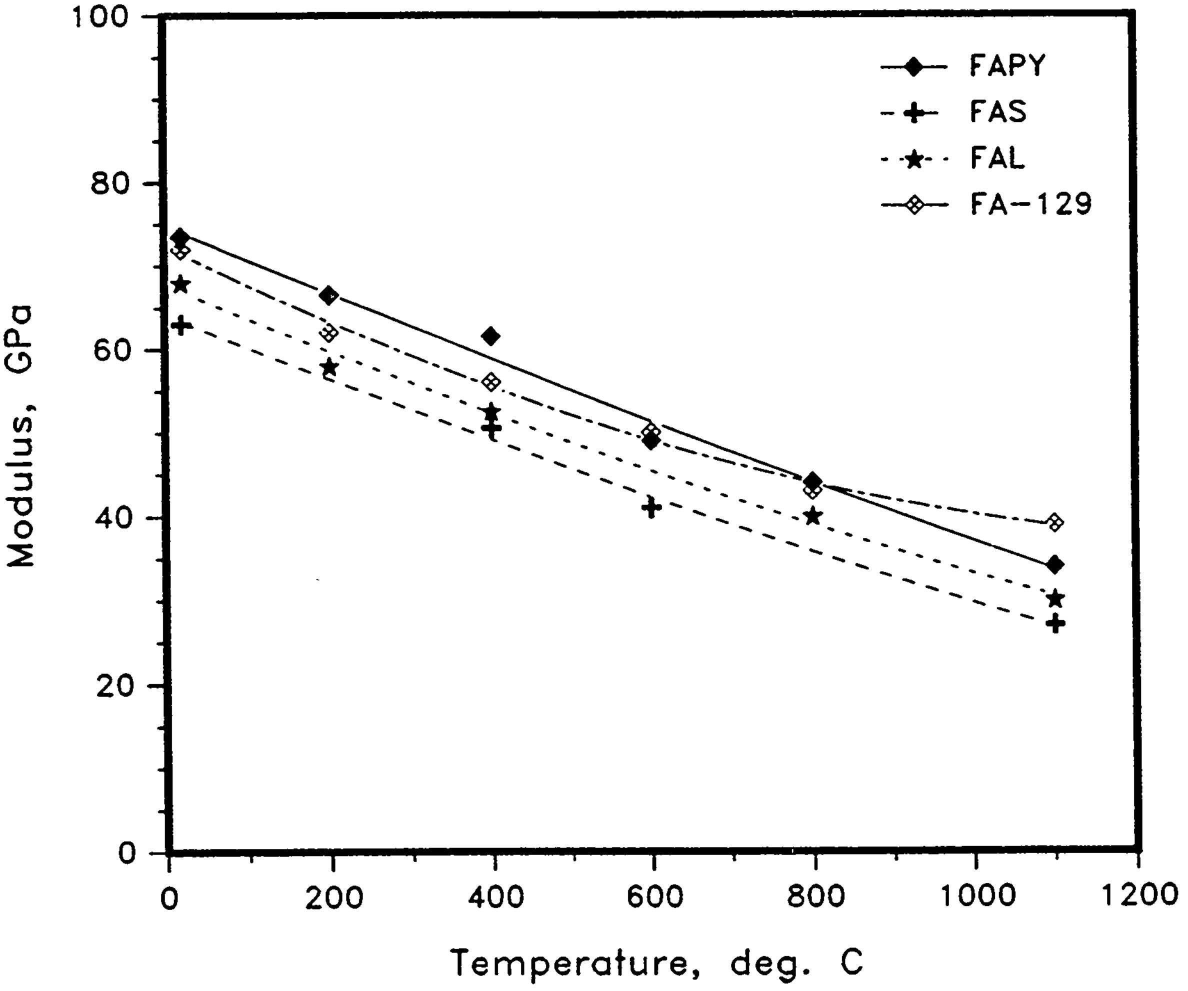

Fig. 5. Torsional modulus of iron aluminides as a function temperature.

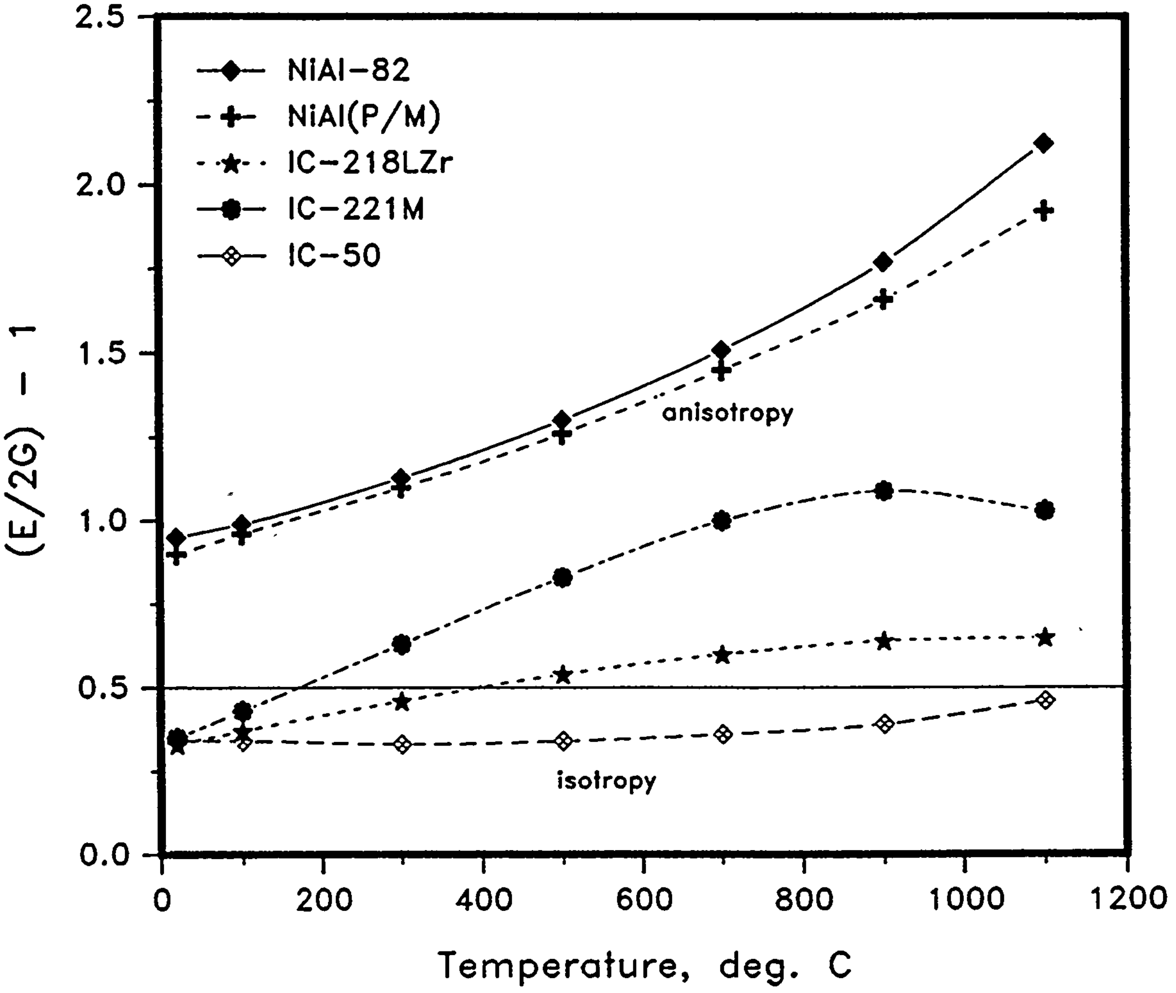

Fig. 6. (E/2G)-1 for nickel aluminides as a function temperature.

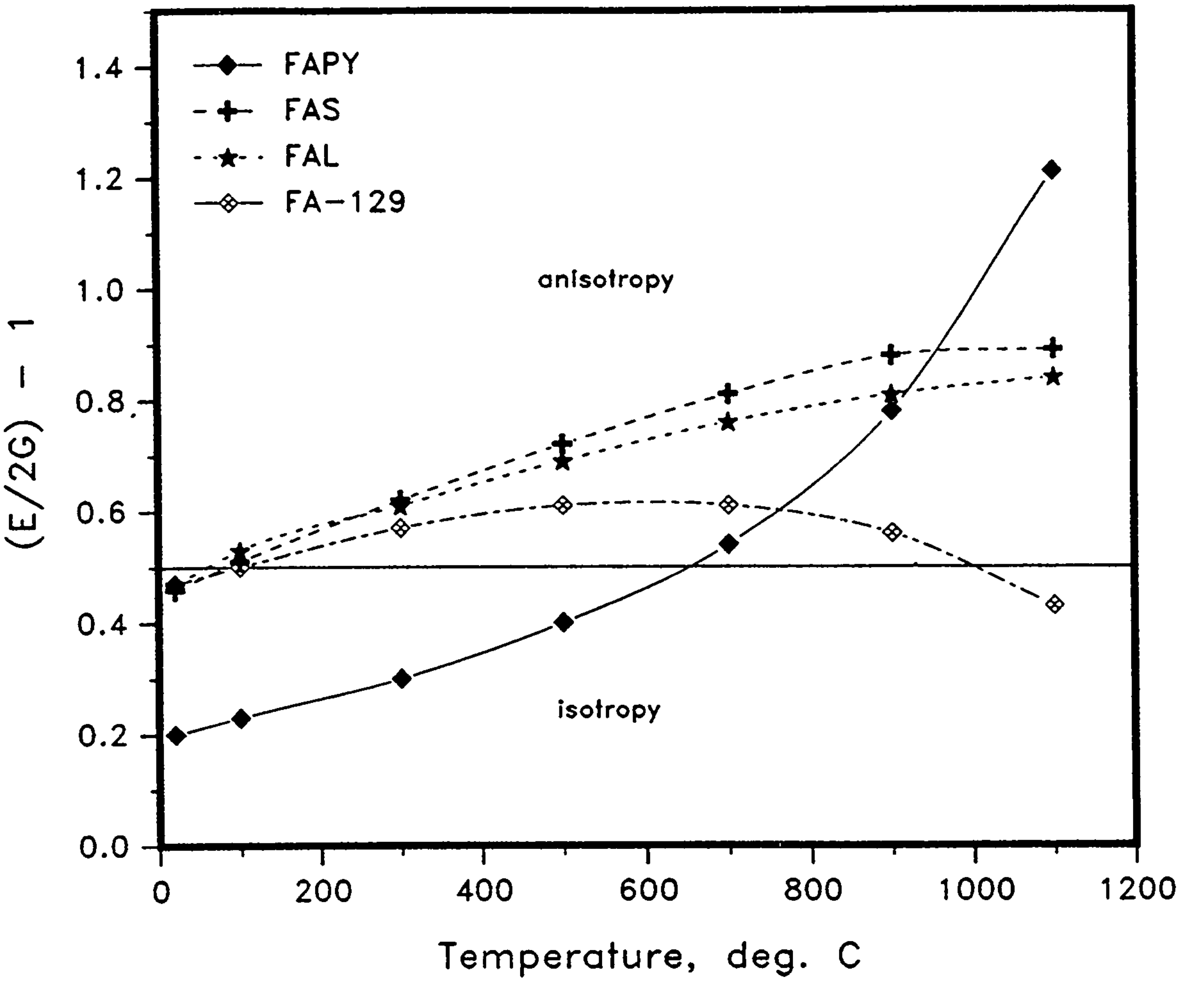

Fig. 7. (E/2G)-1 for iron aluminides as a function temperature.

SESSION III - WORKSHOP ON NEW MATERIALS DEVELOPMENT AND APPLICATIONS

SUMMARY

WORKSHOP ON NEW MATERIALS DEVELOPMENT AND APPLICATIONS

A *Workshop on New Materials Development and Applications* was held as part of the Eighth Annual Conference on Fossil Energy Materials. The workshop consisted of six separate sessions and was attended by over 150 participants. Over 60 of the participants were from industries representing producers and users of the materials being developed on the AR&TD Materials Program.

The conference and workshop were part of the overall AR&TD Materials Program strategic planning. The basis of the workshop was to provide a forum for the transfer of information from Program participants to those planning to use the technology and for participants, customers, and stakeholders to provide input on materials needs and priorities to the fossil energy technology developers and industries served by the Program.

The six sessions that constituted this workshop are listed below. The grouping of the sessions follows the work breakdown structure of the Advanced Research and Technology Development (AR&TD) Materials Program. The session titles are descriptive of the topics discussed in the workshops.

Group I — *Alloys for Advanced Fossil Energy Systems (Combustion 2000, Externally Fired Combined Cycle, Low Emission Boiler Systems, and Hot Particulate Cleanup Systems)*

Group II — *Ceramic Composites for High Temperature Heat Exchangers, Air Heaters, and Hot Gas Particulate Filters*

Group III — *Iron Aluminide Development for Coal Combustion, Coal Gasification, and Hot Particulate Cleanup*

Group IV — *Functional Materials for Fuel Cells, Gas Separations, and Catalysts*

  Group IVA — *Fuel Cell Materials Development*

  Group IVB — *Gas Separations Materials*

  Group IVC — *Catalyst Materials*

In each of the workshop sessions, rapporteurs who were experts in the field, led discussions relative to materials needs from the perspectives of producers and users of the particular materials.

A document entitled *Group Memory of the Workshop on New Materials Development and Applications* has been prepared for distribution to workshop participants. Recommendations and conclusions of the workshop are being considered and where appropriate incorporated into Program planning and implementation. Several recommendations obtained in the workshop sessions had already been incorporated into projects on the Program. Funding for all the recommended work would far exceed the current Program budget; thus, a project prioritization is being made to assure the most effective use of the funds available.

SESSION IV - INTERMETALLICS AND ADVANCED AUSTENITICS

LOW-ALUMINUM CONTENT IRON-ALUMINUM ALLOYS

V. K. Sikka

Oak Ridge National Laboratory
P.O. Box 2008
Oak Ridge, Tennessee 37831-6083

ABSTRACT

A newly developed melting method for Fe-16 at. % Al alloy (FAPY) is described. Tensile data on the air-induction-melted (AIM) and vacuum-induction-melted (VIM) heats of FAPY after identical processing are presented. Optical, scanning electron micrographs (SEM), and microprobe analysis were carried out to explain the lower room-temperature ductility and more scatter in the data for the AIM material as opposed to the VIM material.

INTRODUCTION

The FAP and FAPY are two versions of low-aluminum (16 at. %) alloys developed to alleviate the problems of environmental effects and low room-temperature ductility with Fe_3Al-based alloys.

The alloy compositions are given in Table 1. Both alloys are disordered α-alloy with the only difference being that FAPY contains yttrium. The FAP and FAPY alloy compositions were designed[1] after a systematic study[2] of 12 alloy compositions. Each element of the alloy has a specific role which is described below:

Aluminum: The aluminum content is controlled to eliminate the environmental effect that occurs upon plastic deformation through minimization or elimination of the aluminum reaction with moisture to generate hydrogen.

Chromium: The chromium addition to the alloy is made to gain resistance to aqueous corrosion.

Molybdenum: Molybdenum is added to the alloy to protect against pitting corrosion.

Zirconium and Carbon: These elements are added to form high-melting-point zirconium-carbide particles to provide grain refinement during solidification.

Table 1. Chemical composition of two low-aluminum-content iron-aluminum alloys (FAP and FAPY)

Element	Alloy (%)			
	FAP		FAPY	
	Atomic	Weight	Atomic	Weight
Al	16.12	8.46	16.12	8.46
Cr	5.44	5.50	5.44	5.50
Zr	0.11	0.20	0.11	0.20
C	0.13	0.03	0.13	0.03
Mo	1.07	2.00	1.07	2.00
Y	---	---	0.06	0.10
Fe	77.13	83.81	77.07	83.71

Yttrium: Small additions of yttrium are made to enhance high-temperature oxidation resistance.

This paper will present methods of alloy preparation and processing and tensile data.

MELTING

The melting of Fe-16 at. % Al alloys has been found to be most effective when advantage is taken of the exotherm[3] that occurs during the formation of FeAl (see Fig. 1). The proper use of the exotherm saves energy, provides better alloy chemistry control, reduces melting time, and minimizes slag formation. The specific furnace loading required to take advantage of the exotherm during the melting of FAP and FAPY alloys is shown in Fig. 2. The iron content of the alloy is divided between the top and bottom of the melt crucible. The ratio of iron to aluminum on top of the crucible is chosen to equal 50:50 at. %. The remaining iron is put at the bottom, and the alloying elements are sandwiched between the top and bottom. When the power is turned on, the entire furnace load is heated, and when the temperature reaches 660°C, the aluminum melts. The

ORNL-DWG 94-10709

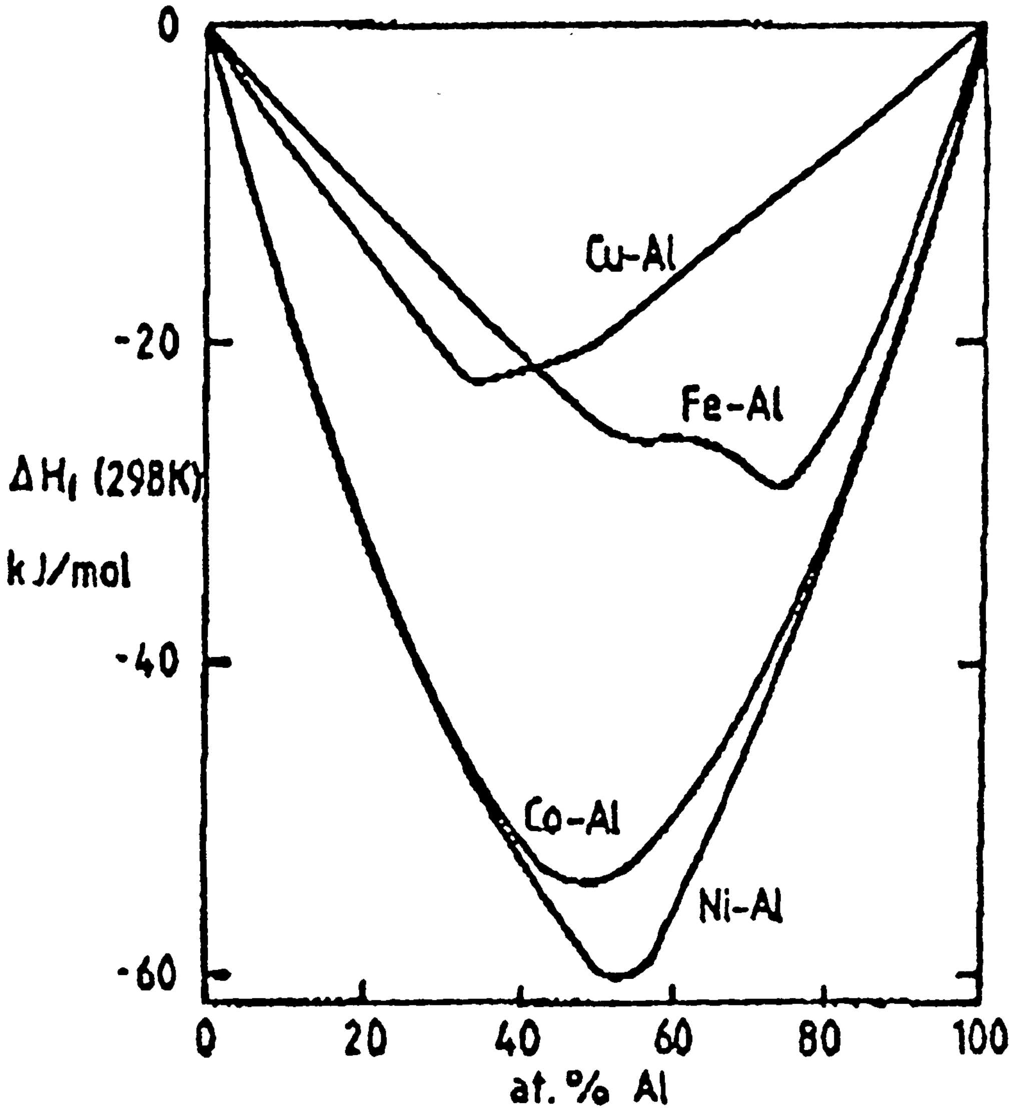

Fig. 1. Extent of exothermic reaction in aluminum binary systems with transition metals including: iron, cobalt, nickel, and copper [German (1)].

molten aluminum reacts exothermally with the iron setting next to it at the crucible top. The FeAl liquid of approximately 1500°C flows down, dissolves the alloying elements and raises the temperature somewhat for pouring. This furnace loading scheme has been successfully used commercially by Sandusky International for melting 2500-kg heats

ORNL-DWG 94-10710

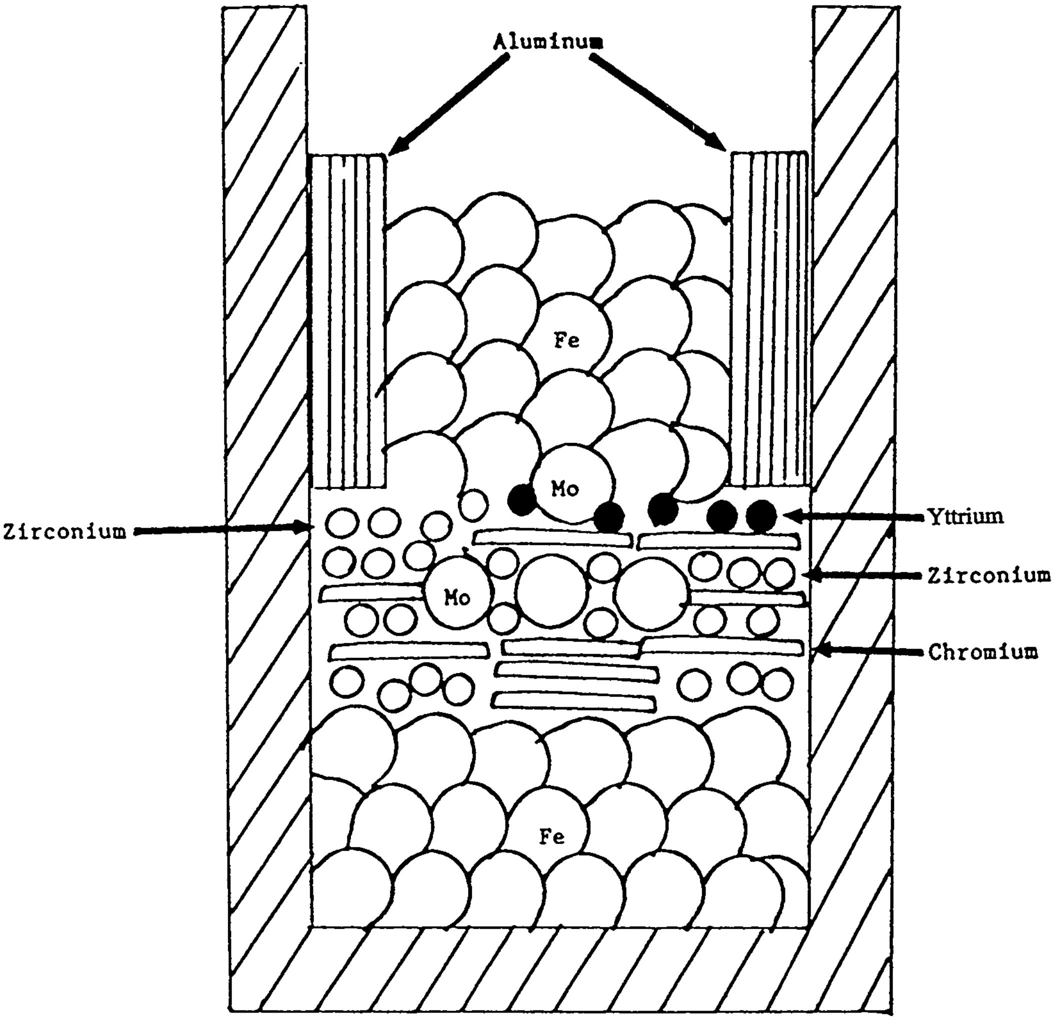

Fig. 2. Furnace-loading sequence to take advantage of heat of formation of FeAl during the melting of FAP and FAPY alloys.

of nickel-aluminide alloy containing approximately the same amount of aluminum as is present in the FAP and FAPY alloys.

The crucible selection for the melting of high-aluminum alloys is also important. Figure 3 shows the free energy of formation for Al_2O_3 and MgO as a function of temperature. Based on this figure, the aluminum in the FAP and FAPY alloys will reduce MgO of the magnesia crucible at temperatures ≥1600°C. This type of reduction of MgO will promote magnesium pickup by the alloy and erosion of the crucible. The effects of

ORNL-DWG 94-10711

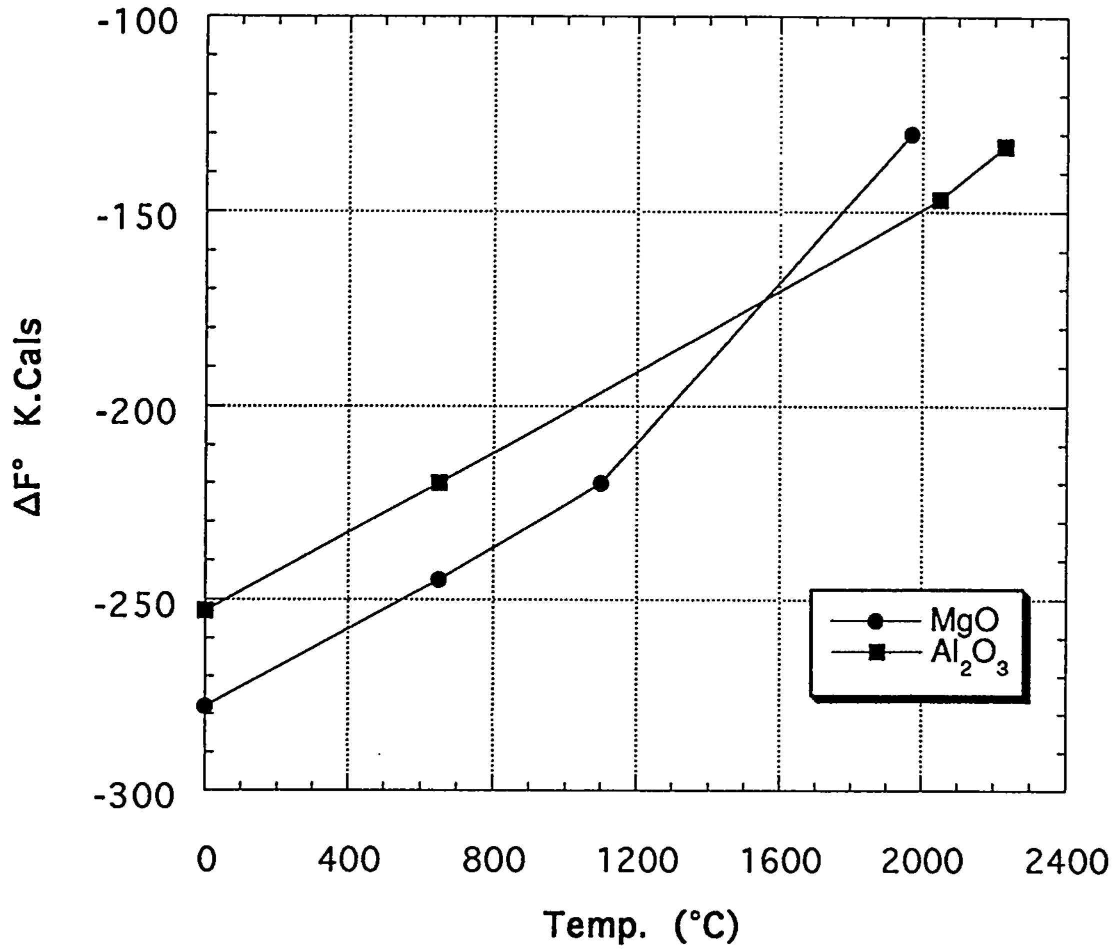

Fig. 3. Comparison of standard free energy of formation as a function of temperature to reveal the relative stability of MgO and Al_2O_3 during melting of the alloys.

magnesium on properties of FAP and FAPY alloys are not yet known. However, given the choice, the Al_2O_3 crucible should be preferred over the magnesia crucible.

The most effective method of adding yttrium to the melt is to use an Al-Y eutectic, which melts at approximately 600°C and is commercially available.

Using the process described above, one 15-lb heat each of the FAPY alloy was melted in air and in vacuum. In each case, the melt was cast into 3-in.-diam ingots. Both ingots were hot extruded at 1100°C through a die with a hole of 3/4 in. diam, which results in a reduction ratio of 16:1. Tensile test bars were machined from each of the extruded bars. Specimens were annealed at 800°C for 1 h followed by air cooling. Tensile tests were conducted in air from room temperature to 600°C.

RESULTS

Tensile data on air-induction-melted (AIM) and vacuum-induction-melted (VIM) heats are summarized in Table 2 and plotted in Fig. 4. The most significant observation is the lower ductility of the AIM material as compared to the VIM material at room temperature. The AIM material also showed more scatter in the data at room temperature as evidenced by the values of 1 and 10% for the two tests. At ≥ 50°C, the ductility values of the AIM material matched those for the VIM material. Microstructural analyse were conducted on the AIM and VIM materials to determine the cause(s) of lower room-temperature ductility of the AIM material.

Table 2. Tensile properties of hot-extruded and annealed bars[a] of FAPY alloys melted in air and vacuum. All of the tests were made in air at a strain rate of 3×10^{-3} s^{-1}.

Test temperature (°C)	Strength (MPa)		Total elongation (%)	Reduction of area (%)
	Yield	Tensile		
Air melted (Heat 15633)				
23	485	523	1.13	0.80
23	520	636	9.09	9.55
50	495	644	26.13	64.00
100	442	590	24.27	64.83
200	367	572	22.96	56.49
600	272	276	63.40	89.97
Vacuum melted (Heat 15634)				
23	514	656	21.40	52.44
100	446	612	24.00	67.41
200	361	591	24.03	64.42
600	265	269	65.55	91.31

[a] Specimens annealed for 1 h at 800°C followed by air cooling prior to testing.

ORNL-DWG 94-10712

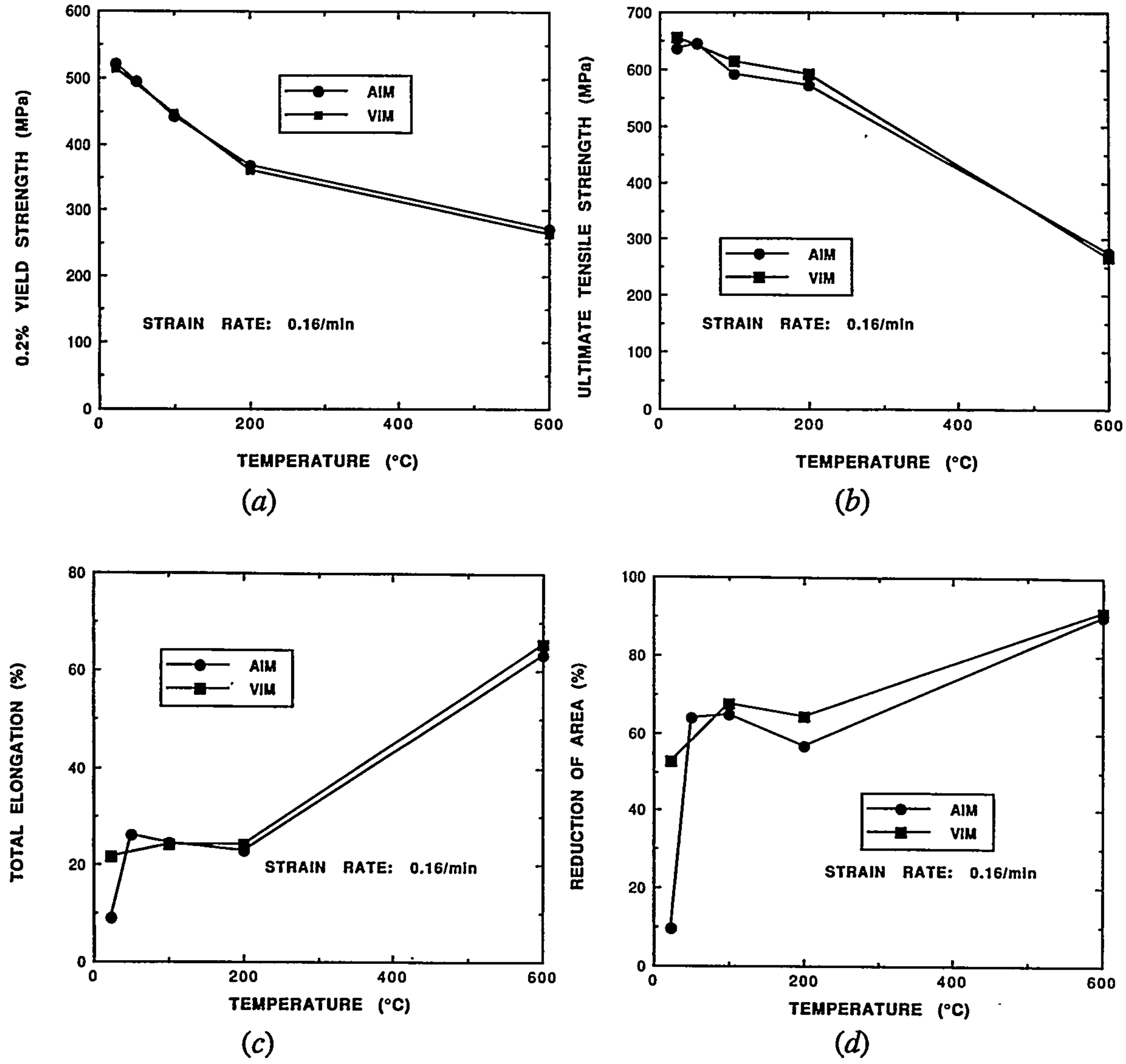

Fig. 4. Comparison of tensile properties as a function of test temperature for air-induction-melted (AIM) and vacuum-induction-melted (VIM) materials (FAPY) tested in the hot-extruded and annealed condition (1 h at 800°C followed by air cool).

The optimal microstructures of the AIM and VIM materials are shown in Fig. 5, and the grain size measurements in the longitudinal and transverse sections are listed in Table 3. This table shows that the grain size of the extruded bar from the AIM and VIM ingots is nearly the same, except near-edge section of the transverse orientation for

ORNL-PHOTO 4859-94

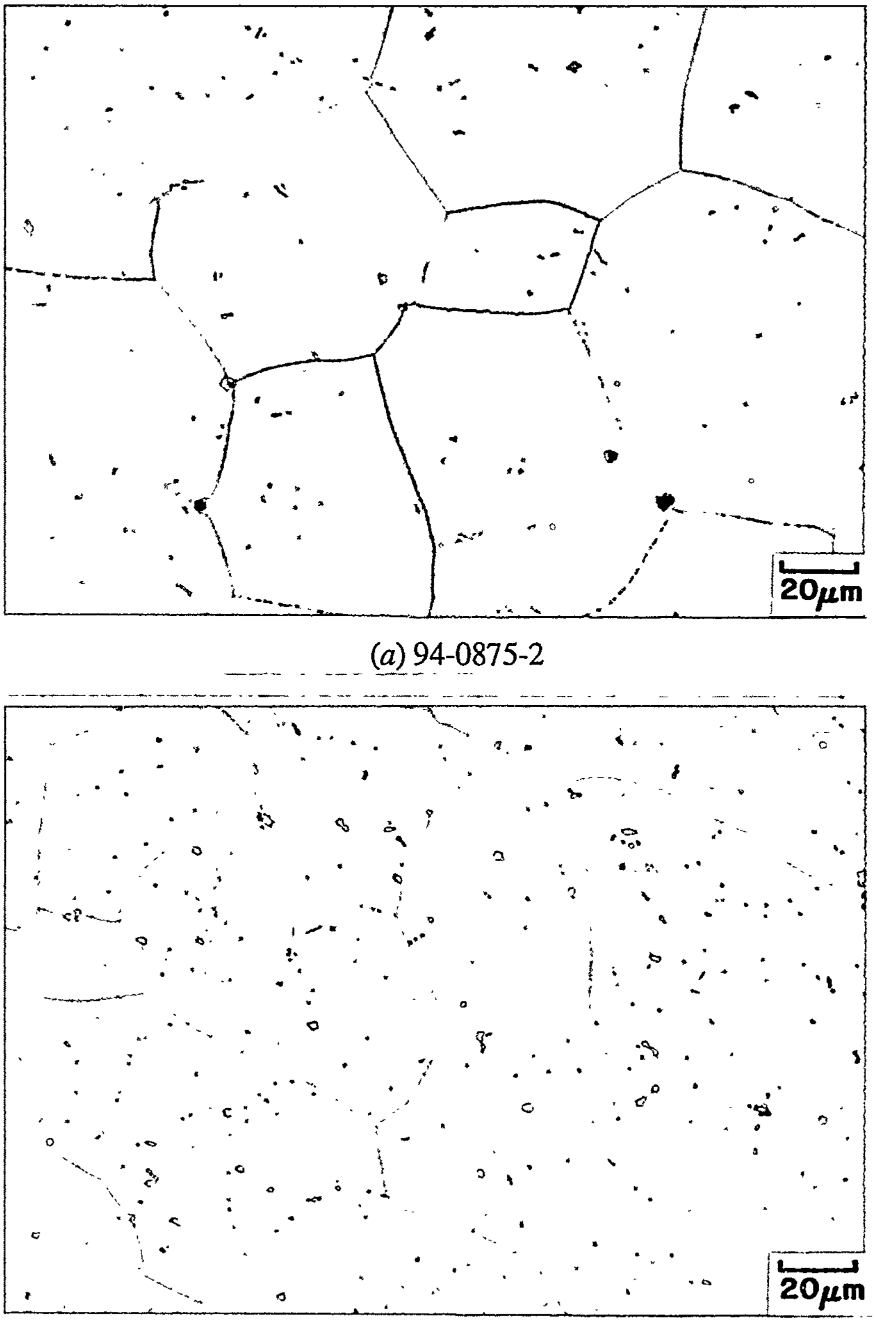

(a) 94-0875-2

(b) 94-0876-2

Fig. 5. Comparison of optical microstructures of air-induction-melted (AIM) and vacuum-induction-melted (VIM) materials (FAPY) in hot-extruded and annealed condition (1 h at 800°C followed by air cool).

Table 3. Grain size (µm)of vacuum- and air-melted and extruded bar[a] of FAPY

Melt practice	Orientation		
	Longitudinal center	Transverse	
		Center	Near edge
Vacuum	67	56	42
Air	77	57	92

[a] The extruded bar was annealed for 1 h at 800°C prior to grain-size measurement.

the AIM material showed nearly twice the grain size of the VIM material. The yttrium recovery difference between the AIM and VIM materials may be responsible for such a difference in grain size.

The low-magnification scanning electron micrographs (SEM) of the room-temperature-tested specimens of the AIM and VIM materials are shown in Fig. 6. The higher magnification SEM photographs are shown in Figs. 7 through 10. These figures show the following features: (1) the AIM specimen failed with no reduction of area as opposed to the VIM material which showed reduction of area and extensive surface deformation, (2) the AIM specimen fracture surface consisted of cleavage with some intergranular features, and (3) the VIM specimen showed cleavage with significant ductile tearing at the center of the fractured surface but only very limited ductile tearing near the specimen edge.

The sections of room-temperature-tested specimens from the AIM and VIM materials were also subjected to microprobe analysis. The backscattered electron images of the AIM and VIM specimens are shown in Figs. 11 and 12. Both specimens show the presence of precipitates. The precipitates in the VIM material are of essentially the same size and are nearly uniformly distributed, whereas precipitates in the AIM material are of elongated shape and are present as stringers. The elemental maps for iron, zirconium, and chromium for the AIM and VIM materials are shown in Figs. 13 and 14. These figures show that the precipitates seen in Figs. 11 and 12 are zirconium-rich and free of

ORNL-PHOTO 4860-94

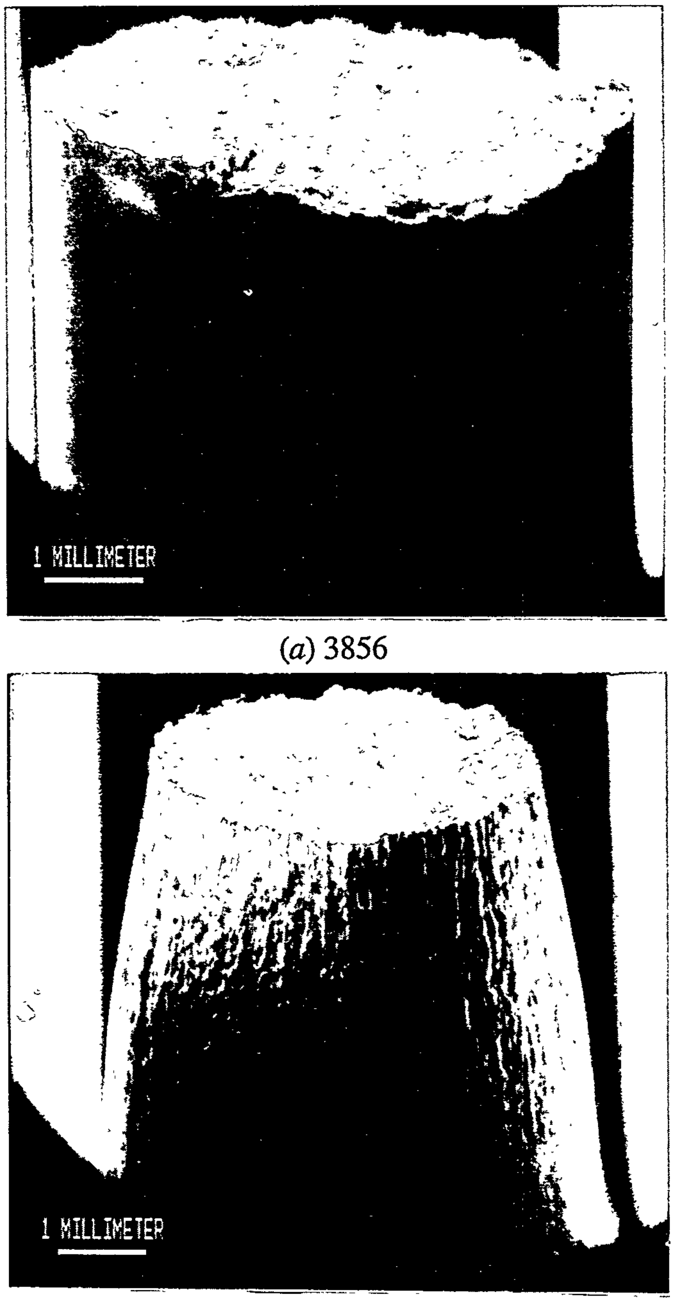

(*a*) 3856

(*b*) 3855

Fig. 6. Low-magnification scanning electron micrographs of room-temperature tensile-tested specimens from: (*a*) air-melted and (*b*) vacuum-melted and extruded bar of FAPY.

ORNL-PHOTO 4861-94

(*a*) 3848

(*b*) 3853

Fig. 7. Fracture surfaces of room-temperature tensile-tested specimens from: (*a*) air-melted and (*b*) vacuum-melted and extruded bar of FAPY.

ORNL-PHOTO 4862-94

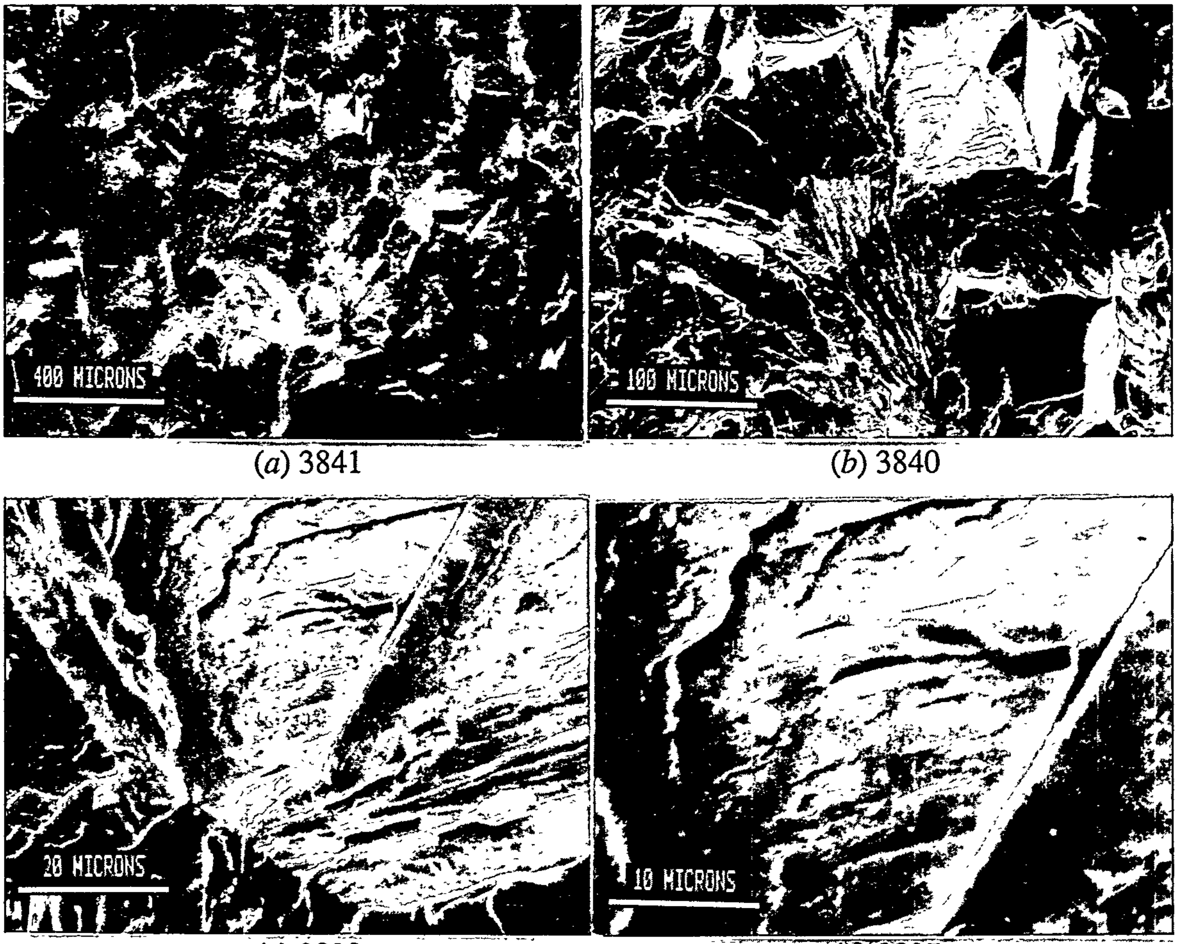

(*a*) 3841 (*b*) 3840

(*c*) 3838 (*d*) 3837

Fig. 8. Fracture surface details of room-temperature tensile-tested specimens from air-melted and extruded bar of FAPY: (*a*) 50×, (*b*) 200×, (*c*) 1000×, and (*d*) 2000×.

iron. The AIM material showed segregation of chromium at the grain boundaries. The stringer type of zirconium-rich particles and chromium-rich particles at the grain boundaries are considered responsible for the mixed mode cleavage, and grain boundary dominated fracture in the AIM material. Since the matrix and grain boundary strength can both be reduced in the AIM material by the precipitates (see Table 4), the lower ductility values are not surprising. In fact, if these precipitates are responsible for low ductility, their variation along the extrusion length could be responsible for the observed scatter in the room-temperature data for the AIM material.

ORNL-PHOTO 4863-94

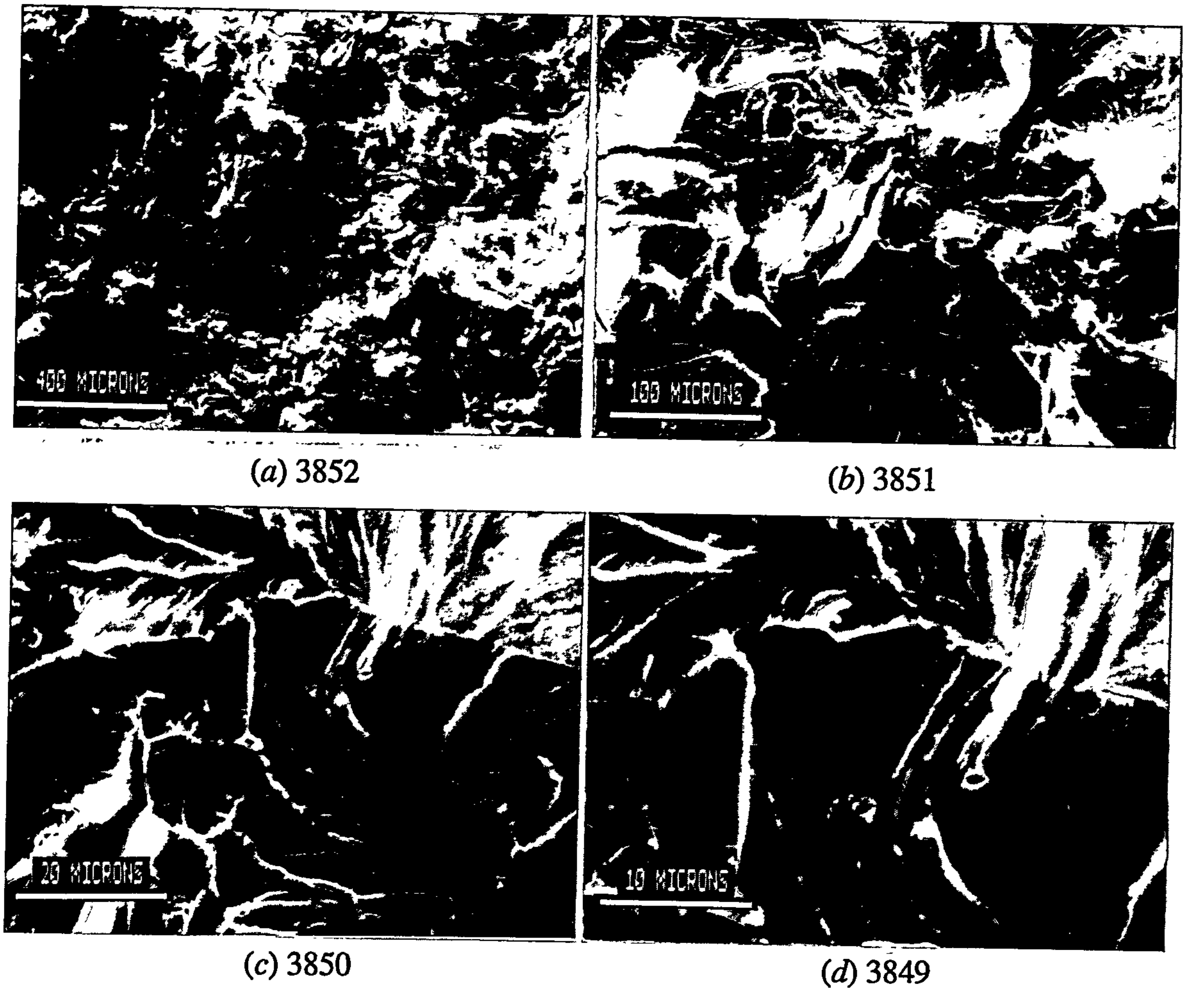

(*a*) 3852 (*b*) 3851

(*c*) 3850 (*d*) 3849

Fig. 9. Fracture surface details of room-temperature tensile-tested specimens from vacuum-melted and extruded bar of FAPY: (*a*) 50×, (*b*) 200×, (*c*) 1000×, and (*d*) 2000×.

However, the ductile-to-brittle transition temperature for the body-centered cubic material is known to be very sensitive to the inclusion content, size, and distribution. Data presented in this paper show that melting in air and using processing for the AIM material similar to the VIM material, is not adequate to break down the precipitates in the FAPY alloy for it to be ductile at room temperature. Additional processing of the extruded bar consisting of forging 50% at 1100°C followed by final rolling at 650°C to 0.03-in.-thick

ORNL-PHOTO 4864-94

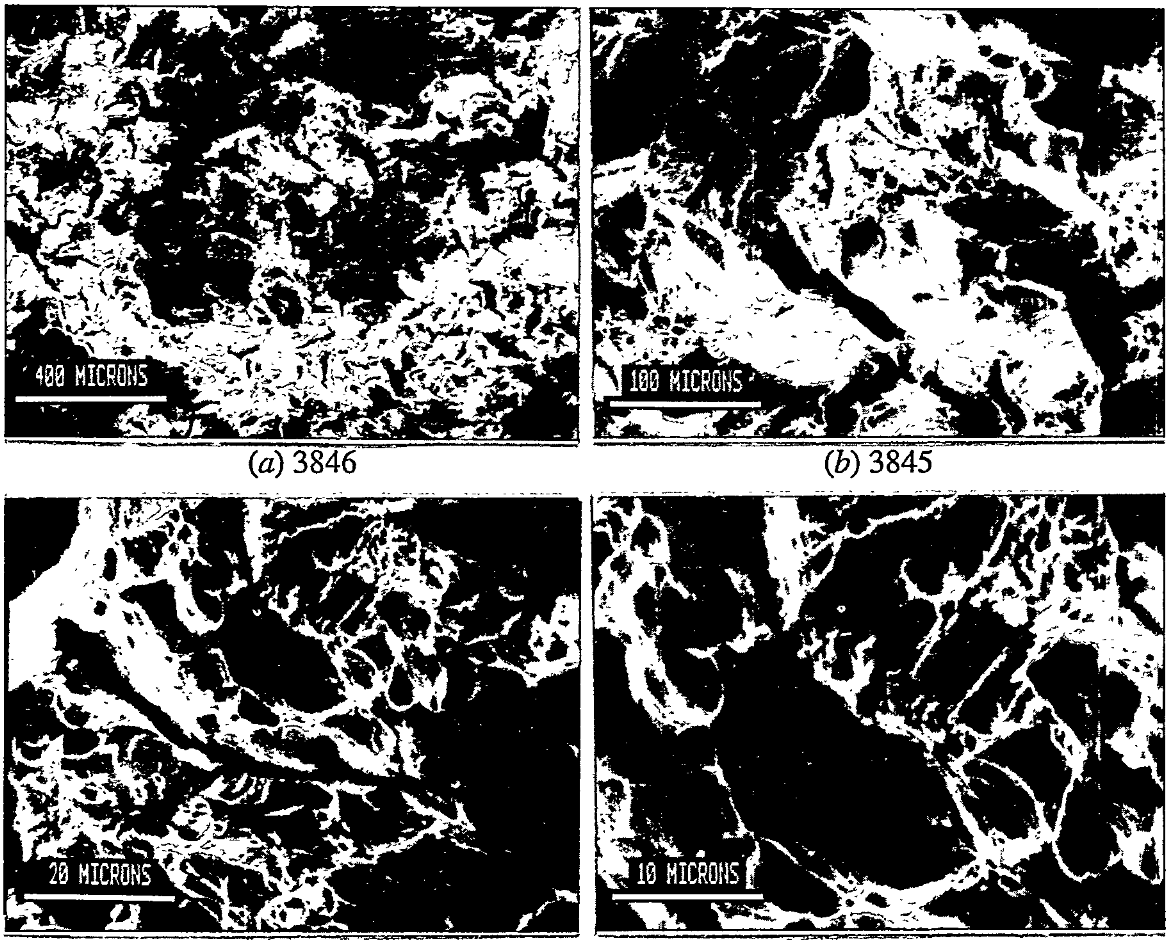

(*a*) 3846 (*b*) 3845

(*c*) 3844 (*d*) 3843

Fig. 10. Fracture surface details of room-temperature tensile-tested specimens from vacuum-melted and extruded bar of FAPY near the specimen center: (*a*) 50×, (*b*) 200×, (*c*) 1000×, and (*d*) 2000×.

sheet resulted in a significant increase in ductility of the AIM material (see Table 4). The VIM material when subjected to the same processing steps as the AIM material showed no change.

ORNL-PHOTO 4865-94

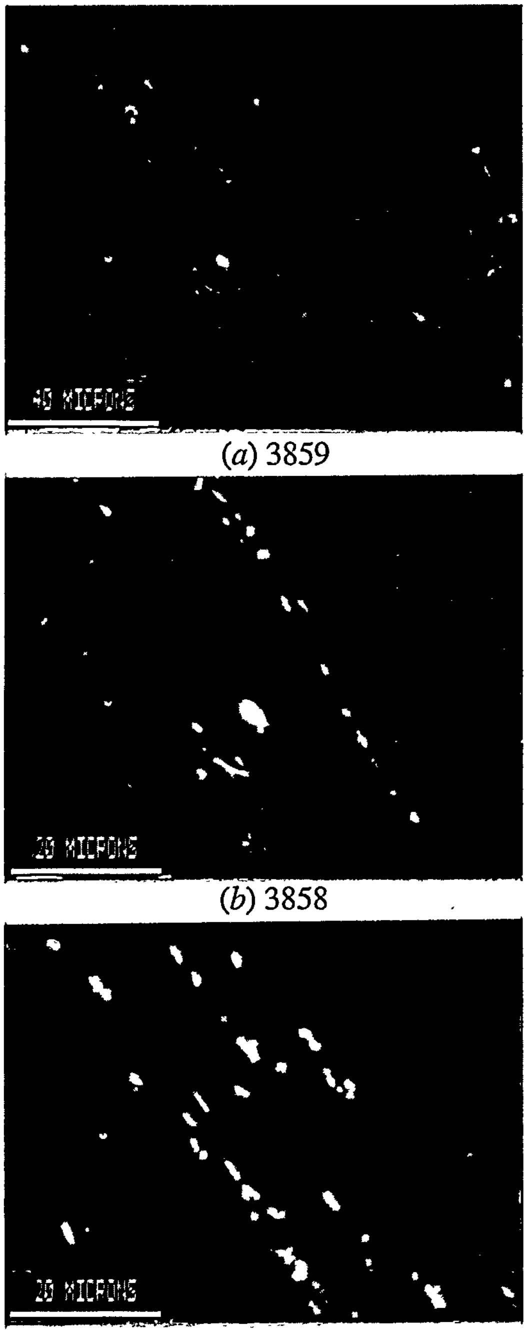

(*a*) 3859

(*b*) 3858

(*c*) 3873

Fig. 11. Backscattered electron image photomicrographs for air-induction-melted (AIM) material (FAPY) in hot-extruded and annealed condition (800°C for 1 h followed by air cool).

ORNL-PHOTO 4866-94

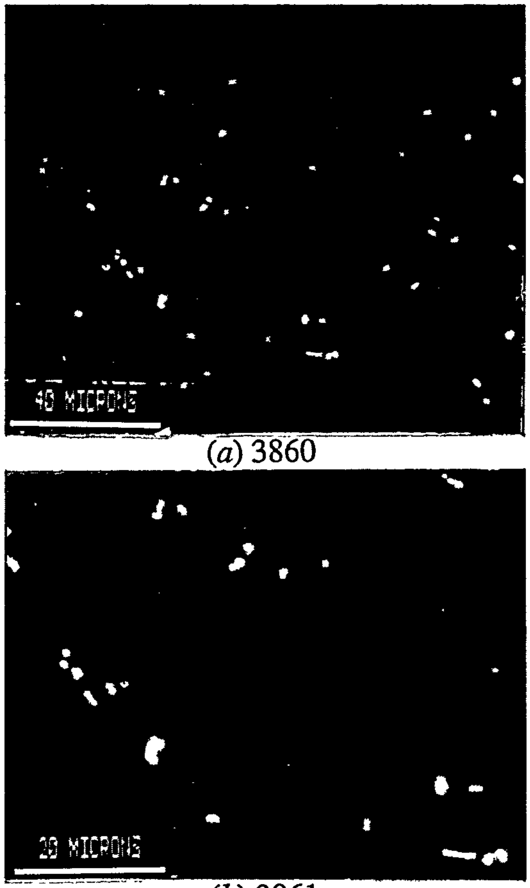

(*a*) 3860

(*b*) 3861

Fig. 12. Backscattered electron image photomicrographs for vacuum-induction-melted (VIM) material (FAPY) in hot-extruded and annealed condition (800°C for 1 h followed by air cool).

ORNL-PHOTO 4867-94

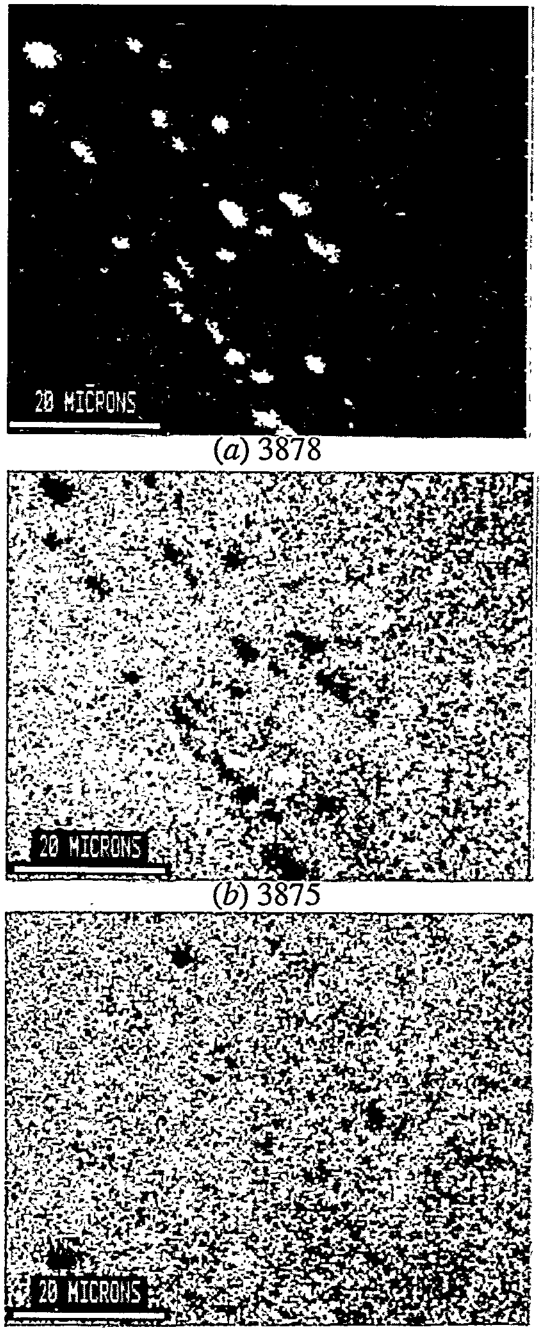

Fig. 13. (*a*) Zirconium, (*b*) iron, and (*c*) chromium maps for air-induction-melted (AIM) material (FAPY) in hot-extruded and annealed condition (800°C for 1 h for followed by air cool).

ORNL-PHOTO 4868-94

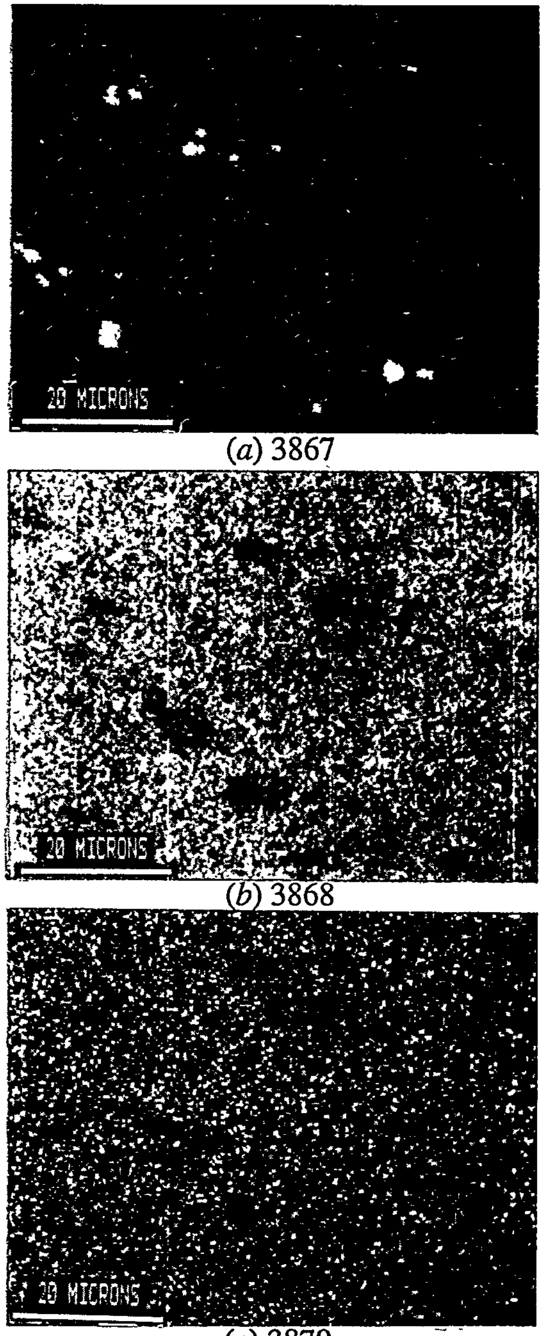

Fig. 14. (*a*) Zirconium, (*p*) iron, and (*c*) chromium maps for vacuum-induction-melted (VIM) material (FAPY) in hot-extruded and annealed condition (800°C for 1 h followed by air cool).

Table 4. Tensile properties of extruded bars of air-induction-melted and vacuum-induction-melted materials after additional processing consisting of forging 50% at 1100°C followed by rolling at 650°C to 0.03-in.-thick sheet.[a]

Test temperature (°C)	Strength (MPa)		Total elongation (%)	Reduction of area (%)
	Yield	Tensile		
	Air melted (Heat 15633)			
23	563	653	25.74	35.01
23	521	656	27.80	39.40
	Vacuum melted (Heat 15634)			
23	559	665	21.68	23.49
23	562	662	21.00	29.04

[a] Specimens annealed for 1 h at 800°C followed by air cooling prior to testing.

SUMMARY AND CONCLUSIONS

A newly developed melting method for Fe-16 at. % Al alloy (FAPY) was described. Tensile data on the AIM and VIM heats of FAPY after identical processing were presented. Optical, SEM, and microprobe analysis were carried out to explain the lower room-temperature ductility and more scatter in the data for the AIM material as opposed to the VIM material. Below are significant conclusions from the work.

1. The AIM material showed zirconium-rich particles as stringers as opposed to essentially equal size and nearly uniformly distributed particles in the VIM material.
2. The AIM material showed chromium-rich precipitates at the grain boundaries.
3. The presence of zirconium-rich particles as stringers and chromium-rich particles at the grain boundaries is considered responsible for lower room-temperature ductility of the AIM material.
4. The inhomogeneous distribution of the zirconium- and chromium-rich precipitates in the AIM material may be responsible for scatter in its data.

5. Additional hot forging followed by warm working to break down the zirconium- and chromium-rich particles in the AIM material improved its room-temperature ductility to the same values as observed for the VIM material.

ACKNOWLEDGMENTS

The author thanks K. S. Blakely and E. C. Hatfield for processing, R. H. Baldwin for tensile testing, C. R. Howell for analyzing data, R. W. Swindeman and E. K. Ohriner for reviewing the manuscript, K. Spence for editing, and M. L. Atchley for preparing the manuscript.

REFERENCES

1. V. K. Sikka and C. G. McKamey, "Iron-Aluminum Alloys Having High Room Temperature and Method for Making Same," U.S. Patent No. 5,238,645 (Aug. 24, 1993).

2. V. K. Sikka, S. Viswanathan, and S. Vyas, "Acceptable Aluminum Additions for Minimal Environmental Effect in Iron-Aluminum Alloys," pp. 971-76 in *High Temperature Ordered Intermetallic Alloys V*, ed. L. A. Johnson, D. P. Pope, and J. O. Stiegler, Materials Research Society (Mater. Res. Soc. Proc. **288**), Pittsburgh, Pa., 1993.

3. R. M. German, pp. 205-31 in *Thermal Analysis in Metallurgy*, ed. R. D. Shull and A. Joshi, The Minerals, Metals and Materials Society, Warrendale, Pa., 1992.

THE INFLUENCE OF PROCESSING ON MICROSTRUCTURE AND PROPERTIES OF IRON ALUMINIDES

R. N. Wright and J. K. Wright

Idaho National Engineering Laboratory, EG&G Idaho, Inc.
Idaho Falls, ID 83415-2218

ABSTRACT

The influence of hot working and subsequent annealing on the microstructure and mechanical properties of iron aluminide alloy FA-129 have been examined using x-ray diffraction and transmission electron microscopy. It has been shown that the presence of defect substructure, even in the form of well developed low angle dislocation boundaries, retards the formation of DO_3 order on cooling from the B2 regime. The influence of processing on properties of iron alloys containing approximately 16 at.% Al has also been examined in detail and the relationship to the microstructure will be discussed.

Reaction synthesis methods have been developed for joining alloy FA-129 and for producing porous iron aluminides for filter applications. Elemental powders or foils have been used to reactively join FA-129 with a Fe_3Al joint layer. The mechanism of bonding appears to be somewhat complex, however, it has been demonstrated that the joints formed from elemental powders are superior to those formed by reaction of elemental foils. The fine grained structure of joints formed from elemental powders results in joints that are stronger than the base material and tensile failure occurs in the base material away from the joint region. Prototype porous Fe_3Al filters formed by reaction synthesis have been produced and tested, showing flow characteristics suitable for filtering hot gas streams.

INTRODUCTION

Alloys based on the intermetallic compound Fe_3Al have reasonable elevated temperature mechanical properties, good resistance to oxidation and sulfidation, and are resistant to wear and erosion. Improved understanding of the effects of alloying and processing on controlling the strength and ductility of these alloys has lead to interest in applying these materials at elevated temperature in aggressive environments.

Before widespread application of these materials is possible, several further developments are necessary. These include improved elevated temperature mechanical properties and methods of joining Fe_3Al into more complex assemblies or to other materials. In addition, there appears to be interest in fabricating porous iron aluminides for application as filters, to take advantage of the superior sulfidation resistance of these materials.

The purpose of this project is to examine the effect of synthesis and processing on the structure and properties of iron aluminides. The results of a study of the influence of substructure on the B2 to DO_3 transition of alloy FA-129 during cooling are presented. Reactive synthesis is also demonstrated as a means of joining alloy FA-129 and for fabrication of controlled porosity binary Fe_3Al. Two different heats of a low aluminum alloy (designated FAPY) have also been examined to determine the origin of a large difference in mechanical properties between the heats.

REACTIVE SYNTHESIS

Mechanical property tests were conducted on joints between sections of extruded FA-129 using reactive synthesis from elemental powders and foils. The powders were 3 μm diameter carbonyl iron and 40 μm diameter gas atomized aluminum mixed dry with relative volume fractions designed to yield Fe-28%Al. For joints from foils, an iron foil 0.1 mm in thickness was placed between aluminum foils that were 0.02 mm in thickness, resulting in a ratio of Fe-21.2%Al by volume. Joints were made under flowing argon in a hot press under 20 MPa pressure with a hold time of 30 minutes at temperature.

Optical micrographs of the joints made from powder and foil are shown in Figure 1 a and b. It is evident from the micrographs that the grain size in the joint made from powder is considerably finer than that in the joint made from foils. The grain size of the extruded material is significantly more coarse than either of the joint layers. Mechanical properties of the joints are given in Table 1, where the values represent averages of three tests for each type of joint. Two of the tensile bars containing joint layers from powder broke well away from the joint in the base material, thus the tensile values for these specimens reflect the base material properties. One of the joints made from powder and all three of the joints from foil failed at the interface between the joint layer and the base material.

The interface between the joint layer and base material for joints synthesized from both powders and foils was examined using transmission electron microscopy. Samples prepared by conventional electropolishing resulted in preferential thinning in the base material and in the joint material for joints made from powder and foils, respectively. In either case it was necessary to further thin the specimen using ion milling to examine the interface. A brightfield micrograph of the interface in a foil joint is shown in Figure 2. For

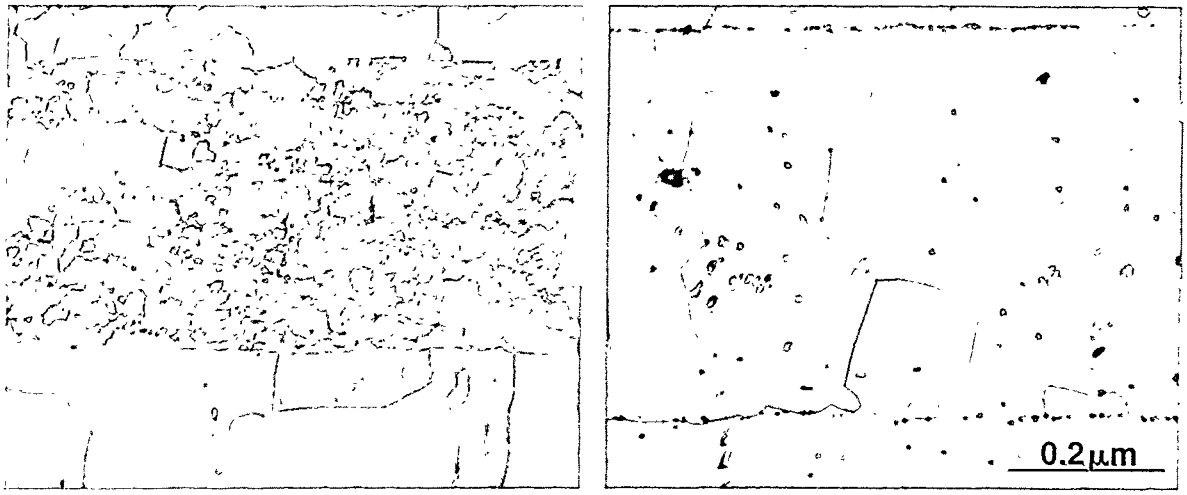

(a) (b)

Figure 1. Optical micrographs of joints synthesized from (a) elemental powders, and (b) elemental foils.

both joining methods the interface appeared well bonded with no large scale discontinuities, with contrast similar to a conventional grain boundary. There was typically a row of oxides present from the original surface, however, in most cases the joint interface had migrated away from the oxides. This observation is in accord with optical microscopy, which typically showed that the interface has moved away from the original surfaces.

The difference in mechanical behavior of the joints synthesized from powder and foils is probably related in part to the differences in grain size. It has been shown previously in bulk Fe_3Al reaction synthesized from powder that the fracture stress was above 700 MPa, where the high strength was attributed to the fine grain size.[1] In tensile tests of joints from powder the deformation and eventual fracture is well away from the joint, reflecting the relatively low strength of large grained extruded material. Since the extruded material began to yield well below the strength of the joint layer, the fracture

Table 1. Tensile properties of specimens with hot pressed joints

Reaction Material	**Y.S. (MPa)**	**U.T.S. (MPa)**	**Total Elong. (%)**
Powder	223 ± 2	433 ± 46	4.32 ± 0.75
Foil	225 ± 10	236 ± 13	0.79 ± 0.12

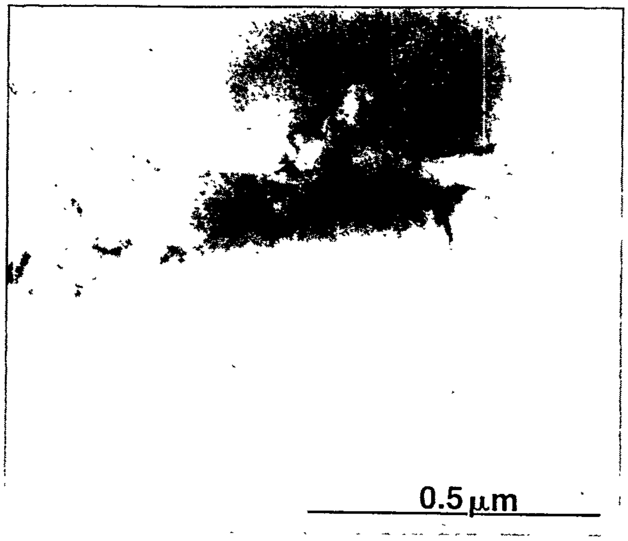

Figure 2. Bright field electron micrograph of the interface in a joint synthesized from elemental foils.

strength of the interface or true bond strength was not reached. In contrast, the bond strength of the joints formed from foils was apparently reached soon after yielding of the matrix occurred. The large grained material formed from reaction of foils is also expected to have low fracture strength, and the fracture path was observed to traverse the joint material.

To further examine the mechanism of bonding, a series of joining experiments was performed in a load control hydraulic testing frame mounted with an induction coil under flowing argon. This method allowed a more rapid heating cycle and shorter hold times. Samples consisting of tensile bars that had been cut in half were joined, and subsequently tested in tension after cooling to room temperature to determine strength and fracture behavior. The heating cycles and tensile results are summarized in Table 2.

The differences in bonding between joints formed from elemental powders compared to those formed from foils, and the observations shown in Table 2 of enhanced bond strength with increased time at temperature using either method, suggest that there are two mechanisms that contribute to bonding using reaction synthesis. The first contribution seems to arise from the synthesis reaction and the second appears to be related to bonding in the solid state. It should be noted that experiments conducted to attempt joining with no inter layer or with only aluminum foil, to test whether diffusion bonding or reduction of the

Table 2. Tensile properties of joints formed from powders or foils

Reaction Material	Temperature (°C)	Time (min)	Fracture Strength (MPa)
Powder	1100	30	433*
	1100	5	350
	900	30	270
	900	5	100
Foil	1100	30	236*
	1100	5	100
	900	5	0

* Average of three specimens.

surface oxides by liquid aluminum alone resulted in bonding, respectively, yielded no bonding.

Preliminary work has demonstrated that 25 mm diameter porous binary Fe_3Al disks can be fabricated using reactive synthesis of die pressed elemental powders.[2] The density of the disks varied from 68 to 86% of theoretical and is primarily controlled by the initial aluminum powder diameter. Gas flow testing on the disks indicates that the porosity is sufficiently interconnected to give acceptable pressure drops across the prototype filter elements. Experiments have shown that the disks commonly warped during processing, presumably either due to non-uniform density resulting from cold pressing the powders or from initiation of the synthesis reaction from a single point. This problem has been eliminated by reacting the disks under slight pressure (<1MPa), however, the surface finish of the disks remains a concern.

SUBSTRUCTURE EFFECTS ON B2 TO DO_3 TRANSITION

It has been suggested previously that the presence of defect substructures has an effect on the B2 to DO_3 transformation on cooling.[2,3] A series of more well controlled experiments was conducted to examine this effect in more detail. Warm rolled FA-129 was annealed at 700 and 900°C to establish substructures consisting of low angle dislocation boundaries and recrystallized material, respectively. These samples were subsequently heat treated at 600°C along with as-rolled material containing dislocation tangles and cell structures to establish the same B2 order conditions and either air cooled or water quenched. Electron diffraction patterns from the air cooled specimens are shown in Figure 3. It is clear from the electron diffraction patterns that the presence of defects, even in well

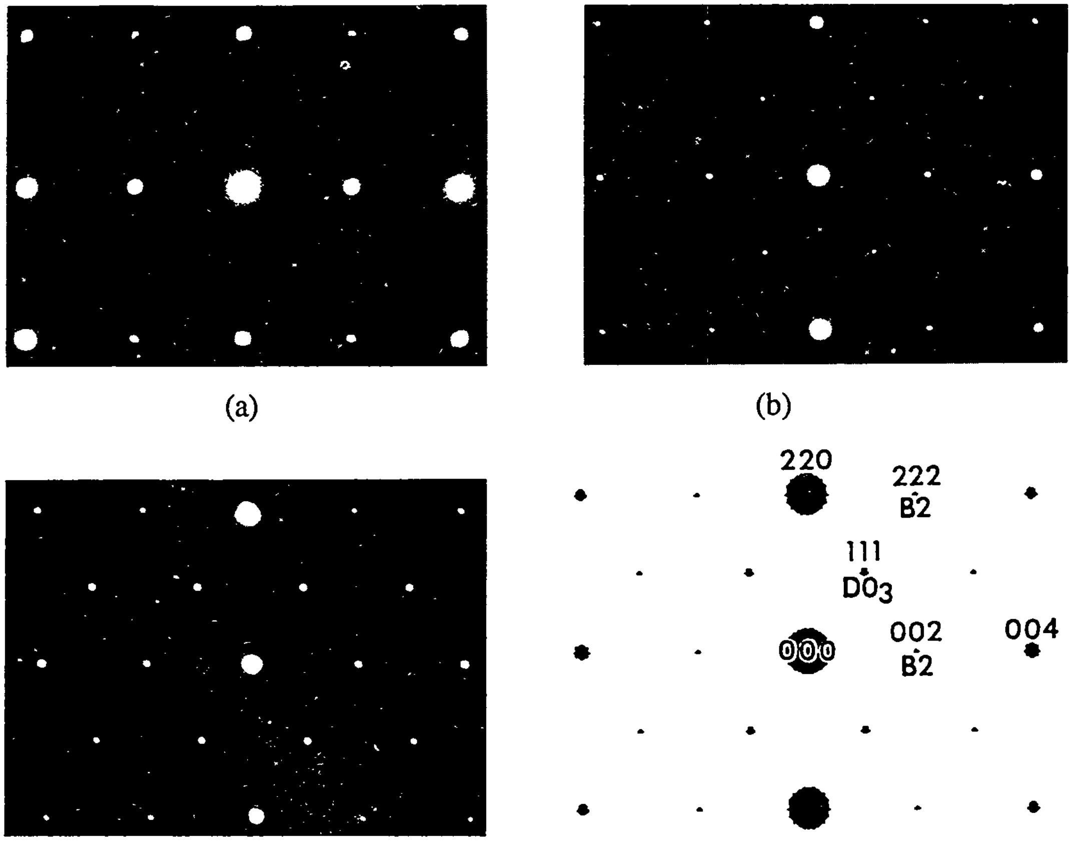
(a) (b) (c) (d)

Figure 3. Electron diffraction patterns from <110> oriented foils of FA-129 heat treated at (a) 600, (b) 700, and (c) 900°C and air cooled, and (d) schematic solution of the pattern.

developed low angle boundaries, retards the formation of DO_3 order. While the mechanism for this effect remains unclear, it has technological significance since retention of the B2 structure has been shown to increase the room temperature ductility.[4]

CHARACTERIZATION OF LOW ALUMINUM ALLOYS

Two different heats of the low aluminum alloy designated FAPY were examined in collaboration with Oak Ridge National Laboratory (ORNL). Heat 19669 was prepared by an outside vendor and had significantly higher aluminum and yttrium contents than Heat 15512 prepared by ORNL. The aluminum content of Heat 19669 was 1.5 wt.% higher than nominal and the yttrium content was 0.3 wt.% compared to a nominal value of 0.1

wt.%. The alloy prepared by the outside vendor exhibited brittle failure after heat treatment compared to the heat prepared by ORNL. Scanning electron microscopy indicated that the as-extruded heat 19669 failed by dimpled rupture, with Y rich particles apparently nucleating the dimples. After heat treatment at 800°C the dominant failure mode was transgranular. Upon higher temperature heat treatment (from 900 to 1300°C) the fracture mode changed to increasing intergranular failure. The TEM micrograph shown in Figure 4 shows Y rich precipitates along the grain boundaries of material heat treated at 1300°C that are thought to be responsible for the intergranular failure. The particles have been tentatively identified as $Fe_{23}Y_6$. Heat 15512 with nominal FAPY composition did not show any precipitates along the grain boundaries. It should also be noted that the dislocations present in Heat 19669 after high temperature treatment were decorated with precipitates, shown in Figure 5, that would effectively pin the dislocations and further restrict ductility.

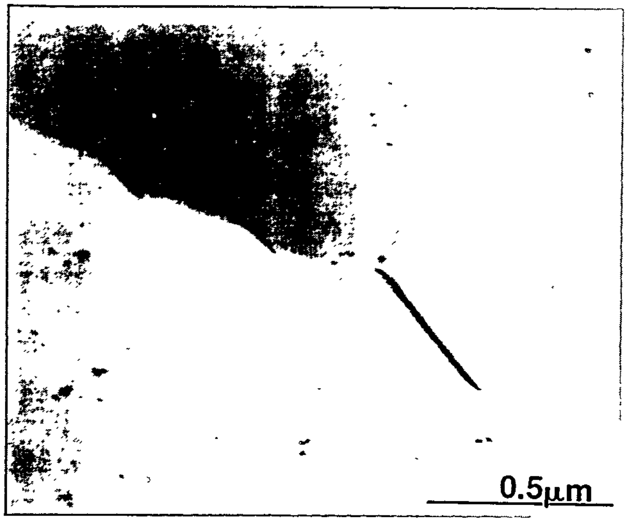

Figure 4. Bright field electron micrograph of $Fe_{23}Y_6$ grain boundary precipitates in FAPY Heat 19669.

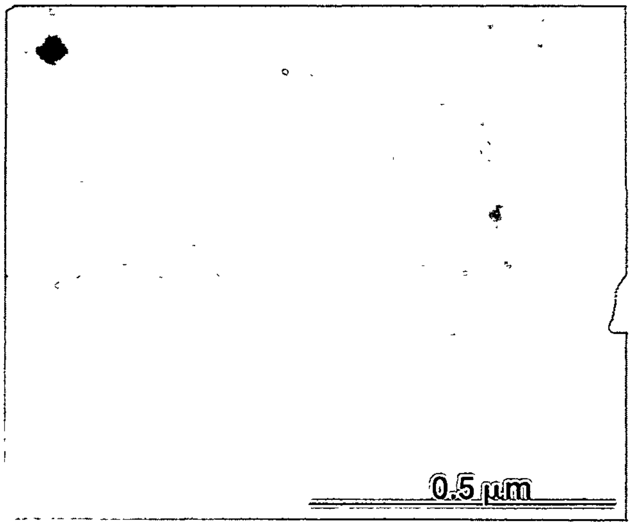

Figure 5. Bright field electron micrograph of precipitates on dislocations in FAPY Heat 19669.

REFERENCES

1. B. H. Rabin and R. N. Wright, "Microstructure and Tensile Properties of Fe_3Al Produced by Combustion Synthesis/Hot Isostatic Pressing," Metall. Trans., 23A (1992) p. 35-41.

2. J. K. Wright and R. N. Wright, "The Influence of Thermomechanical Processing on Microstructure and Properties of Iron Aluminides," Proceedings of the Seventh Annual Conference on Fossil Energy Materials, Oak Ridge, TN, May 1992, p. 209-218.

3. P. J. Maziasz, C. G. McKamey, O. B. Calvin, C. R. Hubbard, and T. Zacharia, "Some Effects of Composition and Microstructure on the B2 to DO_3 Order Transition in Fe_3Al Alloys," Mater. Res. Soc. Symp. Proc., (1992).

4. J. R. Knibloe, R. N. Wright, C. L. Trybus, and V. K. Sikka, "Microstructure and Mechanical Properties of Fe_3Al Alloys with Chromium," J. Mater. Sci., 28 (1993) p. 2040-2048.

FRACTURE BEHAVIOR OF THE Fe-8Al ALLOY FAP-Y

D. J. Alexander

Oak Ridge National Laboratory
Metals and Ceramics Division
P. O. Box 2008
Oak Ridge, TN 37831-6151

ABSTRACT

The tensile and impact properties of two heats of the reduced aluminum alloy FAP-Y have been measured and compared to the Fe_3Al alloy FA-129. The FAP-Y material has similar yield strengths up to 400°C, and much better ductility and impact properties, as compared to the FA-129. Despite excellent room-temperature ductility, the ductile-to-brittle transition temperature is still quite high, around 150°C. The material is found to be strain-rate sensitive, with a significant increase in the yield strength at strain rates of about 10^3 s^{-1}. It is believed that this strain-rate sensitivity is responsible, at least in part, for the high ductile-to-brittle transition temperature.

INTRODUCTION

Iron-aluminum alloys based on the Fe_3Al iron aluminide offer an attractive combination of excellent oxidation and sulfidation resistance with low cost and acceptable strength. Work at Oak Ridge National Laboratory (ORNL) and many other locations has resulted in significant improvements in the mechanical properties of these alloys. Although these alloys have potential for many applications, they can suffer from low ductility at room temperature due at least in part to environmentally induced embrittlement [1], and they have poor impact properties [2-4]. Recent work has shown that improvements in the tensile properties of iron-aluminum alloys can be achieved by reducing the aluminum content to about 8 weight percent [5]. Two heats of a low aluminum content alloy designated FAP-Y have been fabricated, and the tensile and impact properties have been measured for comparison to earlier data for an Fe_3Al-type alloy called FA-129 [4]. Some results from the first heat of FAP-Y have already been reported [6].

EXPERIMENTAL PROCEDURE

Two heats of FAP-Y were prepared at ORNL. The nominal composition of FAP-Y is Fe-8.5Al-5.5Cr-0.2Zr-2.0Mo-0.026C-0.1Y (wt %). The Fe_3Al-based alloy FA-129 [7] has the nominal composition of Fe-15.9Al-5.5Cr-1.0Nb-0.05C. The lower level of aluminum in FAP-Y will result in a disordered body-centered cubic (BCC) structure rather than the ordered B2 or DO_3 structure that the higher aluminum alloys would have. The FAP-Y alloy matches the FA-129 chromium content, with a molybdenum addition for pitting resistance [5]. The zirconium and carbon additions are intended to provide some control of the grain size. The alloy also contains a yttrium addition intended to enhance the corrosion resistance of the alloy to compensate for its lower aluminum content [8,9].

The first heat of FAP-Y (heat number 14953) was vacuum-induction melted, cast into a 75-mm-diam ingot, extruded into 15-mm-diam bar (extrusion ratio of 25:1), annealed for 1 h at 800°C, and air cooled. The second heat (15512) was also vacuum induction melted, cast into a 75-mm-diam ingot, and extruded to a diameter of 13 mm, for an extrusion ratio of approximately 36:1. The bar was annealed in air for 1 h at 800°C and then air cooled.

Full-size Charpy V-notch (CVN) impact specimens were fabricated from the extruded bars. The specimens were oriented along the length of the bars, with their notch perpendicular to the extrusion axis. The small diameter of the second bar resulted in the corners of these specimens being rounded. The specimens were not heat treated after machining.

The CVN specimens were tested on a semiautomated impact test machine. Specimens tested above 300°C were heated in a small box furnace to the desired temperature, as indicated on a dummy specimen instrumented with thermocouples. When the test temperature was reached, the specimen was removed from the furnace, located on the anvils with the aid of specially designed tongs, and broken as quickly as possible. No estimate of the drop in temperature has been made, and the furnace temperature has been used as the test temperature.

Small tensile specimens were fabricated from the broken halves of the CVN specimens by electrodischarge machining. Therefore, all of the specimens were oriented parallel to the extrusion direction. The specimens had a reduced section 1.78 × 2.54 × 6.35 mm long (0.070 × 0.100 × 0.250 in.) and were tested on a screw-driven electromechanical testing machine at a constant crosshead speed of 2.1×10^{-3} mm/s (0.005 in./min) for an initial strain rate of $3 \times 10^{-4}\ s^{-1}$. High-temperature testing was conducted with a split-tube furnace, and temperature was monitored throughout the test with a thermocouple spotwelded on one end of the specimen. All tests were conducted in laboratory air.

Sections parallel and transverse to the extrusion axis for both materials were metallographically polished and etched. The grain sizes were estimated by comparison to the ASTM standards for grain size. The fracture surfaces of the tensile and CVN specimens were examined in a scanning electron microscope.

RESULTS

The microstructures of the two heats are shown in Fig. 1. Both bars had equiaxed grain structures, with rows of inclusions aligned parallel to the extrusion axis. The inclusion content of the two heats appeared to be similar. However, the grain sizes of the two heats were very different. The first heat had a fine grain size, estimated to be ASTM grain size 7. This converts to an average linear intercept grain size of 28 μm. The second heat had a larger grain size, with ASTM number 5, an average linear intercept of 57 μm [10]. Thus, the grain size of the second heat was approximately twice as large as that of the first heat.

The tensile results are shown in Fig. 2. The yield strengths of the two heats of FAP-Y are similar, despite the difference in grain size, and are close to the FA-129 material [6]. At higher temperatures the ordered FA-129 retains it strength while the FAP-Y shows a decrease in strength with increasing test temperature. The tensile strength of the FAP-Y is higher than for FA-129 because of the premature failure of the FA-129 until the test temperature exceeds 400°C. At 600°C where the FA-129 has high ductility, it has a higher ultimate tensile strength. The ductility of the FAP-Y material is very high. The total elongation is about 40% at room temperature and rises as the test temperature increases. The FA-129 alloy has very low ductility up to at least 400°C.

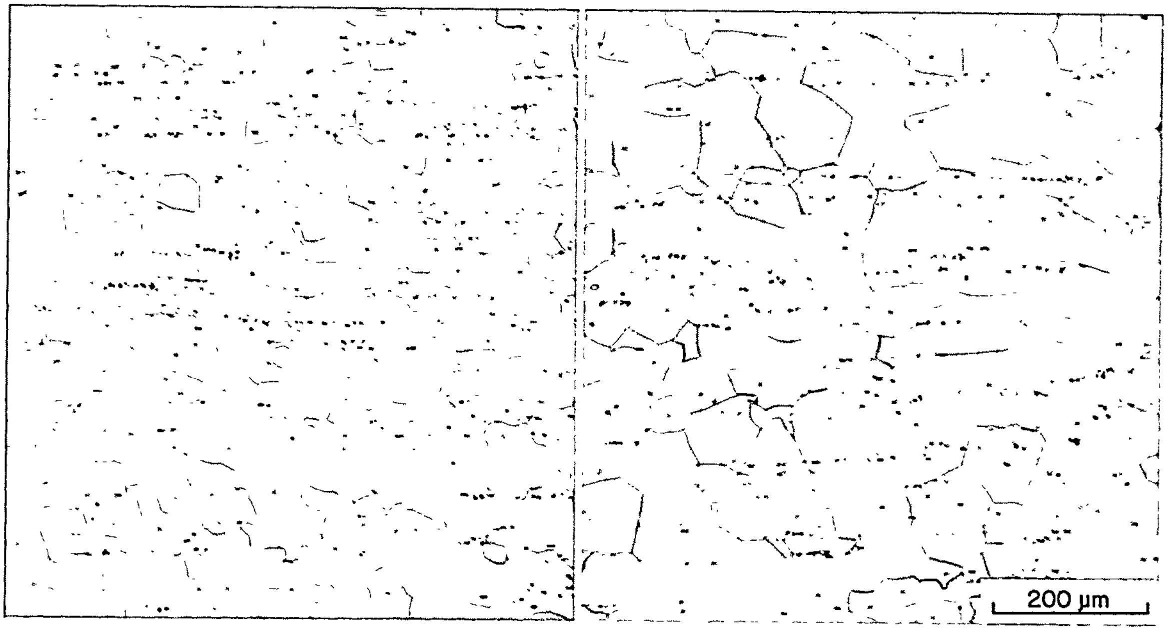

Fig. 1. Microstructures of the FAP-Y materials. Left: first heat. Right: second heat. Note the difference in grain size, and the particles aligned along the extrusion direction (left to right).

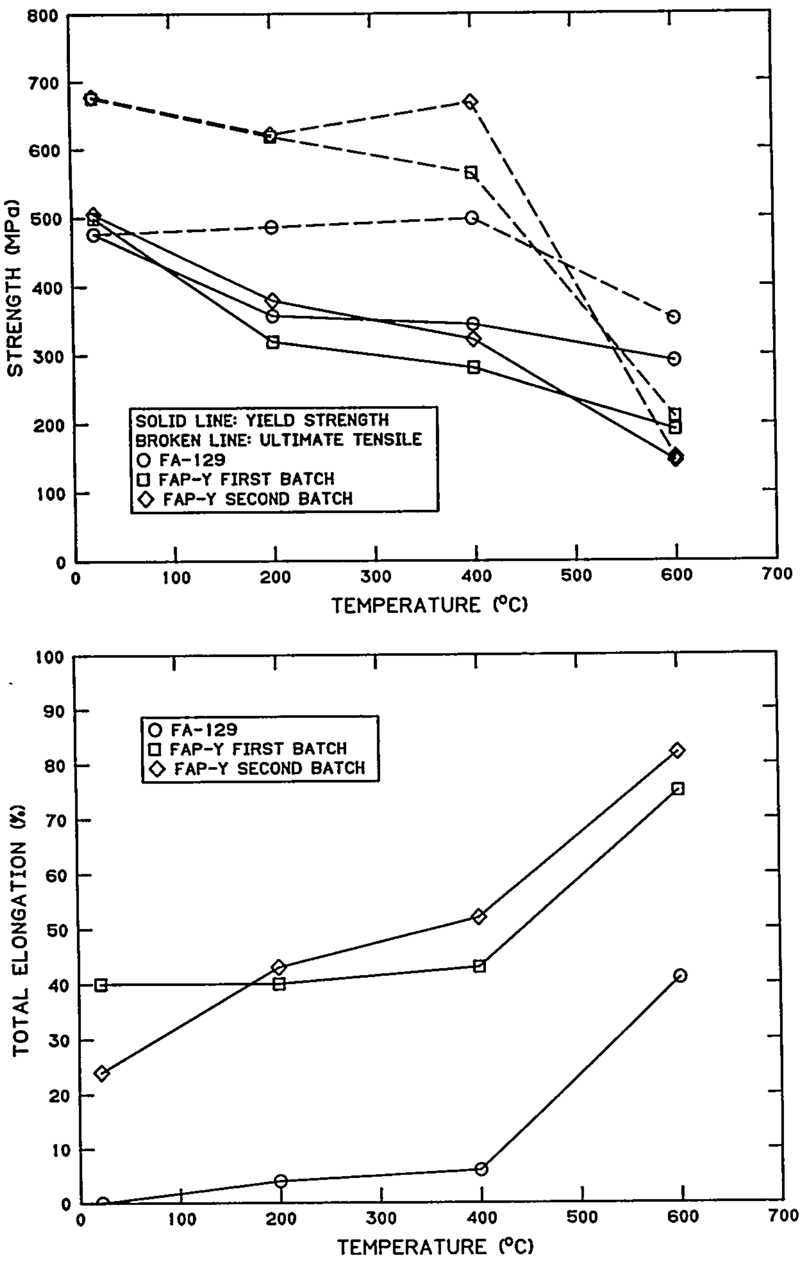

Fig. 2. Tensile properties of FAP-Y and FA-129. Top: yield strength and ultimate tensile strengths as a function of test temperature. Bottom: total elongation as a function of test temperature.

The results of the impact testing are shown in Fig. 3. The two heats of FAP-Y have similar behavior. Both show much greater levels of energy absorption on the upper shelf than the FA-129 [4] but have a high ductile-to-brittle transition temperature (DBTT) of about 150°C. Although this is much better than the DBTT of the FA-129, which is about 300°C, it is still surprisingly high for a material that shows such high ductility at room temperature.

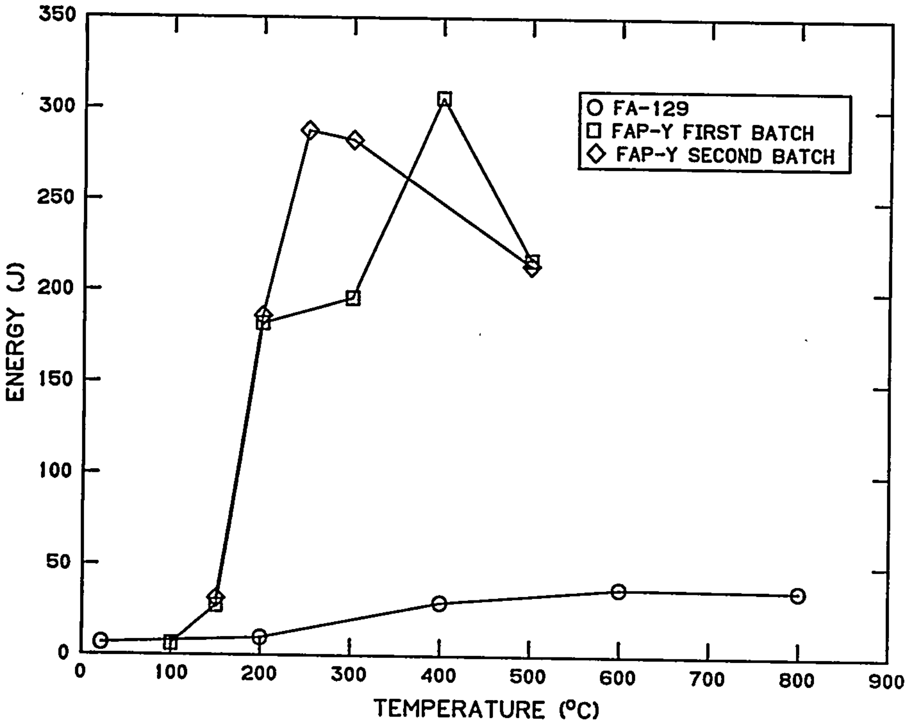

Fig. 3. Absorbed energy in impact vs test temperature for FAP-Y and FA-129.

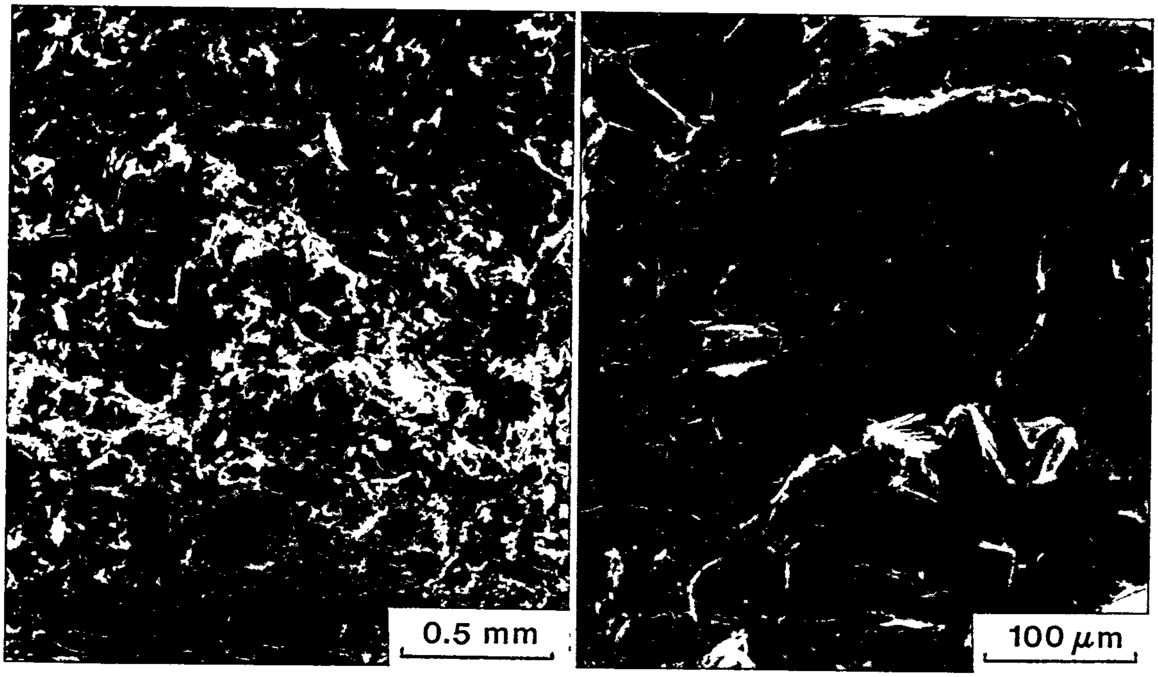

Fig. 4. Fractography for first heat of FAP-Y. Left: low magnification view of fracture surface of Charpy specimen tested at 150°C. Right: higher magnification, showing primarily cleavage fracture with some intergranular fracture.

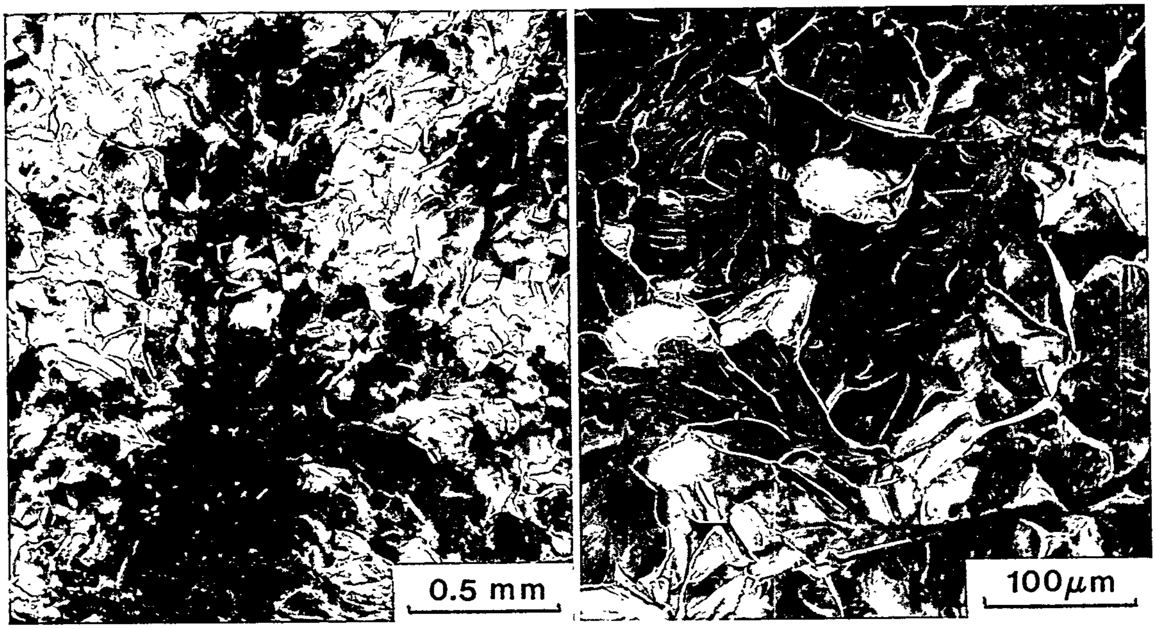

Fig. 5. Fractography for second heat of FAP-Y. Left: low magnification view of Charpy specimen tested at 150°C. Note the many particles on the fracture surface. Left: higher magnification showing cleavage fracture.

Examination of the fracture surfaces of Charpy specimens from the first heat of FAP-Y showed that fracture at low temperatures occurred primarily by cleavage, with some intergranular fracture (Fig. 4). At higher temperatures ductile fracture occurred by microvoid coalescence. Second-phase particles were associated with the ductile dimples. Specimens from the second heat showed larger fracture facets reflecting the larger grain size of the second heat. No intergranular fracture was observed, but many particles were present on the fracture surface (Fig. 5).

DISCUSSION

The reduced aluminum alloys offer similar strength levels to FA-129, but with much greater ductility. This improvement has been attributed to a reduced susceptibility to environmental embrittlement as a result of the lower aluminum content, since it is believed that the aluminum reacts with water vapor in the atmosphere to generate hydrogen that is responsible for the embrittlement [1,5]. In addition, dislocation movement should be much easier in the disordered BCC structure in the reduced aluminum alloys than in the ordered structure in FA-129. The FAP-Y alloy should also benefit from its fine, equiaxed grain structure. It is not clear whether this is due to the yttrium addition or the processing procedures.

An unexpected result is the similarity in the tensile and impact properties of the two heats of FAP-Y despite the factor of two difference in the grain size. The finer grain size of the first heat might be expected to result in a higher yield strength and a lower DBTT as compared to the second heat, but this is not observed. Grain boundary strengthening should be significant for this material, as there is not expected to be any contribution from second phases or precipitates in the matrix. The lack of effect of the grain size on the mechanical properties requires further investigation. Refinement of the grain size by appropriate processing should improve the impact properties of this material.

The high DBTT for the FAP-Y of about 150°C is surprising, considering the excellent tensile properties present at room temperature. Retained vacancies have been shown to have a significant effect on the mechanical properties of FeAl alloys [11]. Although it was not expected that vacancies would play a role in this disordered alloy, some Charpy specimens from the second heat were annealed at 400°C for 120 h. This heat treatment is effective for reducing the concentration of vacancies in FeAl alloys [12]. However, this anneal had no effect on the DBTT of the FAP-Y alloy.

Another possible explanation is that the alloy may be strain-rate sensitive. Recent work with thin sheet specimens of FAP-Y has indicated very little effect of strain rate on the yield strength of this alloy for strain rates from 10^{-6} to 10^{0} s^{-1} [8]. However, it seems likely that this material will exhibit strain-rate sensitivity at higher strain rates such as those associated with an impact test. To investigate this possibility, tensile specimens from the first heat were tested at faster speeds. The crosshead speed of the mechanical tester was increased up to 0.21 mm/s (0.5 in./min) for a strain rate of 3×10^{-2} s^{-1}. Speeds up to 70 mm/s (165 in./min) were obtained on a servohydraulic test machine for a strain rate of 11 s^{-1}. The load-stroke data were captured with a storage oscilloscope and then dumped to an X-Y plotter for analysis. Material from the second heat was also tested at several different strain rates at Los Alamos National Laboratory [13]. A split Hopkinson bar apparatus was used to obtain strain rates in compression as high as 5.5×10^{3} s^{-1}.

These tests showed that this material is strain-rate sensitive, with the yield strength increasing with strain rates above approximately 10^{-1} s^{-1} (see Fig. 6). At the highest strain rates tested the yield strength had risen from 500 to 800 MPa, a 60% increase.

This increase in the yield strength at high strain rates can explain, at least in part, the different behaviors observed in tensile and impact tests. The high ductility observed in the tensile tests occurs at slow strain rates. In the impact tests, the high strain rates will raise the yield stress. In addition, the notched geometry creates a hydrostatic stress field, and suppresses

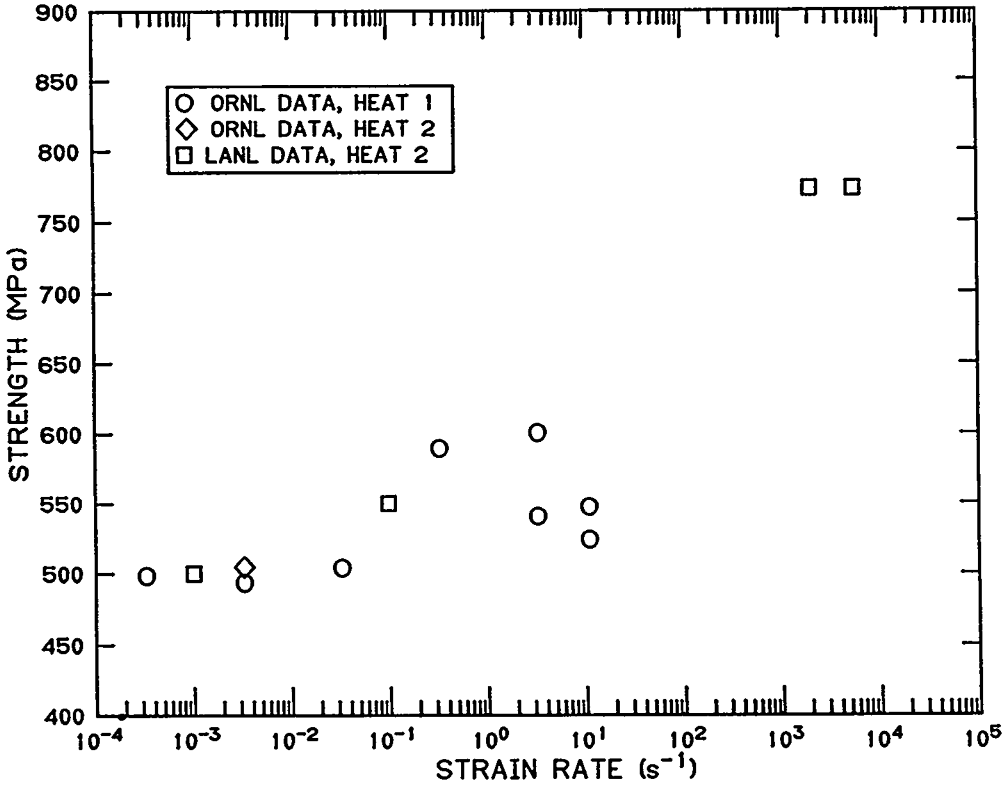

Fig. 6. Effect of strain rate on the room temperature yield strength of FAP-Y. The yield strength begins to increase for strain rates greater than about 10^{-1} s^{-1}.

plasticity. The notch will also increase the local strain rates even further. The suppression of yielding and the elevation of the yield stress results in the local stresses reaching the cleavage fracture stress, with fracture rather than plasticity being the result.

The FAP-Y material also shows a tendency for intergranular fracture. This may contribute to the poor impact resistance, but since the brittle fracture surface is primarily cleavage, the intergranular fracture is not believed to play a major role.

CONCLUSIONS

The tensile and Charpy impact properties of two heats of the reduced aluminum alloy FAP-Y have been measured. Both heats showed similar ductile-to-brittle transition temperatures of about 150°C, and similar tensile properties, with roughly 40% total elongation at room temperature. The FAP-Y alloy is strain-rate sensitive, with the yield strength increasing by about 60% when the strain rate is increased from 10^{-1} to 10^{3} s^{-1}. The combined effects of the notched geometry in the impact specimens, which creates a triaxial stress field and suppresses plasticity, and the strain rate sensitivity, which elevates the yield stress at high strain rates, are believed to be the reasons for the high DBTT despite the excellent tensile ductility of this material at low strain rates. Developing a better understanding of the processing response of this alloy in order to achieve a refined grain size is necessary to determine whether a finer grain size may be helpful.

ACKNOWLEDGMENTS

This research was sponsored by the U.S. Department of Energy, Fossil Energy AR&TD Materials Program (DOE/FE AA 15 10 10 0) under contract DE-AC05-84OR21400 with Martin Marietta Energy Systems, Inc. We would like to thank C. G. McKamey and V. K. Sikka for their helpful reviews of the manuscript, which was prepared by J. L. Bishop.

REFERENCES

1. C. T. Liu, C. G. McKamey, and E. H. Lee, "Environmental Effects on Room-Temperature Ductility and Fracture in Fe_3Al," Scripta Metall. Mater., 24 (1990), p. 385.

2. D. J. Alexander and V. K. Sikka, "Fracture Behavior of Fe_3Al Alloy FA-129," in Proceedings of the Fifth Annual Conference on Fossil Energy Materials, Conf-9105184, ORNL/FMP-91/1, Oak Ridge National Laboratory, Oak Ridge, TN, 1991, p. 239.

3. D. J. Alexander and V. K. Sikka, "Fracture of Iron Aluminide Alloys," in Proceedings of the Sixth Annual Conference on Fossil Energy Materials, ORNL/FMP-92/1, Oak Ridge National Laboratory, Oak Ridge, TN, 1992, p. 295.

4. B. G. Gieseke, D. J. Alexander, V. K. Sikka, and R. H. Baldwin, "Mechanical Properties of Ductile Fe_3Al-Based Plates," Scripta Metall. Mater., 29 (1993), p. 129.

5. V. K. Sikka, S. Viswanathan, and S. Vyas, "Acceptable Aluminum Additions for Minimal Environmental Effect in Iron-Aluminum Alloys," in High-Temperature Ordered Intermetallic Alloys V, I.Baker, R.Darolia, J. D. Whittenberger, and M. H. Yoo, eds., Mat. Res. Soc. Symp. Proc. Vol. 288, Materials Research Society, Pittsburgh, 1993, p. 971.

6. D. J. Alexander and V. K. Sikka, "Mechanical Properties of Iron-Aluminum Alloys," Proceedings of the Seventh Annual Conference on Fossil Energy Materials, CONF-9305135, ORNL/FMP-93/1, Oak Ridge National Laboratory, Oak Ridge, TN, 1993, p. 219.

7. V. K. Sikka, C. G. McKamey, C. R. Howell, and R. H. Baldwin, "Fabrication and Mechanical Properties of Fe_3Al-Based Iron Aluminides," ORNL/TM-11465, Oak Ridge National Laboratory, Oak Ridge, TN, 1990.

8. V. K. Sikka, S. Viswanathan, and C. G. McKamey, "Development and Commercialization Status of Fe_3Al-Based Intermetallic Alloys," in Structural Intermetallics, R. Darolia et al., eds., The Minerals, Metals and Materials Society, Warrendale, PA, 1993, p. 483.

9. V. K. Sikka, R. H. Baldwin, and C. R. Howell, "Low-Aluminum Content Iron-Aluminum Alloys," Proceedings of the Seventh Annual Conference on Fossil Energy Materials, CONF-9305135, ORNL/FMP-93/1, Oak Ridge National Laboratory, Oak Ridge, TN, 1993, p. 197.

10. Standard Test Methods for Determining Average Grain Size, E 112-88, American Society for Testing and Materials, Philadelphia, 1992.

11. I. Baker and P. Nagpal, "A Review of Flow and Fracture of FeAl," in Structural Intermetallics, R. Darolia et al., eds., The Minerals, Metals and Materials Society, Warrendale, PA, 1993, p. 463.

12. P. Nagpal and I. Baker, "Effect of Cooling Rate on Hardness of FeAl and NiAl," Metall. Trans. A, 21A (1990), p. 2281.

13. G. T. Gray, III, Los Alamos National Laboratory, personal communication to D. J. Alexander, Oak Ridge National Laboratory, June 1994.

INVESTIGATION OF MOISTURE-INDUCED EMBRITTLEMENT OF IRON ALUMINIDES

A. Castagna and N.S. Stoloff

Rensselaer Polytechnic Institute
Materials Engineering Department
Troy, NY 12180-3590

ABSTRACT

The influence of several gaseous environments (hydrogen gas, air, and oxygen) on the fatigue crack growth resistance and ductility of a disordered iron-aluminum alloy (FAP-Y) has been determined. Hydrogen gas is found to be most detrimental to crack growth resistance and ductility, while tests in oxygen reveal the lowest crack growth rates and highest ductility. Testing in air resulted in mechanical properties similar to those in oxygen. TEM analysis of dislocation substructures and SEM analysis of fractographic features will be discussed in the context of the mechanism of environmental embrittlement.

The embrittling effect of hydrogen gas on FAP-Y is similar to that on a Fe-28a%Al ordered intermetallic, FA-129, which has been studied previously. The higher aluminum FA-129, however, is also severely embrittled by laboratory air, while FAP-Y is not. It was found that the low aluminum FAP-Y exhibits higher room temperature ductility than FA-129, but less resistance to fatigue crack growth.

INTRODUCTION

Binary iron aluminides display limited room temperature ductility in air, typically 4-8% (ref. 1,2). Like many other intermetallics and steels, direct exposure to hydrogen lowers the room temperature ductility even further. Research conducted at Oak Ridge has shown that the predominant environmental embrittlement mechanism in Fe_3Al involves a chemical reaction with water vapor in the air and aluminum at the surface of the material [3]. Only a small vapor pressure of water is necessary to sharply reduce ductility [4]. Recently, Sikka and co-workers have reported that environmental embrittlement does not occur when aluminum content is reduced to 16a% or less, such that the alloy becomes completely disordered [5]. Alternatively, alloying of Fe_3Al with about 5a% Cr reduces the susceptibility to moisture-induced embrittlement. The purpose of this paper is to examine and compare the tensile and fatigue behavior of two iron-aluminum alloys in moisture and hydrogen-bearing environments. The first is a disordered alpha type alloy with 16a% Al, designated FAP-Y. The second is an ordered intermetallic with 28a% Al, designated FA-129.

EXPERIMENTAL PROCEDURES

Material

The composition of alloy FAP-Y is 16.12a% Al, 5.44a% Cr, 1.07a% Mo, 0.11a% Zr, 0.13a% C, 0.06a% Y, balance Fe, and that of alloy FA-129 is 28.08a% Al, 5.04a% Cr, 0.51a% Nb, 0.20a% C, balance Fe. FA-129 is an ordered Fe_3Al type intermetallic that can exist in the B2 or DO_3 ordered state, depending on the annealing parameters used, while FAP-Y is disordered. Both alloys are fabricated at the Oak Ridge National Laboratory (ORNL) by vacuum induction melting, extrusion to a 2.54 cm thickness, and either hot or warm rolling to the final thickness of 5.08 mm. Plate used in tensile tests of FA-129 was rolled further to 0.76 mm.

FAP-Y was annealed twice at 800°C for one hour with a furnace cool. The annealing parameters for B2 ordered FA-129 consisted of a 700°C anneal for 1 hour with a mineral oil quench, which was then repeated. The annealing parameters for DO_3 ordered FA-129 were the same as for the B2 order heat treatment, with an additional reheat to 500°C for four days with a furnace cool. These heat treatments resulted in a grain size of 42 μm for FAP-Y and a partially recrystallized structure for FA-129. The microstructures for FAP-Y and FA-129 are shown in Figs. 1a) and 1b), respectively.

Tensile Tests

Tensile tests were conducted on alloys FAP-Y and FA-129 in hydrogen gas, laboratory air, and oxygen gas. Alloy FA-129 was tested in the B2 condition at 25°C, 150°C, and 600°C, and in the DO_3 condition at 25°C, 150°C, 300°C, and 450°C. Alloy FAP-Y was tested only at 25°C. Results at 25°C represent the average of two tests, and all others represent single tests. Tensile test specimens of FAP-Y were machined with gauge section dimensions of 12.7 mm x 3.2 mm x 1.9 mm. The FA-129 specimens were punched from 0.76 mm thick plate, with gauge section dimensions of 12.7 mm x 3.2 mm x 0.76 mm thick. The tensile specimens were polished to a 0.3 μm finish prior to testing. All tensile specimens were pin loaded and tested in a servo-hydraulic MTS machine in stroke control at a strain rate of 3.3×10^{-4} /sec. When testing in oxygen or hydrogen gas, the environmental chamber was first evacuated to $< 1.3 \times 10^{-4}$ Pa. The appropriate gas was then admitted to the chamber at a pressure of 2300 Pa (1/3 psi) over atmospheric pressure.

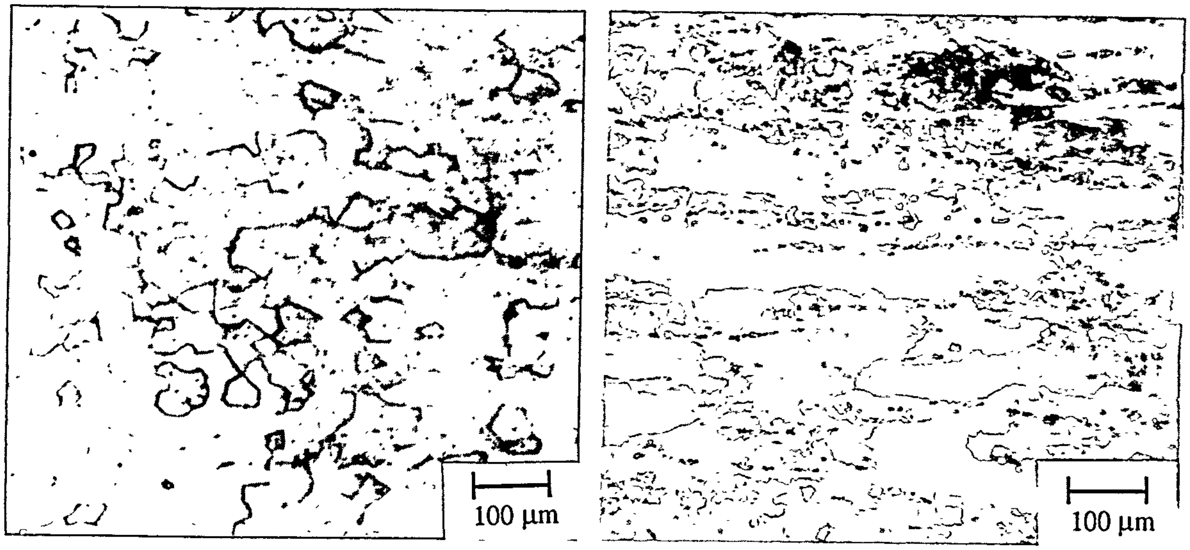

a) FAP-Y with 800°C/1hr anneal

b) FA-129 with 700°C/1hr anneal (B2 order)

Fig. 1. Microstructure of annealed FAP-Y and FA-129

Fatigue Crack Growth Tests

Fatigue crack growth tests were performed on alloy FA-129 in both the B2 and DO3 ordered states, and on alloy FAP-Y. Room temperature tests were conducted in hydrogen gas, laboratory air, and oxygen on FAP-Y and B2 and DO_3 ordered FA-129. Elevated temperature fatigue crack growth tests were conducted on FA-129 in laboratory air at 150°C in the B2 and DO3 ordered state, and at 300°C and 450°C in the DO3 ordered state.

Compact tension specimens were used in all fatigue tests and were cut by wire Electro-Discharge Machining such that the crack propagation direction would be perpendicular to the rolling direction. Crack length was monitored via the d.c. potential drop method. Temperature was monitored at the specimen surface to correct for bulk resistivity changes using a chromel-alumel thermocouple cemented to the CT specimen. All parameters of the fatigue crack growth tests followed the ASTM E-647 procedures with the exception of the CT specimen size, which was slightly undersized due to constraints in material availability.

RESULTS

The results of tensile tests on FA-129 are shown in Table I, and those for alloy FAP-Y are shown in Table II.

Table I - Tensile Data for FA-129

		Air			Vac			O_2		
Order	Temp	Duct.	YS	UTS	Duct.	YS	UTS	Duct.	YS	UTS
B2	25 °C	8.8	409	677	13.7	412	859	16.2	440	858
	150 °C	16.7	369	865	16.5	409	885	23.4	417	936
	600 °C	30.7	303	351	38.5	293	392	41.8	306	416
DO_3	25 °C	3.4	495	645	4.8	547	897	5.8	580	904
	150 °C	15.2	415	846	16.9	414	938	23.1	436	958
	300 °C	29.3	367	934	27.0	420	977	29.5	423	987
	450 °C	24.2	369	683	25.5	412	679	26.2	420	717

ductility = plastic strain at failure in %, YS and UTS in MPa

Table II - Tensile Properties of Alloy FAP-Y at 25°C

Environment	Ductility (%)	YS (MPa)	UTS (MPa)
Hydrogen	6.3	484	614
Air	25.5	487	665
Oxygen	24.0	498	653

ductility = plastic strain at failure in %, YS and UTS in MPa

Alloy FA-129 clearly shows the effect of moisture in air on ductility and UTS. Ductility and UTS were greatly increased at room temperature by testing in vacuum and oxygen (see Table I). In addition, a large increase in ductility and UTS is found when increasing the temperature of the tests from 25°C to 150°C..

In contrast, alloy FAP-Y demonstrates no embrittlement in laboratory air. However, FAP-Y shows embrittlement in gaseous hydrogen. The ductility in hydrogen is decreased to 6.3% from 25.5% in air and 24.0% in oxygen (see Table II). Note that alloy FA-129 exhibits a great deal of strain hardening, and therefore the UTS is reduced as ductility is reduced when tested in air, because less strain hardening occurs. This effect is not seen in alloy FAP-Y, which exhibits very little strain hardening.

Figs. 2 a) and 2b) show the fracture surfaces of alloy FAP-Y tensile tested in gaseous hydrogen, and air, respectively. The change from transgranular cleavage in hydrogen gas (Fig. 2a) to mixed transgranular cleavage and dimples in air (Fig. 2b) is clear. The fracture surface of FAP-Y tested in tension in oxygen is similar to that tested in air. In alloy FA-129, the change in fracture surface occurs when the environment is changed from air to oxygen. Fig. 3a) shows a mixed transgranular-intergranular surface in B2 ordered FA-129 tested in air, while Fig. 3b) shows the predominantly transgranular surface for B2 ordered FA-129 tested in oxygen.

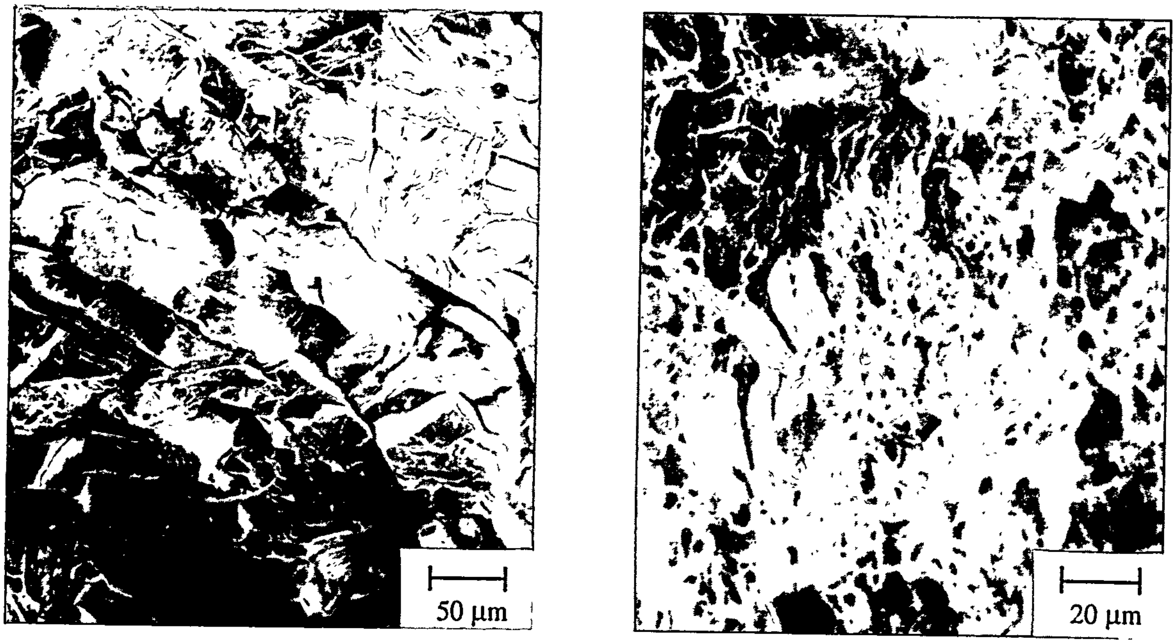

a) hydrogen b) air

Fig. 2. Fracture surfaces of FAP-Y tested in tension at 25°C, a) hydrogen, b) air.

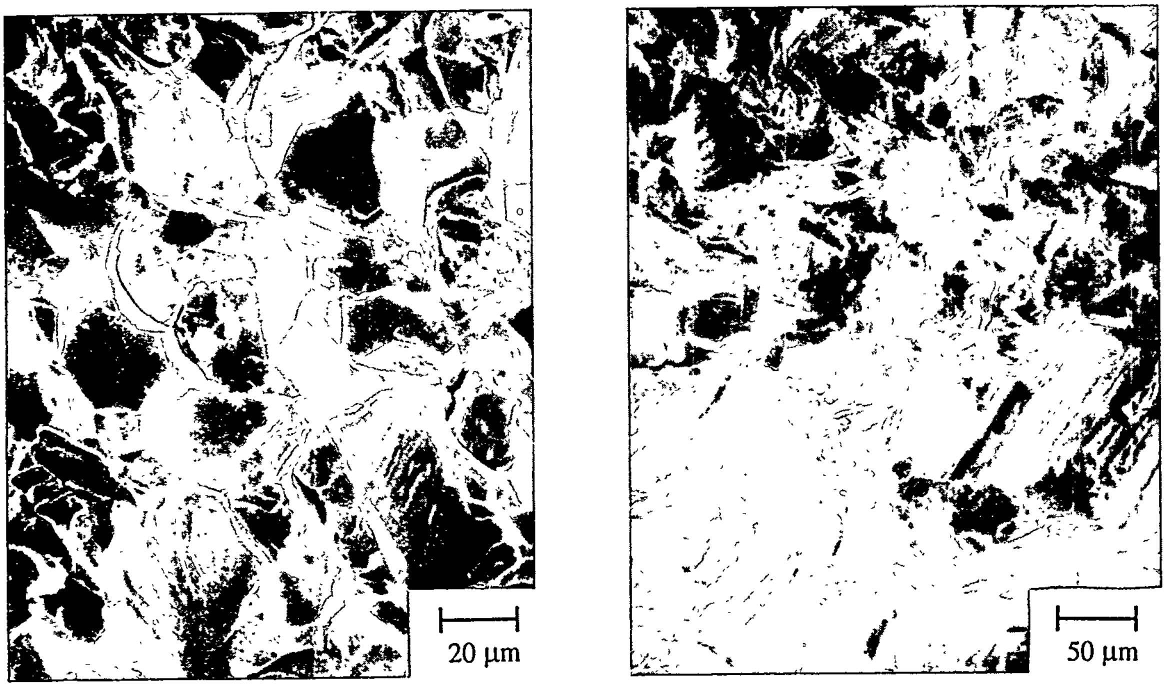

a) air

b) oxygen

Fig. 3. Fracture surfaces of B2 ordered FA-129 tested in tension at 25°C, a) air, b) oxygen.

The results of the fatigue crack growth tests are tabulated in Table III. Threshold and critical stress intensities, the slope m of the Paris equation, { $da/dN = C(\Delta K)^m$ }, and the fracture surface appearance are listed. The da/dN curves generated for FA-129 and FAP-Y in various environments at 25°C are shown in Fig. 4. Note that stable crack growth could not be achieved for FAP-Y in hydrogen gas.

Table III shows that hydrogen gas produces the highest crack growth rates in all cases while oxygen produces the lowest rates. In addition, crack growth rates in alloy FAP-Y are higher than those in DO_3 ordered FA-129 which are, in turn, higher than those in B2 ordered FA-129. The difference in critical stress intensity in alloy FAP-Y between air and oxygen (8.5%) was much smaller than in B2 (16%) or DO_3 (21%) ordered FA-129, indicating that FAP-Y is less susceptible to moisture-induced embrittlement.

Table III shows also that the average value of m (slope of the da/dN curve) increases rapidly as the environment changes from oxygen to air to hydrogen gas at 25°C, with the greater change for DO_3 ordered FA-129 (3.0 in O_2 to 8.8 in H_2 for B2 and 8.5 in O_2 to 25.1 in H_2 for DO_3). The values of m are also consistently higher in FAP-Y than in DO_3 ordered FA-129, and the values of m for DO_3 ordered FA-129 are consistently higher than in B2 ordered FA-129. As with the change in critical stress intensity, the difference in slope m between air and oxygen in alloy FAP-Y is less than the difference measured between air and oxygen for B2 and DO_3 ordered FA-129.

Table III Fatigue Crack Growth Data for Fe_3Al Alloys

Alloy	Environment	Fracture Surface	m	ΔK_{TH} ($MPa\sqrt{m}$)	ΔK_C ($MPa\sqrt{m}$)
FA-129 (B2)	O_2, 25°C	Dimpled, few striations	3.0	20.0	35.9
FA-129 (B2)	Air, 25°C	TG, many striation	6.9	14.5	29.9
FA-129 (B2)	H_2, 25°C	TG, few striations	8.8	13.8	25.9
FA-129 (DO_3)	O_2, 25°C	Dimpled + cleavage	8.5	13.5	25.1
FA-129 (DO_3)	Air, 25°C	Cleavage + IG	11.2	13.3	19.8
FA-129 (DO_3)	H_2, 25°C	Cleavage + IG	25.1	11.1	17.4
FAP-Y	O_2, 25°C	TG	19.7	9.9	12.8
FAP-Y	Air, 25°C	TG	22.2	10.0	11.7
FAP-Y	H_2, 25°C	—	—	—	—

The fracture surfaces of B2 ordered FA-129 were predominantly transgranular, with a dimpled appearance in oxygen (Fig. 5a). Occasional striations are evident, such as in B2 ordered FA-129 fatigued in air (Fig. 5b). The striation spacing was found to be larger than the corresponding value of da/dN, and appears to have a cleavage nature. In the more aggressive environments (air and hydrogen gas) the fracture surface exhibits more pronounced cleavage facets.

DO_3 ordered FA-129 exhibits a shift in fracture mode at room temperature. In oxygen the surface is transgranular with a dimpled appearance, again suggesting microvoid coalescence (Fig. 6a). In air (Fig. 6b) and hydrogen gas the surface shows a mix of intergranular and transgranular cleavage failure.

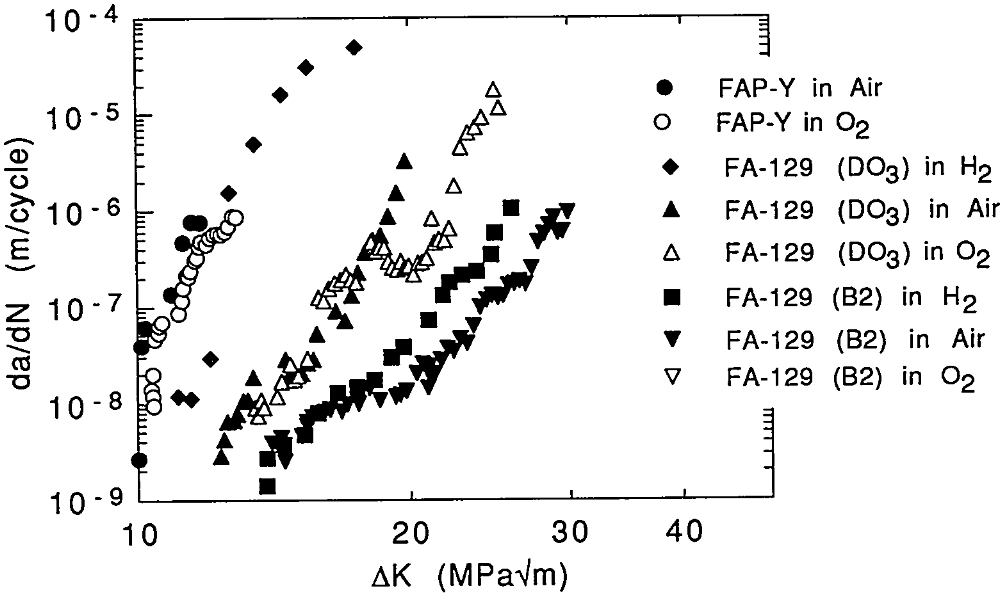

Fig. 4. Fatigue crack growth curves for FA-129 and FAP-Y at 25°C.

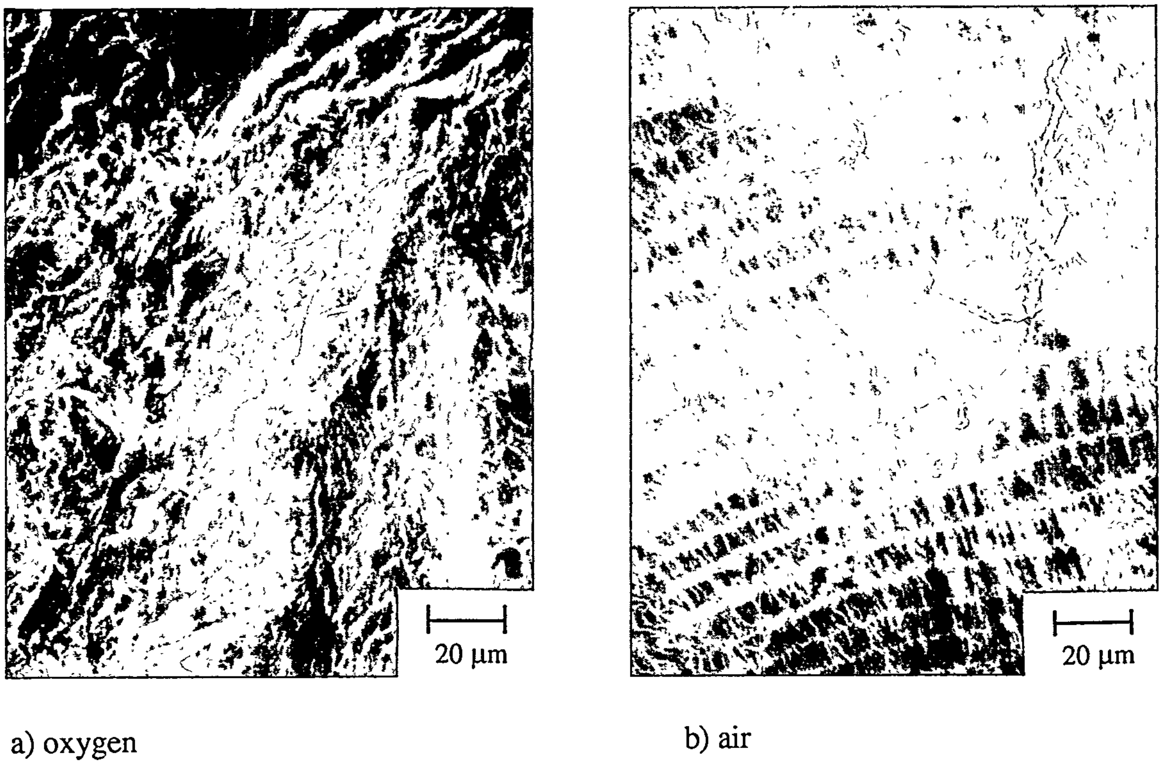

a) oxygen

b) air

Fig. 5. Fracture surface of B2 ordered FA-129 fatigued at 25°C, a)oxygen, b) air.

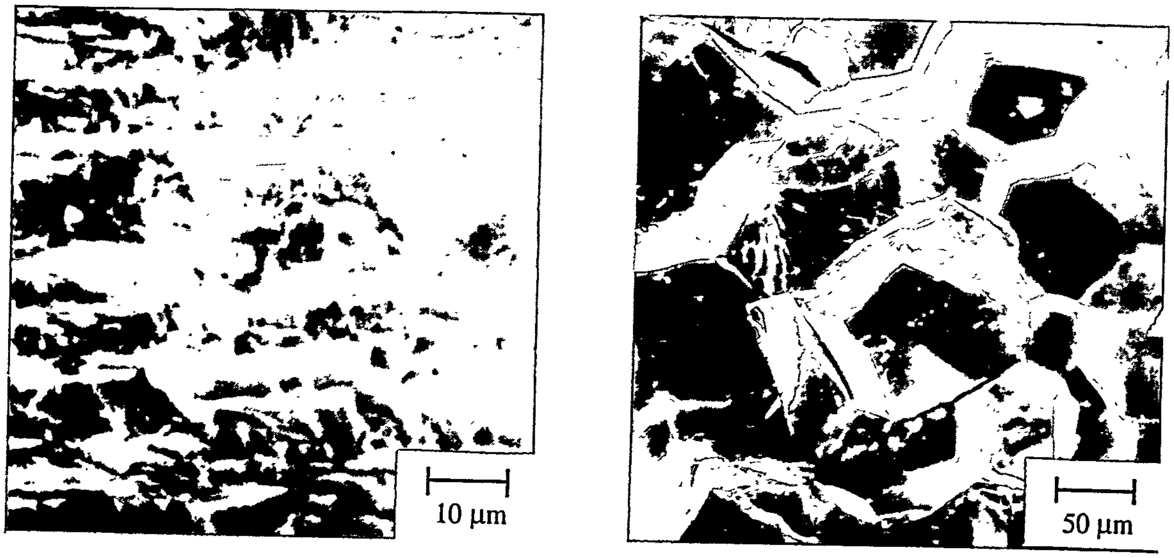

a) oxygen b) air

Fig. 6. Fracture surfaces of DO_3 ordered FA-129 fatigued at 25°C, a) oxygen, b) air.

The fracture surface of alloy FAP-Y shows a transgranular appearance in both oxygen (Fig. 7a) and air (Fig. 7b). The similarity of the fracture surfaces in air and oxygen is consistent with the similarity between the crack growth curves measured in these two environments.

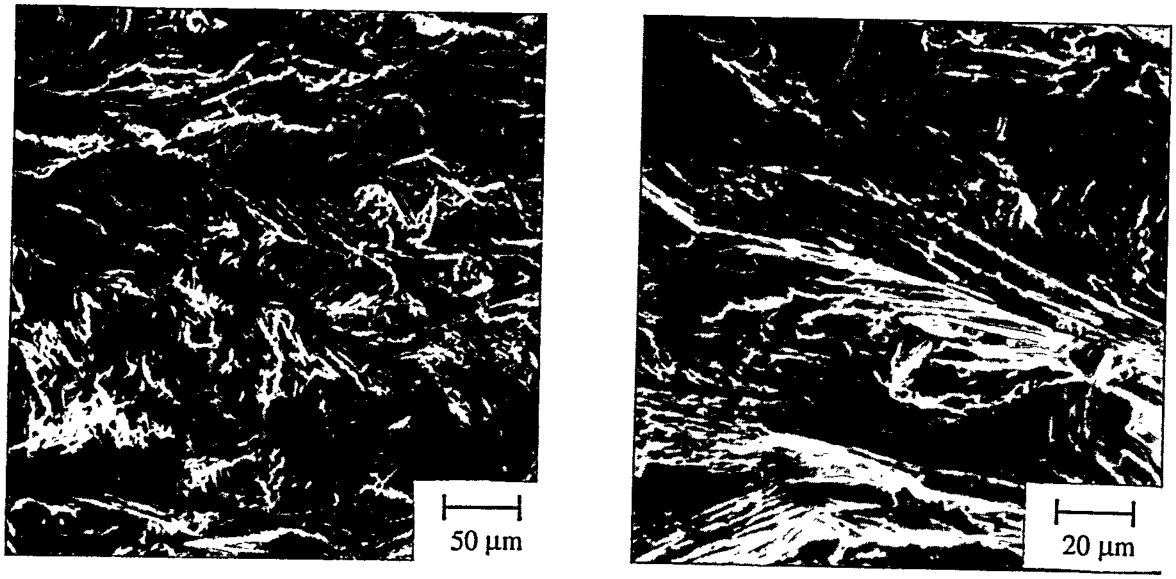

a) oxygen b) air

Fig. 7. Fracture surfaces of FAP-Y fatigued at 25°C, a) oxygen, b) air.

DISCUSSION

The results of tensile and fatigue testing on alloys FAP-Y and FA-129 indicate that the lowering of alloy aluminum content to 16a% appears to remove or reduce the susceptibility to water vapor. FAP-Y suffered no loss of ductility when tested in tension in air, as opposed to oxygen (see Table II), while FA-129 is severely embrittled. In addition, only a slight loss of fracture toughness was found when FAP-Y was fatigued in air, as opposed to oxygen. However, this finding does not preclude a substantial loss of ductility when the low aluminum alloy is exposed directly to hydrogen gas. FAP-Y suffers a 75% drop in ductility between air and hydrogen environments. When FAP-Y was fatigued in hydrogen gas, embrittlement was so severe that stable crack growth could not be achieved. Similar results on low Al alloys have recently been reported by Buchanan et al [6], who showed that electrolytic charging with hydrogen during slow strain rate tests of FAP-Y reduced ductility from 17% to about 5% . Similar tests on a Fe-23.5 % Al binary caused a reduction of elongation from 7% to about 1% (ref. 3). Both sets of data agree in that FA-129 is more susceptible to moisture and to hydrogen than is FAP-Y. Equally clear is the fact that reducing aluminum content so as to leave the ordering range is not sufficient to preclude embrittlement by gaseous or electrolytically generated hydrogen.

The differing response of FAP-Y to moisture and to hydrogen is characteristic of several other alloy systems, including the intermetallics Ni_3Al+B [7] and Ni_3Fe [8]. None of these alloys display reduced ductility in air, yet they are all embrittled to some extent by hydrogen. This suggests that, in order for moisture to be detrimental, a minimum level of some reactive element such as aluminum be present to foster the dissociation of water. In the case of Ni_3Al+B there is the further complication that boron and hydrogen liberated from water compete for the same grain boundary sites, such that boron is able to suppress embrittlement. However, when sufficient hydrogen is present, as in 1 atm. hydrogen gas or when hydrogen is charged electrolytically, the boron present is insufficient to block the embrittling hydrogen. In the case of Ni_3Fe, neither element is reactive enough to dissociate water vapor, resulting in lack of any observable embrittlement [8].

One of the most surprising results of this investigation is the very high fatigue crack growth rate of FAP-Y compared to that of Fe_3Al in air. To some extent this result may arise from the beneficial effects of an ordered structure on fatigue crack growth resistance (particularly in the case of $L1_2$ alloys) [9]. However, the much greater susceptibility of FA-129 to moisture in tension compared to that of FAP-Y suggested that the latter would exhibit slower crack growth in air. Further work is in progress to try to identify the mechanism for rapid crack growth in FAP-Y.

ACKNOWLEDGMENTS

The authors are grateful to the Department of Energy, Fossil Energy Program for providing financial support under Martin Marietta Energy Subsystems. Subcontract No. 19X-SF521C. Assistance also was provided by the Oak Ridge National Laboratory SHaRE program and Dr. P.J. Maziasz. The authors also are grateful for helpful discussion with Drs. C.T. Liu and V.K. Sikka of ORNL and to Dr. Sikka for provision of test alloys.

REFERENCES

1. C.G. McKamey, J.H. DeVan, P.E. Tortorelli, and V.K. Sikka, *J. Materials Research* 6 (1991) 1779

2. M. Shea, A. Castagna, and N.S. Stoloff in L.A. Johnson, D.P. Pope, and J.O. Stiegler (eds.), *High Temperature Ordered Intermetallics IV*, MRS Symp. Proc. v. 213, Pittsburgh PA (1991) 609-613

3. C.T. Liu, H.E. Lee, and C.G. McKamey; *Scripta Met.* 23 (1989) 875-880

4. C.G. McKamey, and E.H. Lee, in I. Baker, R. Darolia, J.D. Darolia, J.D. Whittenberger, and M.H. Yoo (eds.), *High Temperature Ordered Intermetallics V*, MRS Symp. Proc. v. 288, Pittsburgh PA (1993) 983-988

5. V.K. Sikka, S. Viswanathan, and S. Vyas, in I. Baker, R. Darolia, J.D. Darolia, J.D. Whittenberger, and M.H. Yoo (eds.), *High Temperature Ordered Intermetallics V*, MRS Symp. Proc. v. 288, Pittsburgh PA (1993) 971-976

6. R.A. Buchanan and J.G. Kim, Dept. of Energy, Fossil Energy Advanced Research and Development Materials Program, Report ORNL/Sub/88-07685CT92/02, (Springfield, VA:NTIS, August, 1992)

7. A.K. Kuruvilla and N.S. Stoloff, *Scripta Met.*, 19 (1985) 83-87

8. G.M. Camus, N.S. Stoloff, and D.J. Duquette, *Acta Met.*, 37 (1989) 1497-1501

9. N.S. Stoloff, G.E. Fuchs, A.K. Kuruvilla, and S.J. Choe, in N.S. Stoloff, C.C. Koch, C.T. Liu, and O. Izumi (eds.), *High Temperature Ordered Intermetallics II*, MRS Symp. Proc. v. 81, Pittsburgh PA (1987) 247-261

ENVIRONMENTAL EFFECTS ON IRON ALUMINIDE

J. H. DeVan, P. F. Tortorelli, and M. J. Bennett*

Oak Ridge National Laboratory
P. O. Box 2008
Oak Ridge, Tennessee 37831-6156

Consultant, South Moreton, England, OX11 9AH

ABSTRACT

Air oxidation tests of iron-aluminum alloys containing 16 and 28 atom % Al, respectively, were conducted at 1300°C to determine the effect of alloy composition and section thickness on the time to breakdown of oxidation resistance. The oxidation rates of the 16% Al alloy were significantly higher than for 28% Al (Fe_3Al) alloys. The times over which the oxide scales remained protective correlated with the extent of aluminum depletion of the alloy matrix and were therefore a direct function of the initial aluminum content of the alloy, the section thickness, and the oxidation rate. The oxidation rate of the Fe_3Al alloys was significantly reduced by the addition of 0.1% Zr, which improved the adherence of the scale during thermal cycling to room temperature. However, the oxidation rates of the Fe_3Al alloys were higher at 1300°C than those reported for oxide-dispersion-strengthened (ODS) Fe-18%Cr-10%Al alloys containing Y_2O_3. Times to the onset of breakaway oxidation were similar for zirconium-containing Fe_3Al and the ODS alloys, the lower oxidation rate of the latter offsetting the higher initial aluminum of the former.

Studies of the effects of chlorine (HCl) on the oxidation/sulfidation resistance of Fe_3Al-based alloys were conducted using test facilities at the National Physical Laboratory (NPL) in the United Kingdom. Alloys were exposed to a test gas composed of CO_2, H_2, H_2O, and H_2S plus 1000-5000 ppm HCl at 450 and 550°C for 1000 h. Weight gains were relatively low and were generally less than companion specimens of Fe-Cr-Al alloys.

INTRODUCTION

The corrosion behavior of iron-aluminum alloys is being studied in high temperature mixed-oxidant atmospheres typical of coal combustion and gasification environments. The alloys are of two general types: Fe_3Al-based alloys containing 28 atom % Al with variable additions of Cr, Nb, Mo, and Zr, and iron-aluminum alloys containing 16% Al, 5% Cr, 1% Mo, 0.1% Zr, and 0.5%Y (compositions in atom %). The corrosion studies are intended to establish the operating performance limits of these alloys as a function of temperature and oxidant species (oxygen-sulfur-chlorine).

The effects of alloy composition on the oxidation and scaling resistance in air are being evaluated in laboratory tests under isothermal and cyclic temperature conditions. As reported earlier[1,2], the oxidation resistance of the 16% Al alloy was shown to approach that of the 28% Al alloys under isothermal conditions between 900 and 1000°C and under cyclic conditions at 1000 and 1150°C. The extent of oxide scale spallation in cyclic oxidation tests at 1000 and 1150°C was significantly reduced by the incorporation of 0.1% Zr in the alloys. Protection derived from the formation of a coherent and adherent α-Al_2O_3 scale.

More recent studies have been undertaken to assess the effect of both the aluminum and the zirconium contents upon the oxidation behavior of Fe_3Al alloys in air at 1300°C, and to compare their oxidation properties with other alumina-forming alloys. Recent work[3,4] on long term cyclic oxidation behavior of some of the best commercial alloys currently available (the alumina forming oxide dispersion strengthened [ODS] Fe+16-20% Cr+10% Al+0.1% Y_2O_3 ferritic alloys-MA956, ODM 751 and PM 2000), has demonstrated that for typical plant component thicknesses, life-time service conditions will be determined not by component section loss but by the time to onset of breakaway oxidation. This resulted from the aluminum content of the alloy falling (due to consumption by oxidation) below a critical value needed to sustain the protective alumina scale. At this juncture breakaway attack ensued, with the rapid formation of non-protective iron-rich oxides. The other principal parameter controlling the time to breakaway was the aluminum reservoir available within the alloy, which was determined by the alloy aluminum content and the component thickness. The aluminum concentration in these FeCrAl + Y_2O_3 ODS alloys is nominally 10%, whereas that of the Fe_3Al alloys can be up to 28%, thereby affording a much greater reservoir of aluminum.

The sulfidation resistance of iron aluminide alloys also makes them promising candidates as heat exchanger materials for coal gasifiers. Such an application requires the alloy to resist product gases containing small concentrations of H_2S and HCl at relatively low oxygen partial pressures ($<10^{-14}$ Pa) at temperatures up to 500°C. Laboratory tests of the 28% Al alloys in a H_2S-H_2-H_2O mixed gas with reference gasifier sulfur and oxygen activities showed the alloy to have considerably better resistance to H_2S than currently-used heat exchanger alloys. More recent tests have examined the corrosion of the iron aluminides in similar mixed gases containing small concentrations of HCl.

DISCUSSION OF CURRENT ACTIVITIES

High Temperature Oxidation Studies

Experimental

Four iron aluminum alloys, designated FAP, FA129, FA180 and FAL, were included in the test program. Compositions of the alloys are given in Table 1. Specimens, typically 1 x 1 cm or 2 x 1 cm, were cut from sheet having thicknesses between 0.23-0.70 mm. The specimens were contained in alumina crucibles and oxidized in either air or oxygen for successive periods ranging from 6-200 h, but usually 80 h, with intervening furnace cooling to room temperature. The oxidation temperature was 1300°C, but in addition FAP was oxidized at 1250°C. The extent of attack and of oxide spallation were measured gravimetrically. The specimens were also photographed to provide information on dimensional changes. Following the completion of the exposures, the chemical and physical nature of the attack was characterized by a range of surface analytical procedures, including X-ray diffraction (XRD), optical microscopy, scanning electron and transmission electron microscopy, energy dispersive X-ray analysis (EDAX) and electron microprobe analysis (EPMA).

Table 1. Alloy Composition

Alloy	Composition (atom %)					
	Fe	Al	Cr	Zr	Nb/Mo	Non-metals
FAP	72.9	16.1	5.0	0.1	1.1 Mo	0.1 C
FA129	65.7	28.0	5.0		1.0 Nb	0.2 C
FAL	66.9	28.0	5.0	0.1		
FA180	65.6	28.0	5.0	0.025	0.5 Nb 0.8 Mo	0.05 C 0.05 B
FAS	70.0	28.0	5.0			0.05 B

Results and Discussion

All the alloys tested contained 5% Cr but differed with respect to aluminum and zirconium contents. FA129, FA180 and FAL all contained 28% aluminum but had different zirconium levels. FA129 contained no zirconium, and FA180 and FA129 contained 0.025% and

0.1%, respectively. FAP contained a lower aluminum content (16%) and the higher zirconium level (0.1%). Therefore, comparison of FAP and FAL provides insight into the role of aluminum content, and the other alloys allow an assessment of the role of zirconium content.

The oxidation behavior of these alloys was characterized by four main features, namely, a protective oxidation regime, oxide spallation, oxidation-induced dimensional growth and breakaway attack. The increases in weight gain (i.e. the overall extent of attack) with time for the individual FA129, FA180, and FAL specimens are shown in Figure 1. Initially the FAL oxidation kinetics were essentially parabolic, indicative of a protective oxidation regime, which X-ray diffraction and microscopic examination showed to have resulted from the formation of an α-Al_2O_3 scale. At a critical weight gain, which increased with specimen thickness, the oxidation rate abruptly increased rapidly, resulting from the transformation from protective type oxidation to breakaway attack. Although the exact time to onset of breakaway could not be pinpointed exactly, it lay in the time interval between the last measurement in the protective regime and the first measurement following breakaway, which is the range of times quoted subsequently.

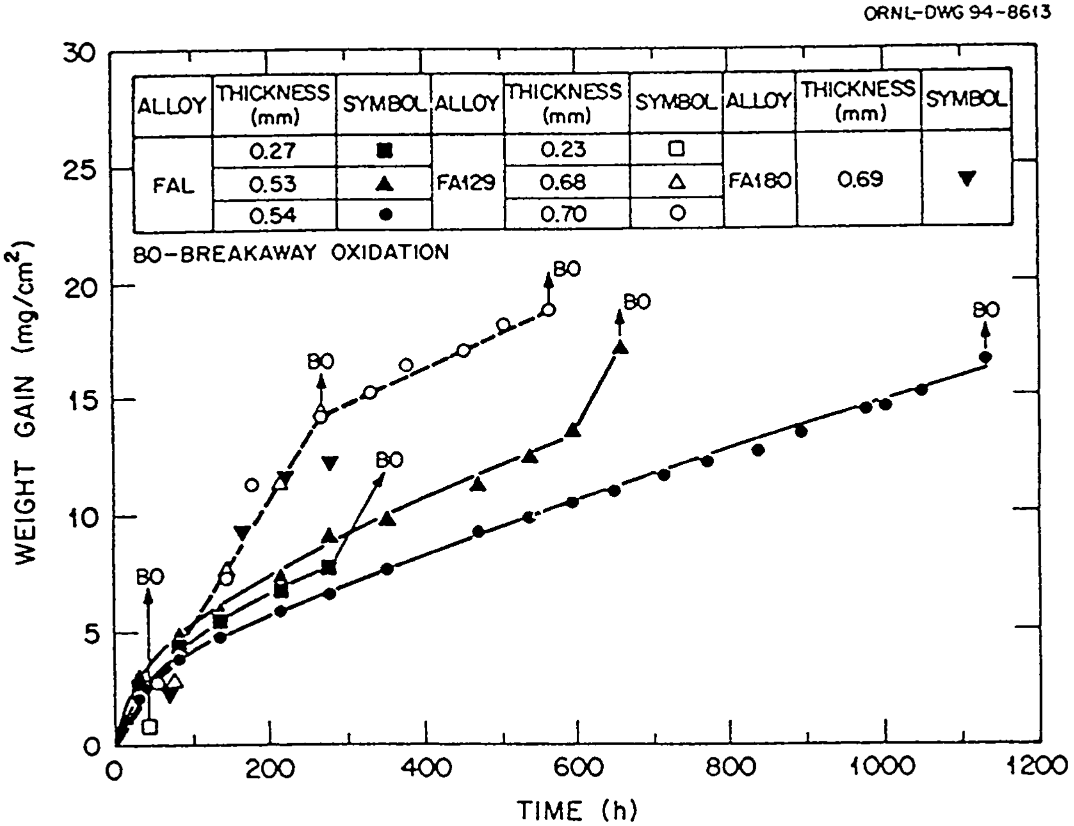

Figure 1. Comparison between the oxidation kinetics of FA129, FA180 and FAL in air at 1300°C.

Up to ~50 h the extent of oxidation of FA129, and also FA180, was comparable to that of FAL. At longer times the oxidation kinetics of FA129 and FA180 increased over that of FAL and became effectively linear (Figure 1). For comparable specimen thicknesses, the times to breakaway for FAL at 1300°C significantly exceeded those for FA129. On exposure at 1300°C the FAP alloy, with 16% aluminum, went immediately into breakaway oxidation; however, at 1250°C breakaway followed an initial period of parabolic oxidation behavior.

Although oxide spalled from all the alloys on cooling to room temperature, there was a major difference between the behavior of FA129 and FA180 and of FAL. With FA129 and FA180 most of the oxide formed spalled, such that the weight of spalled oxide increased linearly with exposure time. In contrast, with FAL most of the scale remained completely adherent throughout oxidation, and only a small fraction of the outermost layer of the scale spalled, primarily following the first thermal cycle. Although scale delamination was optically visible, the extent of spallation was often less than the gravimetric measurement limits. After 500 h of oxidation, the weight of spalled oxide from FA129 was 26 mg/cm^2 compared to only 0.5 mg/cm^2 from FAL.

Oxidation caused an increase in both the length and width of the FAL specimens. The kinetics of area extension followed that of oxidation, in that they were faster initially and continued at a rate which decreased progressively with time. For the 0.5 mm thick specimens the area had grown by ~35% prior to breakaway. FA129 specimens also grew in area as a result of oxidation with similar kinetics but by a smaller extent, with a ~16% extension prior to breakaway.

These results clearly indicate that both the zirconium and aluminum contents have a significant effect on the high temperature oxidation behavior of iron-aluminum alloys. Mechanistic understanding of the role of zirconium was revealed by detailed characterization of the oxide scale formed on FA129 and FAL and how this related to current understanding of the development and failure of protective alumina scales.[5,6,7] The alumina scale on FA129 was similar to that formed on FeCrAl alloys[5] in that it was convoluted and generally detached from the alloy with only localized areas of attachment. In contrast, the corresponding scales on FAL were both compact and adherent. The FAL scales were shown by EPMA to be enriched in zirconium, whose concentration was highest near the gas interface and decreased with scale depth. Various surface analytical techniques (SEM, TEM with EDAX, and XRD) established that zirconium was present as discrete 0.5-1.2 mm diameter ZrO_2 (monoclinic) particles. On the basis of studies on related systems[6], it would also be expected that zirconium would be segregated at the oxide grain boundaries, although this has yet to be established for FAL.

Based on reference 9, the alumina scale on FA129 can be assumed to have developed by the transport both of cations outward and oxidant inward. At 1300°C convoluted scale formation is indicative of rapid aluminum surface diffusion. This scale cracked and spalled readily on cooling. However, on re-exposure of the alloy, scale regeneration was facilitated by the relatively high aluminum level in the alloy (until it fell below the critical level for onset of breakaway). The linear oxidation kinetics were consistent with successive scale thickening and breakdown, with oxidation being controlled by transport through a thin, surface oxide barrier layer.

Zirconium is one of the so called reactive elements known to improve the protection afforded by alumina scales, and indeed it acted in this role on FAL. As a result of ZrO_2 particle formation and the resultant oxide grain boundary segregation of zirconium by Ostwald ripening, outward cation transport was inhibited, such that the scale on FAL would have developed primarily by inward anion transport.[6,7] Zirconium also dramatically improved scale adherence, probably largely due to the change in oxide growth mechanism. A further contributing factor was that the stresses resulting from oxidation were relieved by deformation of the underlying alloy, which like all ferritic alloys had a low creep strength at 1300°C. As a consequence the resultant strain on the alumina scale on cooling was considerably lower than would have been experienced by a comparable scale on the significantly stronger ODS alloys, which in certain circumstances is known to cause scale spallation.[3,4] It should be added that the lower deformation of FA129 compared with FAL was entirely consistent with the poorer adhesion and thinner scales on the FA129 alloy. Finally, it should be noted that whereas a zirconium concentration of 0.1% proved to be effective in improving oxidation resistance, a factor of four lower level (0.025%) was not.

In this series of iron-aluminum alloys, in which the chromium content was limited to 5%, the concentration of 16% aluminum in FAP was insufficient for protective alumina scale formation at 1300°C, even though the alloy also contained 0.1% zirconium. However, a protective type oxidation regime was established on the alloy at lower temperatures. At 1300°C the higher aluminum content (28%) afforded by the Fe_3Al alloy proved to be essential. In the case of the FeCrAl alloys, the presence of 10% aluminum in combination with 18-20% chromium provides better oxidation resistance at 1300°C than observed for the FAL alloy and demonstrates a synergistic interaction between chromium and aluminum that promotes the formation of protective alumina scales at lower aluminum levels.

The overall mechanism leading to breakaway oxidation of these alloys appears to be similar to that already modelled for the alumina forming FeCrAl-Y_2O_3 ODS alloys.[3,4] Non-protective oxidation occurred when the alloy aluminum content was reduced, by scale formation, to a value below that needed to sustain continuing growth of a protective alumina scale. Breakaway was dependent, therefore, on four critical parameters. These included the extent of aluminum available (i.e. the alloy aluminum content and specimen thickness), the rate of aluminum consumption through oxidation (including effects of spallation), and the rate of aluminum diffusion from within the alloy to the oxidizing surface. As observed with the ODS alloys[4], the rate of aluminum diffusion was relatively rapid; i.e., there was no perceptible aluminum concentration gradient across oxidized FAL specimens based on EPMA analyses. The fourth parameter was the value of the residual alloy aluminum content leading to breakaway attack. This could be determined from the last weight gains prior to breakaway and also from EPMA measurements on metallographically mounted specimens taken from alloy regions beneath protective oxide scales that adjoined regions which had oxidized completely following breakaway. For FAL the values calculated from weight changes ranged between 3.1-5.8 weight %, while the EPMA values were between 1.8 and 2.4 weight %. These were slightly higher than the corresponding calculated residual aluminum contents for FeCrAl+Y_2O_3 (reference 4) for which the average of fifteen values, ranging between 0.3 and 3.5 weight %, was 1.8%. For FA129 the calculated and EPMA residual aluminum values, respectively, were higher than the FAL values.

The measured times to breakaway for the three Fe_3Al alloys have been superimposed in Figure 2 upon the corresponding plot of weight change vs specimen thickness derived for the ODS FeCrAl+Y_2O_3 alloys[3,4] in air and oxygen. The data are generally consistent for all alloys-the time to breakaway increased with specimen thickness, FAP exhibited the worst behavior, while FA129 was inferior to FAL. That the FAL values fell on or slightly above the best estimate line through the ODS results is entirely coincidental, but it does demonstrate that the behavior of this alloy is at least as good as the best commercially available ODS ferritic alloys. It also suggests that the potential offered by the increased aluminum content of FAL compared to the FeCrAl alloys is not being fully exploited. Two factors limiting the performance of FAL compared with the ODS alloys were, first, the slightly higher residual aluminum level where breakaway occurred, and, second and more significantly, the higher oxidation rate of FAL. As an indication, at 1300°C the FAL parabolic rate constant (40×10^{-2} $mg^2 \cdot cm^{-4} \cdot h^{-1}$) was over an order of magnitude greater than that for the ODS alloy ODM 751 (2.5×10^{-2} $mg^2 \cdot cm^{-4} \cdot h^{-1}$). If the Fe_3Al oxidation rate could be reduced to the lower value, then the time to breakaway would be significantly increased; e.g., for a 0.5 mm thick component this time would be in excess of 9000 h rather than 600 h as at present.

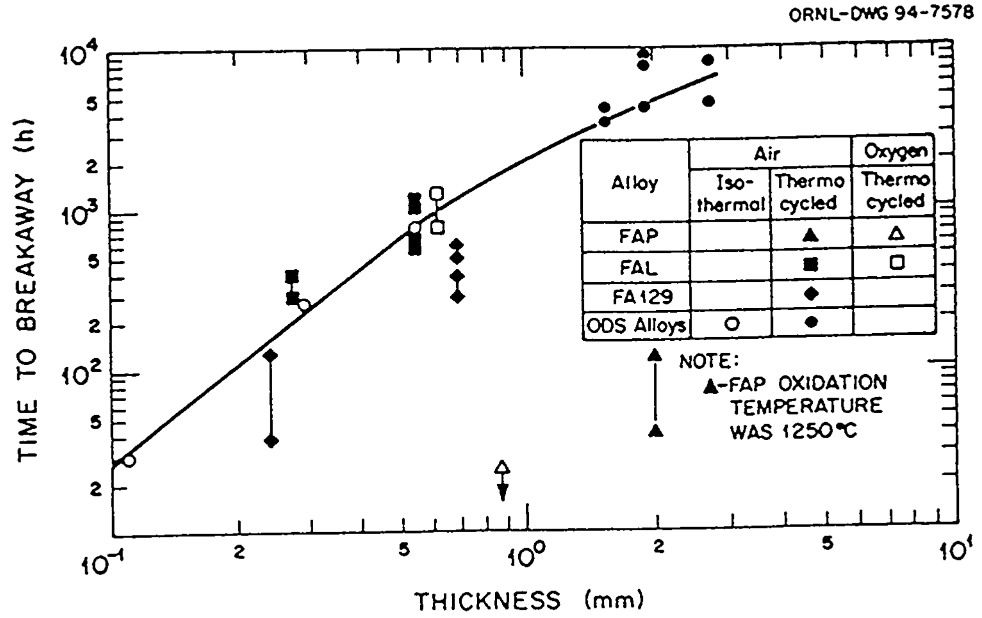

Figure 2. Influence of alloy thickness on the time to breakaway oxidation of FAL, FA129, and FAL and of ODS FeCrAl+Y_2O_3 alloys in air and oxygen at 1300°C.

Reducing the oxidation rate of Fe_3Al alloys to at least that of commercial ODS alloys appears to be a feasible objective. It should be achievable by optimizing not only the concentration, but also the nature of the reactive element. There are strong arguments for incorporating the reactive element as an oxide dispersoid and also for gaining synergistic effects from multiple reactive element additions. Both aspects are being researched as part of our overall iron aluminide development program.

Effect of HCl on Sulfidation of Fe_3Al by H_2S-Containing Mixed Gases

Experimental

Test specimens of the iron-aluminum alloys FAS, FA129, and FAP were supplied to National Physical Laboratory (NPL) for exposure to a CO-H_2-H_2O-CO_2 mixed gas containing small concentrations of both H_2S and HCl. Nominal compositions of the alloys are given in Table

Table 1. The specimen size was 10 mm x 10 mm x 3 mm. The major faces of the specimens were precision machined so that the 3 mm cross section was flat and parallel to within 2.5 μm. This was required to accommodate the automated measuring technique that NPL uses to monitor thickness changes due to corrosion, which has a precision of ± 3μm. The test gas was composed of 24.8% CO, 20.4% H_2, 3.93% CO_2, 6.3% H_2O, 0.123% H_2S, bal. N_2 (by volume). HCl was added to a concentration of 1000 ppm by passing the gas mixture over a dilute solution of hydrogen chloride heated to achieve the appropriate HCl and H_2S vapor pressures. Duplicate specimens of each material were exposed to the flowing test gas at 450°C, and single specimens, at 550°C. Analyses of the gas leaving the specimen retorts indicated that the oxygen-containing species had not equilibrated at the test temperatures, so the $p(O_2)$ was assumed to be fixed by the H_2/H_2O ratio.[8] The sulfur and oxygen activities of the gas at the respective test temperatures are recorded in Table 2. Exposures were conducted for a total duration of 1000 h with six weighings during the first 320 h and five weighings thereafter. A FeCrAl alloy containing 20% Cr, 8% Al, 0.1% Y, bal. Fe (provided by NPL) was exposed concomitantly with the iron-aluminum specimens and served as a reference against which to evaluate the relative corrosion resistance of the various alloys.

Table 2. Fugacities of S_2 and O_2 in the NPL Test Atmosphere

Temperature °C	O_2 Fugacity*	S_2 Fugacity
450	9.7×10^{-27}	5.1×10^{-8}
550	2.0×10^{-22}	1.9×10^{-6}

* Based on $p(H_2):p(H_2O)$ ratio

Results and Discussion

Figure 3 compares the weight changes for the Fe_3Al alloys (28% Al) at 450°C with those for the FeCrAl alloy. The weights increased for the first 600 h and then became constant or decreased slightly. Except for one of the FAS specimens, all the iron aluminides showed lower weight gains than the FeCrAl alloy. The FAP alloy (16% Al) at 450°C showed relatively high initial weight losses (>8 mg/cm^2) followed by still larger weight gains (≤75 mg/cm^2) after 600 h. As shown in Figure 4, at 550°C weight gains of the Fe_3Al alloys increased uniformly with test time, although the gains were initially less than those for corresponding times at 450°C. After

1000 h the gains at 550° C were approximately the same as at 450° C and were approximately half the weight gains of FeCrAl at 550° C. The FAP alloy at 550° C showed a relatively high weight gain after only 20 h, but after 1000 h the weight gain was somewhat less than at 450° C.

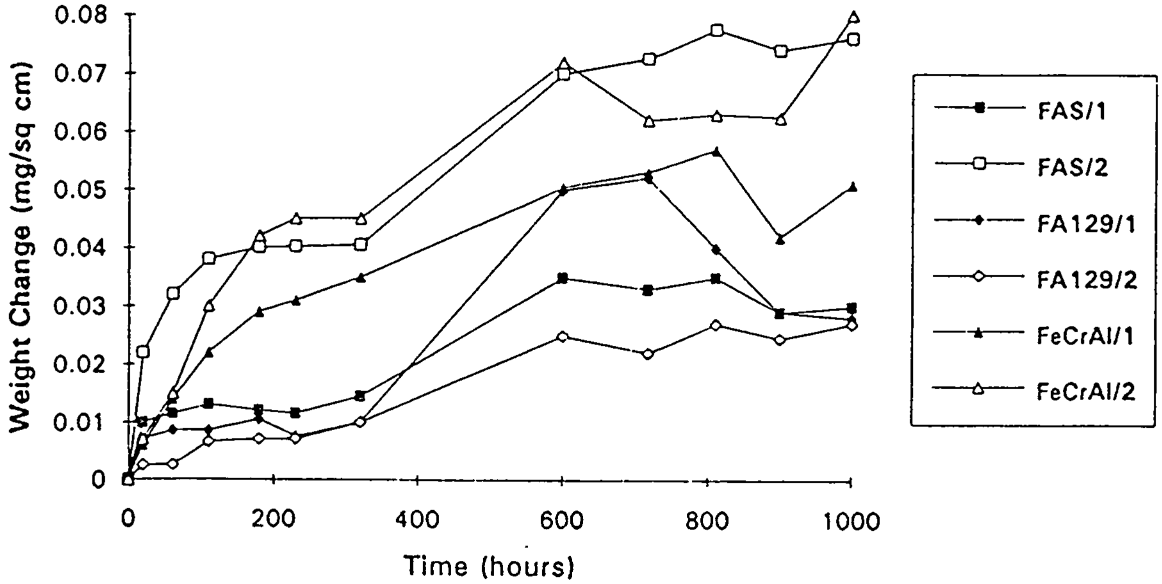

Figure 3. Comparative weight changes of Fe_3Al-based alloys and FeCrAl at 450° C in simulated coal gas atmosphere containing 1000 ppm HCl.

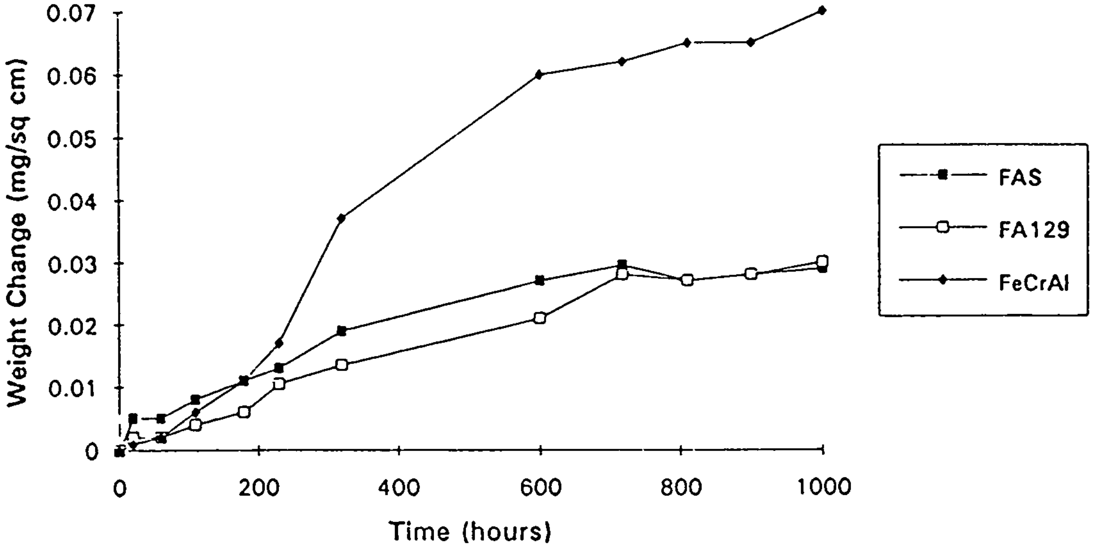

Figure 4. Comparative weight changes of Fe_3Al-based alloys and FeCrAl at 550° C in simulated coal gas atmosphere containing 1000 ppm HCl.

The relatively low weight changes observed for the Fe_3Al alloys in these tests are in accord with results from laboratory tests conducted at higher temperatures (700-800° C) in H_2S-containing gas mixtures without HCl.[9] However, the FAP alloy was much less resistant to attack in the NPL test environment than in the higher temperature laboratory tests in mixed gas with H_2S and no HCl. Furthermore, in the latter laboratory tests, the sulfidation resistance of the FAP alloy, though less than that of the Fe_3Al alloys, was significantly better that of the FeCrAl alloy.[10] The higher chromium content of the FeCrAl alloys and the lower aluminum content both contributed to the poorer performance of this material under purely sulfidizing conditions at ≥700° C. In the case of the NPL tests, where the exposure temperatures are lower and HCl is present, chromium at the 20% level no longer had a detrimental effect on corrosion resistance, particularly compared to the FAP alloy containing 16% aluminum and 5% chromium. Furthermore, the addition of 5% chromium to the Fe_3Al base composition (FA129), which markedly reduces the sulfidation resistance against H_2S at higher temperatures,[10] either did not change or slightly improved the corrosion resistance in the NPL tests. To what extent this result is due to the lower temperature or to the influence of HCl is not clear from the present test results. However, the absence of any significant effect of the HCl on the corrosion resistance of the Fe_3Al-based alloys suggests that the lower temperature may be the more important factor.

REFERENCES

1. J. H. DeVan and P. F. Tortorelli "Environmental Effects on Iron Aluminides", *Proceedings of the Seventh Annual Conference Fossil Energy Materials*, ORNL/FMP-93/1, 277-288, Oak Ridge National Laboratory, Oak Ridge, TN (1993).

2. P. F. Tortorelli, J. H. DeVan and E. K. Abdali, "Cyclic Oxidation of Iron Aluminides:, *CORROSION 93*, paper 258/9, National Association of Corrosion Engineers, Houston (1993).

3. W. J. Quadakkers and M. J. Bennett, "Oxidation Induced Lifetime Limits of Thin Walled, Iron Based, Alumina Forming Oxide Dispersion Strengthened Alloy Components", to be published in *Materials Science and Technology*, 1994.

4. M. J. Bennett, R. Perkins, J. B. Price and J. A. Desport, "The Oxidation Behavior of Alumina Forming Ferritic Oxide Dispersion Strengthened alloys", to be published in the *Proceedings of the First Mexican Symposium on Metallic Corrosion*, held at Merida, Yucatan, Mexico, March 7-12, 1994.

5. F. A. Golghtly, F. H. Stott and G. C. Wood, "The Influence of Yttrium Additions on the Oxide Scale Adhesion on a Fe-Cr-Al Alloy", *Oxid. Met.*, 10, 163-187 (1976).

6. B. A.Pint, J. R. Martin, and L. W. Hobbs, "^{18}O/SIMS Characterization of the Growth Mechanism of Doped and Undoped α-Al_2O_3", *Oxid. Met.* 39, 167-195 (1993).

7. R. Prescott and M. J. Graham, "The Formation of Aluminum Oxide Scales on High Temperature Alloys", *Oxid. Met.*, 38, 233-255 (1992).

8. W. T. Bakker, "Effect of Gasifier Environment on Materials Performance", *Materials at High Temperatures*, 11 (1-4), 81-93 (1993).

9. J. H. DeVan and P. F. Tortorelli, "Oxidation/Sulfidation of Iron-Aluminum Alloys", *Materials at High Temperatures*, 11 (1-4), 30-35 (1993).

10. J. H. DeVan and P. F. Tortorelli, "The Oxidation Behavior of Iron Alloys Containing 16-40 at % Aluminum", *Corrosion Science*, 35 (5-8) 1065-1071 (1993).